Imperial College London
Department of Physics

The Gulf Stream as a Modulator for Atmospheric Blocking

Jamie Mathews

Supervisor: Dr. Arnaud Czaja

Submitted in part fulfilment of the requirements for the degree of
Doctor of Philosophy from Imperial College London, October 2024

Abstract

This work examines the influence of the Gulf Stream on wave breaks in the mid-latitude jet stream, known as atmospheric blocking. Chapter 3 explores the connection between North Atlantic blocking and the Gulf Stream's diabatic effects using ERA5 reanalysis (1979-2020). Turbulent heat fluxes over the Gulf Stream generate negative potential vorticity (PV) in the atmospheric boundary layer, which ascends via the warm conveyor belt to strengthen the block's upper-level PV anomaly. Blocking size and frequency are linked to oceanic preconditioning, with anomalous heat transport and content enhancing turbulent heat fluxes before blocking events.

In Chapter 4, the ECMWF IFS model tests this theory by suppressing surface latent heat flux over the Gulf Stream. This reduces Northern Hemisphere blocking frequency by up to 30%, with shorter lifespans (-6%), smaller spatial extents (-10%), and reduced intensities (-0.4%), though the number of individual blocking anticyclones increases (+17%). Responses are consistent across model resolutions, with Tco639 ($\sim$18 km) showing the largest changes. Diminished moisture fluxes favour eastward Rossby wave propagation and higher zonal wavenumbers, while air-sea interactions promote stationary, westward-propagating waves with zonal wavenumber 3.

Chapter 5 abstracts these interactions by deriving a simple heuristic three-box blocking model which consists of an oceanic mixed layer coupled to the atmospheric boundary layer through air-sea heat fluxes, which is further coupled to the upper troposphere via convection. The model reproduces key features of blocking, including positive ocean heat anomalies before a block and negative anomalies afterward. Upper-level PV anomalies correlate with boundary-layer PV and ocean temperature prior to the event, suggesting upward causal propagation. Parameter modifications reveal a Hopf bifurcation and chaotic regime, leading to a generally increasing Lyapunov exponent, indicating reduced predictability.

These findings highlight the importance of coupled ocean-atmosphere interactions, as neglecting them risks overlooking critical system dynamics and emergent properties.

Acknowledgements

I would like to express my deepest gratitude to my supervisor, Dr. Arnaud Czaja. Not only has he been an inspirational scientific mentor, but his honesty and openness throughout my time at Imperial College have been a great source of moral guidance. I would also like to thank Frederic Vitart and Christopher Roberts at ECMWF for their support in running an experiment on the IFS—a challenging but ultimately rewarding endeavour. Thanks to Dr. Gwendal Riviere and Vinita Deshmukh for the engaging discussions and generous hospitality during my secondment at LMD. I extend my gratitude to everyone in EDIPI, some of the finest people I have ever had the good fortune to be associated with. Finally, the biggest of thank yous to my family, friends and Ann, who have always shown me love when I needed it the most.

Declaration

I hereby declare that except where specific reference is made to the work of others, the contents of this dissertation are original and have not been submitted in whole or in part for consideration for any other degree or qualification in this, or any other university. This dissertation is my own work and contains nothing which is the outcome of work done in collaboration with others, except as specified in the text and Acknowledgements. Chapter 3 has been published in Climate Dynamics (Mathews & Czaja 2024) and Chapter 4 has been published in Geophysical Research Letters (Mathews et al. 2024).

Copyright

The copyright of this thesis rests with the author. Unless otherwise indicated, its contents are licensed under a https://creativecommons.org/licenses/by/4.0/Creative Commons Attribution-NonCommercial 4.0 International Licence (CC BY-NC).

Under this licence, you may copy and redistribute the material in any medium or format. You may also create and distribute modified versions of the work. This is on the condition that: you credit the author and do not use it, or any derivative works, for a commercial purpose.

When reusing or sharing this work, ensure you make the licence terms clear to others by naming the licence and linking to the licence text. Where a work has been adapted, you should indicate that the work has been changed and describe those changes.

Please seek permission from the copyright holder for uses of this work that are not included in this licence or permitted under UK Copyright Law.

'Je m'occupe, moi, des choses sérieuses!'

The Little Prince - Antoine de Saint-Exupéry

Contents

Abstracti

Acknowledgements **iii**

1 Introduction **1**

1.1 Motivation 1

1.2 Thesis Outline 4

2 Background Theory **5**

2.1 The Jet Stream 5

2.1.1 The General Circulation of the Troposphere 5

2.1.2 Rossby Waves 7

2.2 Atmospheric Blocking 10

2.2.1 The Importance of Atmospheric Blocking 10

2.2.2 Dry Processes 12

2.2.3 Moist Processes 13

2.3 Ocean-Atmosphere Coupling 14

2.3.1 Air-Sea Heat Fluxes 14

2.3.2 Oceanic Mixed Layer Dynamics 15

2.3.3 Ocean Current Dynamics 16

2.3.4 Ocean-Atmosphere Coupling in the North Atlantic 17

2.4 Potential Vorticity 20

2.4.1 Symmetric Instability 21

2.4.2 Diabatic Effects on Potential Vorticity 23

2.5 Dynamical Systems Theory 24

2.5.1 Chaos Theory 27

3 Observational Evidence for Oceanic Maintenance of Atmospheric Blocking 32

3.1 Introduction . . . 32
3.2 Method . . . 35
3.3 Results . . . 37
3.3.1 Synoptic and Climatological Conditions . . . 37
3.3.2 Oceanic Preconditioning . . . 43
3.3.3 Mechanism . . . 46
3.4 Discussion . . . 49
3.4.1 Method . . . 49
3.4.2 Orders of Magnitude . . . 49
3.4.3 Prediction . . . 51
3.5 Conclusion . . . 51
4 Testing the Gulf Stream's Influence on Atmospheric Blocking 54
4.1 Introduction . . . 54
4.2 Data and Methodology . . . 55
4.2.1 Model Set Up . . . 55
4.2.2 Diagnostic Methods . . . 57
4.3 Results . . . 59
4.3.1 The Effect on Atmospheric Blocking . . . 59
4.3.2 Changes in the Jet Stream and Rossby Wave Characteristics . . . 63
4.3.3 The Interrupted Oceanic Pathway . . . 66
4.3.4 Dependence on Model Resolution . . . 70
4.4 Conclusions . . . 74
5 A Heuristic Model for the Oceanic Pathway to Atmospheric Blocking 76
5.1 Introduction and Motivation . . . 76
5.2 The Model . . . 79
5.3 Method . . . 82
5.4 Results . . . 83
5.4.1 Fixed Ocean Model . . . 83
5.4.2 Coupled Model . . . 85
5.5 Discussion . . . 93
5.5.1 The Fixed Ocean Model . . . 93
5.5.2 The Fully Coupled Ocean . . . 94

5.5.3 Implications for Observations and Modelling 98
5.6 Conclusion 100
6 Conclusion **101**
6.1 Summary of Thesis Achievements 101
6.2 Applications 103
6.3 Future Work 105
A Diabatic PV Generation **107**
B Non-Dimensionlizing the Box Model **111**
Bibliography **112**

List of Tables

3.1 The collection of time series used in this analysis, with a description of which data set they belong to, their units, frequency, location and how they were calculated. 36

4.1 Initial dates used for the reforecasts and the date the first block was detected over the North Atlantic in ERA5 data. Winter reforecasts are depicted in **bold**. 56

4.2 Percentage change in blocking frequency over the NH relative to the control run for the entire reforecast period is presented. The first two weeks of the forecast are shown in brackets. Winter reforecasts correspond to NDJFMA, while Summer corresponds to MJJASO, as indicated in Table 4.1. Results significant over the 99% confidence interval are depicted in **bold**. 60

List of Figures

1.1 Observational data of the North Atlantic sea surface temperatures shown in coloured shading on the 7^{th} of May 2024 taken from `https://earth.nullschool.net`. The winds at 250hPa are shown with the grey streamlines and the ocean surface currents are shown with the white streamlines. 1

1.2 Fig. 2 from Kautz et al. (2022) showing a wave breaking in the jet stream illustrated by the thin black contour representing an upper-level geopotential height contour. Hot and cold extremes exist inside the red and blue dashed contours, respectively. Regions of high integrated water vapor transport, heavy precipitation, and warm conveyor belt ascent are shown in orange, blue, and purple shading, respectively. Snow and thunderstorms are shown in blue stars and lightning bolts, respectively. 2

1.3 Fig. 17 from O'Reilly et al. (2016) showing a schematic of the effect of Gulf Stream frontal sharpness on the development of a ridge in the atmospheric jet stream. The jet stream is shown in black and grey arrowed contours, while the sea surface temperature (SST) contours are shown in red, with the real and smoothed SST gradient results shown on the left and right, respectively. Precipitation and eddy kinetic energy are shown in green and red shading, while meridional heat transport is represented by a yellow arrow. 3

2.1 The December, January, February (DJF) climatology of the meridional transport (top) and zonal wind (bottom) from ERA-40 Atlas (Sterl & Caires 2005). . . . 6

2.2 Schematic of Rossby wave propagation. Low and high-pressure systems are illustrated in red and blue, respectively, while neutral air is depicted in green. The grey line shows the flow of air along the jet stream. A section of the Earth's atmosphere is shown in a light blue fill, with the vorticity of the neutral air shown with the green vectors inside it. 8

2.3 Fig. 3 from Hoskins & Karoly (1981) showing the geopotential height anomalies as a result of heating in the mid-troposphere. The hashed mask indicates the region being heated, while solid and dashed contours show positive and negative geopotential height anomalies, respectively. 9

2.4 Fig. 2 from Croci-Maspoli et al. (2007) showing the seasonal atmospheric blocking climatology using the PV anomaly index from Schwierz et al. (2004). The colour shading depicts the frequency of atmospheric blocking. 11

2.5 Fig. 1 from Cobb & Czaja (2019) illustrating the difference in sea surface temperatures (SSTs) between the positive and negative phases of the NAO, based on the NAO index defined by Hurrell et al. (2003). 18

2.6 Fig. 4B from Häkkinen et al. (2011) showing the anomalous blocking frequency for a high Atlantic Multi-decadal Oscillation (AMO). 19

2.7 Vortex stretching between two isentropic surfaces, taken from Hoskins (1997), Fig. 4. 20

2.8 The average PV between 900-975 hPa (top) and a PV meridional section (bottom) (in PVU, 1 PVU = 10^{-6} Km^2 s^{-1} kg^{-1}) for a blocking event starting on January 18th, 2020. The white dashed line in the top panels indicates the position of the section used in the bottom panels. The red stippled contour shows upward velocities at 500 hPa where $\omega < -1$ Pa s^{-1}, while the hollow stippling shows air that has a relative humidity above 90% at 975 hPa. The brown, light blue, and red lines in the bottom panels show surfaces of constant momentum, moist potential temperature, and the height of the atmospheric boundary layer, respectively. 22

2.9 Fig. 9 from Stoelinga (1996), showing the effect of latent heating along a WCB. Absolute momentum surfaces and streamlines are shown with thin arrowed lines. Absolute vorticity vectors are shown with white arrows. Shading depicts the strength of latent heating and vertical transport. '+' and '-' symbols show the generation and destruction of PV, respectively. 23

2.10 Fig. 1.3.1 from Strogatz (2018) describes the types of behaviours possible for dynamical systems of different dimensions and increasing non-linearity. 25

2.11 Saddle node bifurcation for the equation $\dot{x} = r + x^2$ where r is the control parameter, taken from Strogatz (2018), Fig. 3.1.1. Filled and hollow dots denote stable and unstable fixed points, respectively, while half-filled dots denote half-stable fixed points. 26

2.12 The Lorenz (1963) attractor for parameters $\sigma = 10$, $\rho = 28$, and $\beta = 8/3$. The colour shading shows the local dimension of the attractor calculated following Faranda et al. (2017). 28

2.13 Bifurcation diagram for the Rossler (1976) system for variable x, with bifurcation parameter c. Parameters $a = b = 0.1$. The largest Lyapunov exponent is shown in red. 29

3.1 PV section (left) and PV averaged between 900-975 hPa (in PVU, 1 PVU = 10^{-6} Km^2 s^{-1} kg^{-1}) (right) for a blocking event starting on January 18th, 2020. In the left panels, the light red, light blue, and dashed red contours indicate the potential temperature, equivalent potential temperature, and boundary layer height respectively. In the right panels, the white contour indicates the blocking mask, the orange contours show the 500 Wm^{-2}, 1000 Wm^{-2}, and 1500 Wm^{-2} turbulent heat flux, and the red stippled contour shows upward velocities at 500 hPa where $\omega < -1$ Pa s^{-1}. The dashed white line indicates where the section is taken. 38

3.2 As in Fig. 3.1 but now showing moist PV. 39

3.3 DJF climatology of the THF and PV at 950hPa over the North Atlantic. The green and orange contours represent the 7.5% blocking frequency and the 350Wm^{-2} THF climatology during DJF, respectively. 41

3.4 DJF climatology of the negative PV frequency. The white contours indicate the frequency of negative moist PV. The green and orange contours represent the 7.5% blocking frequency and the 350 Wm^{-2} THF climatology during DJF, respectively. 42

3.5 Surface pressure anomaly (in hPa, color) composite during periods when a block is present inside the green 7.5% DJF blocking frequency climatology contour minus blocking absence in this same contour . The white arrows indicate the 10m wind anomalies, with the black arrow showing the size of the 1m/s vector. The orange contour represents the 350 Wm^{-2} THF climatology during DJF. The stippling indicates 95% confidence. 43

3.6 The top panel shows the cross correlation between the seasonally averaged blocking area time series (refer to Table 3.1) in DJF and the Florida Straits heat transport (light blue), and the heat content (dark orange) time series. The 95% confidence interval is shown with a coloured fill. The bottom panel shows the composite of the blocking frequency in DJF, 5 months after increased heat transport through the Florida Current. The green and orange contours represent the 7.5% blocking frequency and the 350Wm^{-2} THF climatology during DJF, respectively. The light blue line shows the RAPID N26 mooring. Dotted stippling indicates 95% confidence. 44

3.7 A composite of the top 300m Argo heat content 4 months before (top panel) and 2 months after (bottom panel) increased blocking area inside the green contour representing the 7.5% blocking frequency climatology during DJF. The orange contours represent the 350Wm^{-2} THF climatology during DJF. The light blue line shows the RAPID N26 mooring. Dotted stippling indicates 95% confidence. 45

3.8 A schematic summarising the series of events that lead to oceanic maintenance of atmospheric blocking. The bottom slab represents the ocean, with blue and red colors representing anomalously cold and warm water respectively. The red, orange and green arrows show the warm water transport, heat flux from the ocean to the atmosphere and the WCB respectively. The purple blobs show anomalously low PV. Low pressure systems are illustrated with red and blue fronts and grey isobars. The markers A, B, and C are described in the main text. 47

4.1 Mean blocking frequency for ERA5 (top left), the control run (middle left), the NO_GS_SLHF run (bottom left), and the difference between the NO_GS_SLHF and control runs (right). The grey contours indicate the SLHF mask applied, with the darkest (lightest) contour indicating complete suppression (permission). Stippling indicates areas that exceed the 95% confidence interval. 57

4.2 As in Fig. 4.1 but now calculated using the **geopotential height reversal index**. 60

4.3 As in Fig. 4.1 but now calculated using the **geopotential height anomaly index**. 61

4.4 Mean blocking frequency for ERA5 (top left), the control run (middle left), the NO_GS_SLHF run (bottom left), and the difference between the NO_GS_SLHF and control runs (right) for the first two weeks of the reforecast. The grey contours indicate the SLHF mask applied, with the darkest (lightest) contour indicating complete suppression (permission). Stippling indicates areas that exceed the 95% confidence interval. 62

4.5 The difference in mean blocking frequency between the NO_GS_SLHF and control runs for the extended summer (left) and extended winter (right). The grey contours indicate the SLHF mask applied, with the darkest (lightest) contour indicating complete suppression (permission). Stippling indicates areas that exceed the 95% confidence interval. 63

4.6 The distributions of the block characteristics for the control (light red) and NO_GS_SLHF (light blue) runs. From left to right the block's duration, average size, and intensity (total PV per area) are shown. Solid lines represent the mean values, while dotted lines represent the upper and lower quartiles. 63

4.7 The zonal wind at 250hPa (a) and the power spectrum of the vertically averaged anomalous PV field from 500hPa to 150hPa within the latitudinal range of 40°N to 60°N (b) are presented. In both figures, the shading illustrates the difference between the NO_GS_SLHF and control runs, with the blue and red contours representing their respective reforecast means. The region between 40°N and 60°N is indicated by green dashed lines. The theoretical phase speed for different meridional wavenumbers at 40°N, applying a background flow of 16.4 m/s as observed, is depicted with grey dashed lines. Areas that exceed the 95% confidence interval are highlighted with stippling. 64

4.8 Meridional cross-section of the mean zonal wind for the entire Northern Hemisphere (top), the North Atlantic 60°W - 0°E (middle), and the North Pacific 120°E - 180°E (bottom). The control run is shown with the red contours, while the shading depicts the difference between the NO_GS_SLHF and the control runs. The dashed green box depicts the region where the spectral analysis is computed as in Fig. 4.7. 65

4.9 The power spectrum of the vertically averaged anomalous PV field from 500hPa to 150hPa within the latitudinal range of 40°N to 60°N for extended summer (left) and extended winter (right). The shading illustrates the difference between the NO_GS_SLHF and control runs, with the blue and red contours representing their respective reforecast means. The theoretical phase speed for different background flows at 40°N, applying a meridional wavenumber of 4, is depicted with grey dashed lines. Areas that exceed the 95% confidence interval are highlighted with stippling. 66

4.10 The difference between the NO_GS_SLHF and control runs for the SLHF (left), SST (middle) and SSHF (right). Stippling indicates areas that exceed the 95% confidence interval. 67

4.11 The difference between the NO_GS_SLHF and control runs for the PV at 850 hPa (left), minimum surface pressure throughout the forecast (middle), and PV anomaly between 150hPa and 500 hPa (right). Stippling indicates areas that exceed the 95% confidence interval. 68

4.12 The difference between the NO_GS_SLHF and control runs for the WCB inflow (top left), ascent (top middle), outflow (top right), anomalous PV inflow (bottom left), anomalous PV outflow (bottom middle), and total anomalous PV outflow (bottom right). Green contours indicate the control values with contour intervals being 1%, 4%, and 9% respectively. Stippling indicates areas that exceed the 95% confidence interval. 69

4.13 As in Fig. 4.1 but now at resolution **Tco319**. 71

4.14 As in Fig. 4.1 but now at resolution **Tco199**. 72

4.15 The percentage change in the block's characteristics for the NO_GS_SLHF run with respect to the control run verses resolution. The block's duration, average size, intensity, and the number of individual blocks detected per forecast are shown in green, orange, purple, and red, respectively. Fully saturated colours indicate changes over the 95% confidence level. 73

4.16 The difference between the WCB inflow (left), ascent (middle), and outflow (right) sensitivity of Tco639 and Tco199. Green contours show the difference between the NO_GS_SLHF and control runs for resolution Tco639 as shown in shading in Fig. 4.12, with dashed lines showing negative values. 73

5.1 The average PV between 900-975 hPa (top) and a PV zonal section (bottom) (in PVU, 1 PVU = 10^{-6} Km^2 s^{-1} kg^{-1}) for a blocking event starting on January 18^{th}, 2020. The white dashed line in the top panels indicates the position of the section used in the bottom panels. The red stippled contour shows upward velocities at 500 hPa where $\omega < -1$ Pa s^{-1}, while the hollow stippling shows air that has a relative humidity above 90% at 975 hPa. The brown, light blue, and red lines in the bottom panels show surfaces of constant momentum, equivalent potential temperature, and the height of the atmospheric boundary layer, respectively. . 77

5.2 As in Fig. 5.1 but for moist PV. 78

5.3 Schematic of the three-box blocking model. The bottom box represents the average ocean temperature θ in the oceanic mixed layer, the middle box is the average boundary layer moist PV Q_B, and the top box is the average upper troposphere PV Q_A. The height of each box is denoted by h. The ocean is connected to the atmospheric boundary layer via heat fluxes F, indicated by the orange arrow. The atmospheric boundary layer is then connected to the upper box via convection σ, represented by the green arrow. The upper-level PV anomaly decays according to λ_A, depicted by the orange hue. Air is allowed to flow through the boundary layer u, indicated by the blue arrow, with the inflow of new PV into the boundary layer box is denoted by Q_{In}, while the inflow of heat into the oceanic mixed layer is represented by ϕ. 80

5.4 A stream plot showing the trajectory of the equations of motion given a fixed ocean temperature of $\theta_o = 0.01$, $\sigma_0 = 535$, $\kappa = 11$, and $\lambda_A = 0.2$. The black cross denotes the fixed point of the system, with the colour gradient line depicting the variations of the fixed point with ocean temperatures. The green line shows the convection parameterisation. 84

5.5 Variations of the upper-level PV Q_A, the boundary layer PV Q_B, and the ocean temperature θ over a 20-day period are denoted in green, purple, and orange, respectively, with parameters $\sigma_0 = 535$, $\kappa = 11$, $c = 0.006$, $\gamma = 0.2$, and $\lambda_A = 0.2$. 86

5.6 Phase plot of the trajectory with parameters $\sigma_0 = 535$, $\kappa = 11$, $c = 0.006$, $\gamma = 0.2$, and $\lambda_A = 0.2$. The colours along the trajectory denote the time since its initialisation, as denoted by the green cross. 86

5.7 Lorenz map showing consecutive extrema for all variables. When θ, Q_B, or Q_A leads, the plot is in orange, purple, or green, respectively. Parameters are set to $\sigma_0 = 535$, $\kappa = 11$, $c = 0.006$, $\gamma = 0.2$, and $\lambda_A = 0.2$ 88

5.8 Phase plot of the three-box model with the instantaneous dimension (left) and persistence (right) shown in colour. Parameters were set to $\sigma_0 = 535$, $\kappa = 11$, $c = 0.006$, $\gamma = 0.2$, and $\lambda_A = 0.2$. 89

5.9 Fixed points of the three-box model with variations in the convection strength σ_0. Black and red points show stable and unstable fixed points respectively. Parameters are set to $\sigma_0 = 535$, $\kappa = 11$, $c = 0.006$, $\gamma = 0.2$, and $\lambda_A = 0.2$. 90

5.10 Plot showing the average period of oscillation, shown in navy, and the average difference between successive maxima and minima with changes in control parameters. The upper-level PV, boundary layer PV, and ocean temperature are shown in green, purple, and orange, respectively. Parameters are set to $\sigma_{00} = 535$, $\kappa = 11$, $c_0 = 0.006$, $\gamma_0 = 0.6$, and $\lambda_{A0} = 0.2$ when they are not undergoing modification. 91

5.11 Bifurcation diagram of the three-box model with variations in the convection strength σ_0, including a zoomed-in region indicated by the light blue box. The largest Lyapunov exponent is plotted in red. Parameters are set to $\kappa = 11$, $c = 0.006$, $\gamma = 0.2$, and $\lambda_A = 0.2$ 93

6.1 The mean of variable X with small changes in parameter a for a logistic map, taken from Lorenz (1964) Fig. 3. 104

6.2 Fig. 1 from Oertel et al. (2020), showing the diabatic effect of PV through the interaction of horizontal vorticity and the horizontal gradient of heating across the cold front of the cyclone. Here ω_h is the horizontal vorticity vector. 106

List of Acronyms

AMO Atlantic Multi-decadal Oscillation.

AMOC Atlantic Meridional Overturning Circulation.

CAO Cold Air Outbreak.

CMIP Coupled Model Intercomparison Project.

DJF December, January, February.

ECMWF European Centre for Medium-Range Weather Forecasts.

ENSO El Niño Southern Oscillation.

GCM Global Circulation Model.

GS Gulf Stream.

IFS Integrated Forecast System.

JJA June, July, August.

LIM2 Louvain-la-Neuve sea Ice Model.

MJJASO May, June, July, August, September, October.

MOC Meridional Overturning Circulation.

NA North Atlantic.

NAO North Atlantic Oscillation.

NDJFMA November, December, January, February, March, April.

NEMO Nucleus for European Modelling of the Ocean.

NH Northern Hemisphere.

PV Potential Vorticity.

rhs right-hand side.

SLHF Surface Latent Heat Flux.

SPPT Stochastically Perturbed Physical Tendency.

SSHF Surface Sensible Heat Flux.

SST Sea Surface Temperature.

WBC Western Boundary Current.

WCB Warm Conveyor Belt.

Chapter 1

Introduction

1.1 Motivation

The ocean-atmosphere system is a complex coupled relationship. These two domains operate primarily on different timescales, with atmospheric timescales spanning days, whereas the ocean operates on monthly to decadal timescales and even longer. Coupling between these two domains allows for a broad spectrum of variability to exist in both, complicating the causal responsibility of weather phenomena, ocean circulation, and global warming. Therefore, in order to fully comprehend either domain, it is imperative to study them together; otherwise, we risk overlooking emergent behaviour as a result of their inherent interdependence.

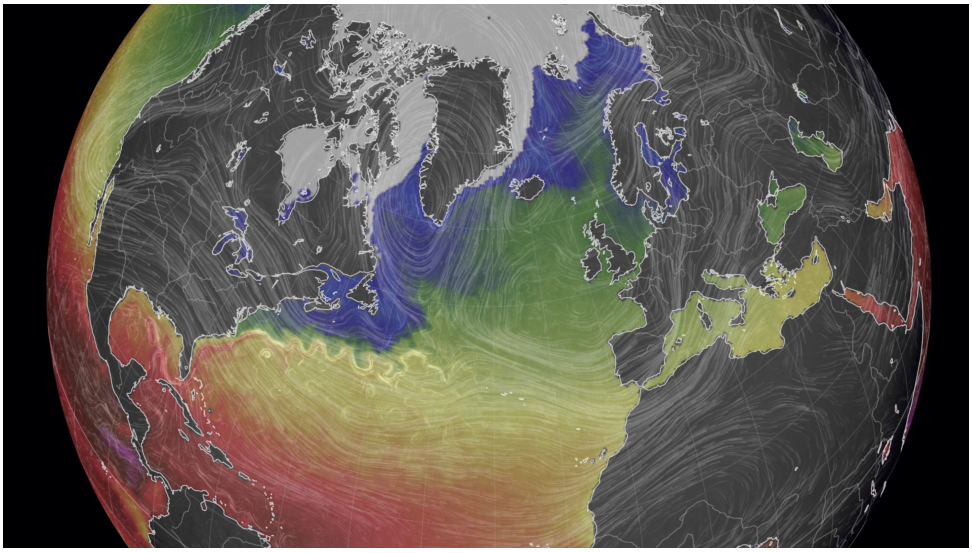


Figure 1.1: Observational data of the North Atlantic sea surface temperatures shown in coloured shading on the 7^{th} of May 2024 taken from `https://earth.nullschool.net`. The winds at 250hPa are shown with the grey streamlines and the ocean surface currents are shown with the white streamlines.

The focus of this work is on a weather phenomenon known as atmospheric blocking. This phenomenon results from a wave break in the atmospheric jet stream, depositing an anticyclone vortex, as seen at the southern tip of Greenland in Fig. 1.1, and is often associated with extreme weather events. These weather extremes range from heat waves to cold spells and droughts to flooding, depending on the location of a region relative to the blocking anticyclone, as illustrated in Fig. 1.2. Depending on the intensity and persistence of these events, their presence can put enormous stress on a society, leading to crop failure, hospitalisations, and increased mortality. Therefore, accurate prediction of atmospheric blocking episodes is of utmost importance so that precautionary measures can be taken to prepare for any extreme weather events associated with it. Despite their potentially devastating impacts on society, atmospheric blocks have yet to be adequately represented in models (Davini et al. 2021). This is likely due to a lack of comprehensive theory encompassing all the processes that contribute to their onset, maintenance, and decay, resulting in Global Circulation Models (GCMs) under-representing certain physical processes that initiate or extend an atmospheric block's life cycle. This is increasingly concerning because of the uncertainty regarding how their frequency and intensity may change in the future as a response to climate change. Woollings et al. (2018) showed a decreasing trend due to global warming, although this signal is weaker than both the model's atmospheric blocking bias and the decadal variability of blocking seen in observations.

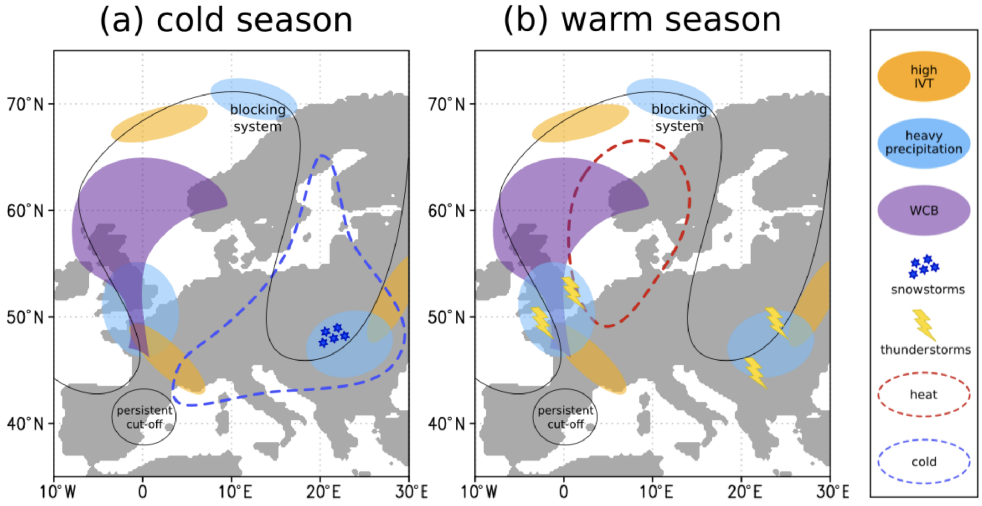


Figure 1.2: Fig. 2 from Kautz et al. (2022) showing a wave breaking in the jet stream illustrated by the thin black contour representing an upper-level geopotential height contour. Hot and cold extremes exist inside the red and blue dashed contours, respectively. Regions of high integrated water vapor transport, heavy precipitation, and warm conveyor belt ascent are shown in orange, blue, and purple shading, respectively. Snow and thunderstorms are shown in blue stars and lightning bolts, respectively.

Recently, the ocean has received interest as a potential modulator of atmospheric blocking variability. Although it is commonly agreed that the atmosphere primarily drives the ocean on subannual timescales in mid-latitudes, as shown by Frankignoul & Hasselmann (1977), and that the ocean drives the atmosphere in the tropics, particularly through processes such as El Niño, recent observations suggest that the ocean plays a role in driving the atmosphere in mid-latitudes (Minobe et al. 2008, Häkkinen et al. 2011, O'Reilly & Czaja 2015, O'Reilly et al. 2016, Sheldon et al. 2017, Famooss Paolini et al. 2022, Kolstad & O'Reilly 2024), particularly over the western boundary currents (WBCs). This confirmed coupling between the atmosphere and the ocean in the mid-latitudes coincides with the emergence of high-resolution models that can properly resolve the frontal and mesoscale interactions that manipulate storm track position and intensity as well as air-sea heat fluxes. These two processes affect baroclinicity and static stability in the atmospheric boundary layer (Bennetts & Hoskins 1979), triggering slant-wise convection (Emanuel 1983) that impacts the entire troposphere (Minobe et al. 2008), as illustrated in Fig. 1.3.

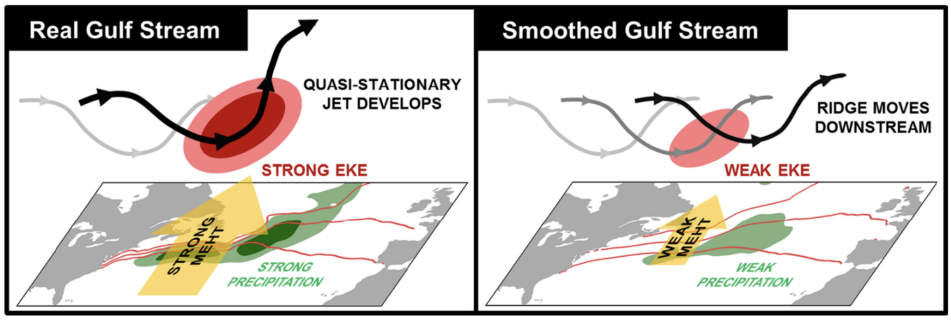


Figure 1.3: Fig. 17 from O'Reilly et al. (2016) showing a schematic of the effect of Gulf Stream frontal sharpness on the development of a ridge in the atmospheric jet stream. The jet stream is shown in black and grey arrowed contours, while the sea surface temperature (SST) contours are shown in red, with the real and smoothed SST gradient results shown on the left and right, respectively. Precipitation and eddy kinetic energy are shown in green and red shading, while meridional heat transport is represented by a yellow arrow.

With the influence of WBCs on the upper troposphere now being observed and tested in GCMs, the role of feedbacks is becoming increasingly important in understanding variability across a range of timescales. As discussed by Strogatz (2018), systems that exhibit chaotic behaviour display non-periodicity and, therefore, contain a broad range of timescales. Although atmospheric timescales are typically on the order of days, the ocean operates on timescales of months to years. Hence, any coupling between these two domains will result in timescales external to both (Czaja & Marshall 2001). Understanding how oceanic signals propagate

through the storm track and to the jet stream, and, in turn, understanding how the jet stream affects heat fluxes from the ocean to the atmosphere, as well as ocean currents, is key to properly quantifying the feedbacks between these domains, and hence the resulting variability in each.

1.2 Thesis Outline

This thesis uses observational, reanalysis, and model output to observe and quantify the link between the Gulf Stream and atmospheric blocking over the North Atlantic and throughout the Northern Hemisphere. It is laid out as follows. In Chapter 2, the background physics related to atmospheric blocking, air-sea coupling, and chaos theory is discussed. Chapter 3 is a study linking the Gulf Stream to atmospheric blocking through observational and reanalysis data in both the oceanic and atmospheric domains. The causal nature of this link is then tested using a sensitivity experiment with a high-resolution GCM in Chapter 4, and the strength of the Gulf Stream's influence on the upper troposphere is quantified and compared across numerous resolutions. The coupled interaction between the Gulf Stream and the North Atlantic jet stream is abstracted into a simple heuristic model in Chapter 5, from which the importance of certain physical processes and feedbacks can be addressed. Details about data sets, model setup, and analysis techniques are described separately in each chapter. Chapter 6 summarises the conclusions from each study and includes some discussion on the application of these findings along with avenues for future research.

Chapter 2

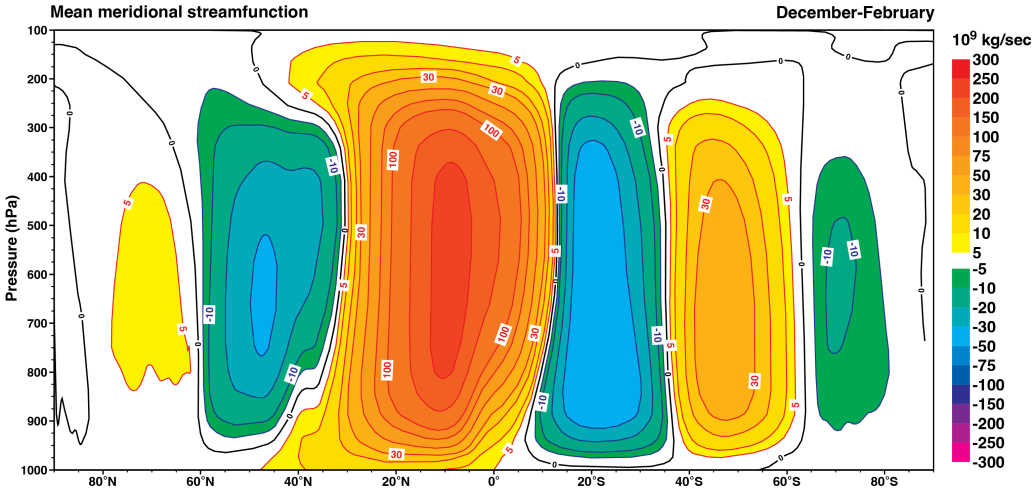
Background Theory

2.1 The Jet Stream

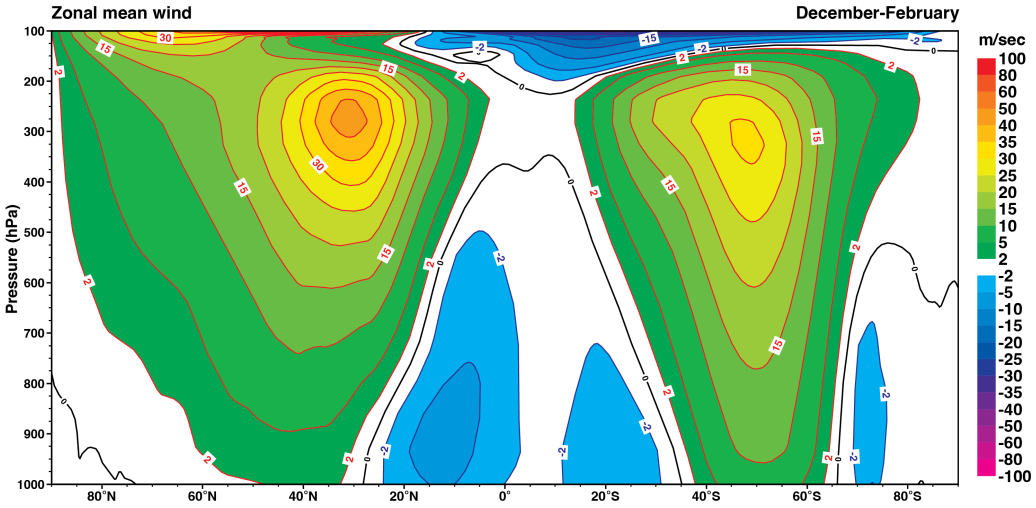
2.1.1 The General Circulation of the Troposphere

The Earth's general circulation is driven by differential heating, with the equator receiving more radiative energy from the Sun than the poles. This imbalance causes warm air to rise at the equator and move poleward in an attempt to reduce the temperature contrast, as described by Hadley (1735) in his model of atmospheric circulation. The rising equatorial air forms part of the Hadley cell, as seen either side of the equator in Fig. 2.1, which transports heat to the poles. As the air moves poleward, its radial distance from the Earth's axis of rotation decreases, requiring it to accelerate eastwards to conserve angular momentum. Eventually, this air reaches its maximum speed due to instabilities, forming the subtropical jet stream in the upper troposphere. This air, having cooled during its journey, descends to the lower troposphere where it either moves poleward, joining the Ferrel circulation, or returns equatorward. In conserving angular momentum, the equatorward-moving air becomes easterly, forming the trade winds.

There are typically two jet streams in the winter hemisphere on Earth: the subtropical jet and the mid-latitude jet. In contrast, the mid-latitude jet is not primarily thermally driven, as it resides on the poleward side of the Ferrel cell, where air rises at higher latitudes and subsides at lower latitudes. Instead, the mid-latitude jet is powered by the convergence of eastward momentum generated by the presence of eddies, as discussed by Kuo (1951). In this region, baroclinic disturbances at lower levels of the atmosphere produce eddies. Due to the



(a) Meridional Transport



(b) Zonal Wind

Figure 2.1: The December, January, February (DJF) climatology of the meridional transport (top) and zonal wind (bottom) from ERA-40 Atlas (Sterl & Caires 2005).

conservation of vorticity, this process reduces the vorticity outside this region, subsequently creating westward momentum. The conservation of angular momentum leads to the influx of eastward momentum into the eddy-filled area, ultimately giving rise to the mid-latitude or eddy-driven jet. However, these two jet streams are not absolute and constantly vary in intensity and position and frequently merge (Madonna et al. 2017).

The main modes of variability in the mid-latitude jet stream are the annular modes. These describe a large proportion of the geopotential height variance that occurs in either hemisphere. They are characterised by a north-to-south shift of mass in the atmosphere from the poles to the mid-latitudes, resulting in changes in pressure fields and jet stream strength and position. Of particular importance for this study is the North Atlantic Oscillation (NAO), which is the

main mode of variability in the North Atlantic and is closely related to the Northern Annular Mode. This mode is measured by Hurrell et al. (2003) as the pressure difference between the Azores and Iceland. During a positive NAO phase, stronger westerlies are expected in the mid-latitudes, whereas a negative phase coincides with weaker westerlies.

2.1.2 Rossby Waves

Rossby waves, or planetary waves, are atmospheric waves in which zonal flow is perturbed, leading to periodic increases and decreases in meridional transport with respect to longitude. These waves result from the conservation of potential vorticity (PV) on a beta plane (a surface where the Coriolis force varies linearly with latitude). Rossby waves have a strong influence on mid-latitude weather and, when they exhibit quasi-stationary behaviour, are often associated with compound events across the hemisphere (Kautz et al. 2022). As theorised by Rossby (1939), these waves travel westward relative to the background flow, U, and propagate faster with longer wavelengths, as indicated by the dispersion relation.

$$\omega = Uk - \frac{\beta k}{k^2 + l^2}. \tag{2.1}$$

Here, ω is the frequency of the oscillation, k and l are the wave numbers in the zonal and meridional directions, respectively, and β is the rate of change of the Coriolis parameter with respect to the meridional direction. From this relation, it can be shown that the phase speed in the zonal direction, $c_p = \omega/k$, is zero, i.e., stationary Rossby waves, when $U = \frac{\beta}{k^2+l^2}$. Therefore, knowledge of the background flow and mechanisms for wave number resonance offers potentially powerful predictive tools for synchronised extreme events in the future (Petoukhov et al. 2013, Coumou et al. 2014).

Conceptually, we can understand the movement of these waves using a thought experiment, the setup of which is illustrated in Fig. 2.2. This figure shows consecutive high- and low-pressure systems, shown in blue and red, respectively, creating a planetary wave that wraps around the northern hemisphere. The flow of the jet stream is shown with the grey contour. Now imagine the movement of air from position **N**. This air mass is neutral, as it is equidistant from both the high-pressure and low-pressure systems, and hence it has no relative spin. However, this

air mass is in the flow of the jet stream and hence will move with it. In the case of the leftmost neutral air mass, this air moves equatorward. As it moves, it experiences a stretching of its relative vorticity vector in the direction of the Earth's spin, and hence this vorticity will increase (Hoskins 1997), as detailed by the second term on the right-hand side (rhs) of the adiabatic vorticity equation in a rotating frame:

$$\frac{D}{Dt}\left(\frac{\boldsymbol{\zeta}}{\rho}\right) = \frac{(\boldsymbol{\zeta}.\nabla)\boldsymbol{u}}{\rho} + \frac{\nabla\rho \times \nabla p}{\rho^3}, \tag{2.2}$$

where $\boldsymbol{\zeta} = f\hat{\boldsymbol{k}} + \boldsymbol{\zeta}_r$ is the vorticity vector, comprised of the Coriolis parameter and the relative vorticity vector, $\boldsymbol{u}$ is the velocity vector, ρ is the density of air and p is the pressure. The stretched vorticity vector is shown in green in the thin layer of the atmosphere on the edge of the globe. Hence, as it moves equatorward, it accumulates some anticlockwise (cyclonic) spin and generates a low-pressure anomaly. The opposite is true for air masses moving poleward, as illustrated by the middle neutral air mass in Fig. 2.2.

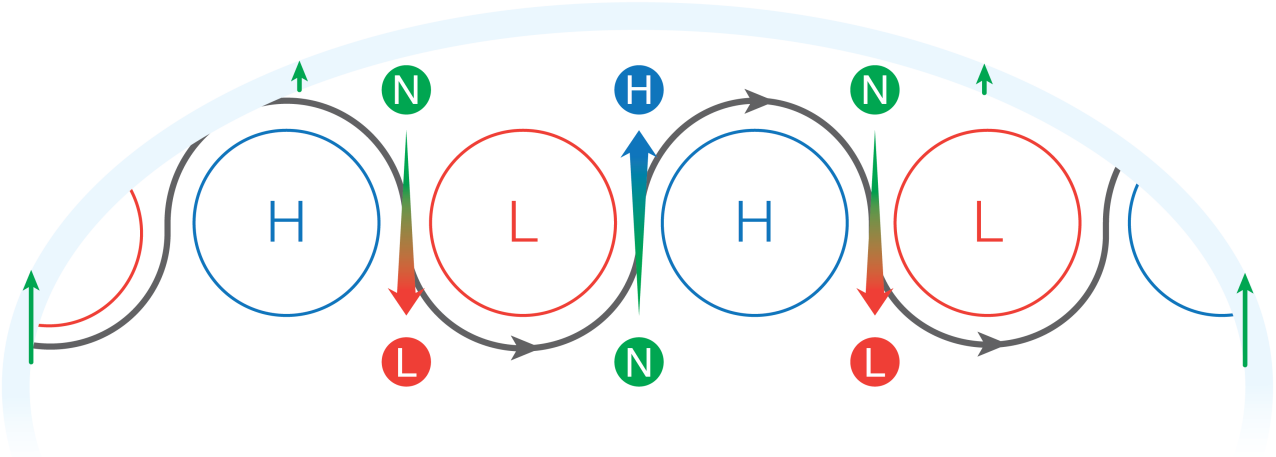


Figure 2.2: Schematic of Rossby wave propagation. Low and high-pressure systems are illustrated in red and blue, respectively, while neutral air is depicted in green. The grey line shows the flow of air along the jet stream. A section of the Earth's atmosphere is shown in a light blue fill, with the vorticity of the neutral air shown with the green vectors inside it.

As detailed in Fig. 2.2, the movement of this neutral air tends to deposit anomalous air of the same sign on the western flank of the already established anomaly, resulting in the creation (destruction) of that anomaly on the western (eastern) flank, resulting in the propagation of the Rossby wave to the west. As indicated by Equation 2.1, the phase speed of the wave in the zonal direction depends on the size of the Rossby wave, with larger zonal wavelengths leading

to faster westward propagation. To illustrate this, imagine again the same wave seen in Fig. 2.2, but now the zonal wave number is smaller, that is, the high- and low-pressure systems are larger and occupy more of the northern hemisphere. Again, moving a neutral air mass meridionally with the flow of the jet stream will result in anomalous air being deposited on the western side of the high- and low-pressure systems; however, since these pressure systems are larger, the neutral air mass must move a farther distance meridionally. This results in a larger anomaly being created and hence a faster propagation to the west.

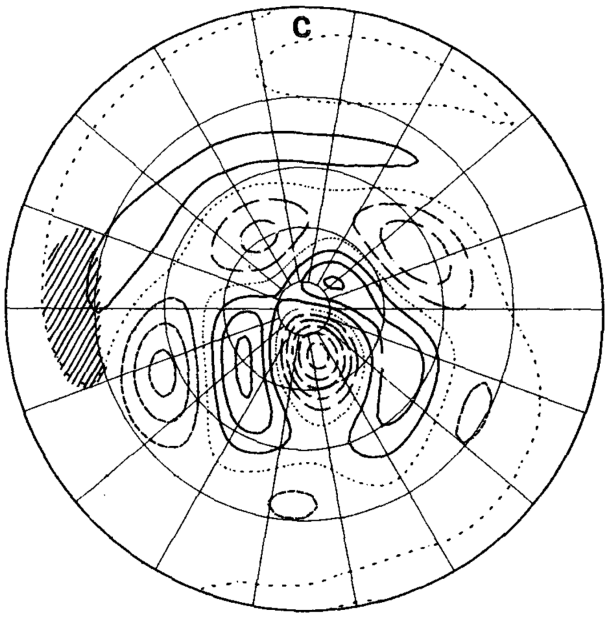


Figure 2.3: Fig. 3 from Hoskins & Karoly (1981) showing the geopotential height anomalies as a result of heating in the mid-troposphere. The hashed mask indicates the region being heated, while solid and dashed contours show positive and negative geopotential height anomalies, respectively.

Understanding the behaviour of these waves leads to the following question: How do they arise? Primarily, these Rossby waves arise due to forcing from orography or asymmetric heating (Hoskins & Karoly 1981). Charney & Eliassen (1949) was the first to test the role of orography in a simple model, finding the existence of large-scale quasistationary waves as a result of forced ascent over continental landmasses. Imagine a simple vertically stratified atmosphere: when there is a mountain range, the layers in the atmosphere are squeezed closer together. This also shrinks the vorticity vector and results in anticyclonic circulation. Similarly, when this mountain range subsides, the vorticity vector is stretched again, and cyclonic circulation occurs. This starts a Rossby wave train that propagates locally from mountainous regions. Similarly, Hoskins & Karoly (1981) showed that wave trains originate from regions of heating, as seen in

Fig. 2.3, with anticyclonic circulation occurring on the downstream flank of a heated region while cyclonic circulation occurs on the upstream flank. Using the same vorticity argument, this heating acts to increase the distance between isotherms and hence stretch (squash) the vorticity vector upstream (downstream) of a heated region. Therefore, it has the opposite effect to that of orographic forcing.

2.2 Atmospheric Blocking

2.2.1 The Importance of Atmospheric Blocking

Atmospheric blocking refers to a persistent, quasistationary anticyclonic anomaly in the mid to high latitudes that blocks the background westerly flow. Atmospheric blocks are important due to their modification of regional precipitation, temperature, and weather regimes (Rex 1950, Grams et al. 2017), as seen in Fig. 1.2. This is particularly relevant in a warming climate, as blocked flows are often associated with extreme temperatures, generating co-located high-temperature anomalies and low-temperature anomalies on the eastern and western boundaries (Pfahl & Wernli 2012). During summer, the presence of a blocking anticyclone leads to cloud-free skies, resulting in persistent warming due to incoming shortwave radiation, which can cause and exacerbate heat waves. Conversely, in winter, the advection of cold polar air equatorward primarily drives the associated cold spells. As well as temperature extremes, blocking systems are associated with droughts and flooding, depending on their location relative to the storm track (Kautz et al. 2022). Therefore, accurate understanding and prediction of these systems has major implications for early warning systems and mitigating the effects of these systems.

There are many different ways of measuring an atmospheric block, all of which pick up on different aspects of blocking (Barnes et al. 2012). For example, Tibaldi & Molteni (1990) use the reversal of 500 hPa geopotential height as a blocking indicator, which is suggestive of Rossby wave breaking in the jet stream. Similarly, Pelly & Hoskins (2003) suggested measuring the reversal of meridional potential temperature gradients along upper-level PV surfaces. Of particular interest for this work is the index of Schwierz et al. (2004), which defines a block as a negative PV anomaly between the midtroposphere (500 hPa) and the lower stratosphere (150 hPa) that exceeds a certain amplitude, overlap, spatial scale and duration. Fig. 2.4 shows the seasonal atmospheric blocking frequency as measured by this index. This shows that

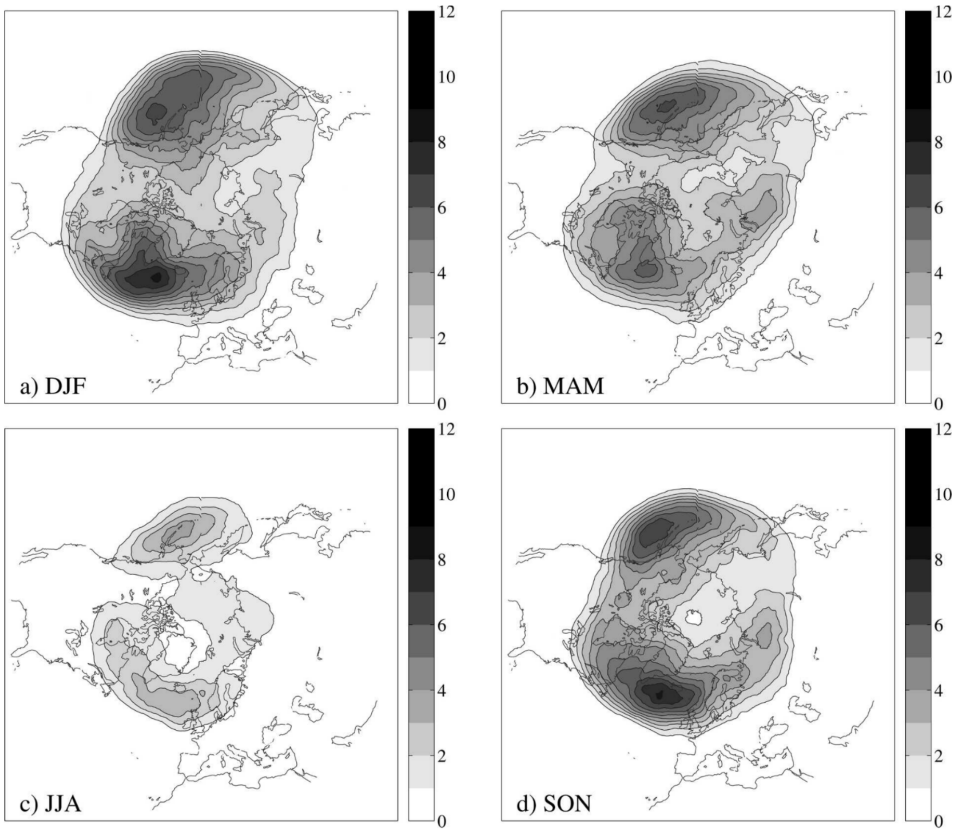


Figure 2.4: Fig. 2 from Croci-Maspoli et al. (2007) showing the seasonal atmospheric blocking climatology using the PV anomaly index from Schwierz et al. (2004). The colour shading depicts the frequency of atmospheric blocking.

atmospheric blocking is most common during December, January, and February (DJF) and least prevalent during June, July, and August (JJA) in the Northern Hemisphere. Additionally, it is preferentially located over the two main ocean basins, the North Atlantic and North Pacific.

The numerical prediction of atmospheric blocking dates back to Charney & DeVore (1979), who showed that their simple baroclinic model with orographic forcing possessed three fixed points: one related to zonal flow with small Rossby wave amplitude, one blocked flow with large Rossby wave amplitude, and a final intermediate state, suggesting that these states are likely metastable in the real atmosphere. Blocking representation has greatly improved since then, although modern models tend to underestimate blocking frequency and interannual variability (Davini et al. 2021). These recent improvements in blocking representation have primarily been related to increased atmospheric and oceanic horizontal resolution, as well as improvements in the mean biases in the models (Scaife et al. 2010).

Of urgent importance is understanding how blocking events will change in a warming climate. Both Woollings et al. (2018) and, more recently, Dorrington et al. (2022) have reported

a decrease in blocking frequency and less persistent blocking regimes in the Coupled Model Intercomparison Project (CMIP) models under the RCP 8.5 scenario, although the signal is relatively weak and exhibits a complex spatial pattern. The driver of this trend is often cited as a tug-of-war between Arctic amplification at lower levels in the troposphere (the rapid heating of the Arctic compared to global mean temperatures) and upper-level tropical heating. Both effects change the resulting meridional temperature gradient, but in opposite directions, and hence the zonal flow and amplification of Rossby waves. However, the projected trends of blocking frequency are both weaker than the models' atmospheric blocking biases and the decadal variability of blocking seen in observations, leading to low confidence in these projections.

With blocking now understood in a broader context, the next key question is: how do blocks form? The lack of a clear theoretical framework for their onset, maintenance, and decay has contributed to their underrepresentation in GCMs. Enhancing our understanding of these mechanisms will undoubtedly help reduce model bias and increase confidence in the projected changes in blocking patterns due to climate change. Until recently, blocking was thought to be a purely "dry" phenomenon, with no influence of diabatically modified air on the upper-level flow. However, nearly a decade ago, it was discovered that moist processes, particularly latent heating, significantly impact atmospheric blocks. The roles of both "dry" and moist processes are discussed in the following sections.

2.2.2 Dry Processes

In the simplest onset scenarios, subtropical air rapidly moves poleward, and due to shrinking vorticity vector, as discussed in Section 2.1.2, this air mass becomes anticyclonic, forming a block. However, since this anticyclonic anomaly isn't part of a larger Rossby wave, it doesn't propagate against the background flow and is likely to continue downstream unless interrupted by another mechanism. One theory that explains the quasi-stationarity of such anomalies is the selective absorption mechanism proposed by Yamazaki & Itoh (2013). This theory suggests that blocking anticyclones absorb smaller-scale upstream anticyclones, increasing the block's mass and helping to maintain it, while cyclonic anomalies are repelled from the block, as also observed by Hauser et al. (2023). Additionally, Shutts (1983) demonstrated that introducing an eddy source in a simple barotropic model with weak zonal flow led to a dipole block. These eddies reinforce the blocking pattern by deforming as they approach the block from upstream. These

two theories describe the energy cascade from the synoptic scale to the planetary scale, with baroclinic sources, such as storm tracks, acting as key contributors to blocking maintenance.

As well as lone anticyclonic anomalies, blocks may be part of a larger Rossby wave, such that this Rossby wave becomes stationary with respect to the Earth (Held 1983). As described by the dispersion relation in Equation 2.1.2, stationary Rossby waves occur when there is a balance between the background flow and the wavelength of the Rossby wave, with lower background speed and higher wavelength leading to more stationarity generally. This feature was observed by Riboldi et al. (2020), who showed more blocking when the Rossby phase speed was low. This also coincided with weak background flow. Additionally, blocks can form from the superposition of multiple Rossby waves of different wavelengths (Austin 1980) or the interaction of Rossby waves with the background flow Charney & DeVore (1979).

The decay stage of a block has often been considered to be a result of long-wave radiative cooling Harvey et al. (2020), although the breakdown of maintenance processes is also suspected to be of major importance in the life cycle of these phenomena (Hauser et al. 2023).

2.2.3 Moist Processes

The first observation of moist processes being important for atmospheric blocking formation and maintenance came from Pfahl et al. (2015). Using Lagrangian analysis, they found that between 30%-40% of the air in a block had been heated by more than 2K, primarily due to latent heating along the fast-ascending air streams from lower levels to the upper troposphere. Later, Steinfeld & Pfahl (2019) found that this air is deposited through a series of transient cyclones, ascending in the warm sector of the cyclone in an airstream known as the Warm Conveyor Belt (WCB). This air has anomalously low PV when entering the upper troposphere and hence contributes to the formation and maintenance of the atmospheric block. Additionally, this air is primarily deposited on the western poleward flank of the block, as seen in Fig. 1.2, amplifying the ridge and further advecting the block westward against the background flow.

Testing the importance of this moist airstream, Steinfeld et al. (2020) performed a sensitivity experiment in which latent heating was suppressed along the WCB of a cyclone that was seen to contributed to the formation of a block. This resulted in the size, intensity, and duration of several blocks being reduced, while others failed to form at all. Steinfeld et al. (2022) then

showed that the role of moist processes in a warmer climate becomes increasingly important compared to "dry" processes. They observed, contrary to the projections of Woollings et al. (2018) and Dorrington et al. (2022), an increase in blocking size and intensity due to the increased contribution of moist processes, with a slight increase in frequency. This is due to the more moisture in the atmosphere in a warmer climate as a result of the Clausius-Clapeyron relation, and hence more transport from lower levels due to increased latent heating.

2.3 Ocean-Atmosphere Coupling

Coupling between the ocean and atmosphere involves the interaction of two domains that primarily operate on vastly different timescales, resulting in complex variability across a range of frequencies. Bjerknes (1964) was among the first to investigate this interaction, examining how the ocean's heat content is modulated by radiation, sensible and latent heat fluxes, and heat convergence due to oceanic transport. The majority of short timescale heat content change occurs in the ocean's upper layer, known as the mixed layer, while the deep ocean contributes far less to ocean-atmosphere coupling. However, heat can also enter the mixed layer from below, primarily through entrainment of deeper waters into the mixed layer. Additionally, ocean currents, modulated by wind stress, primarily act within the oceanic mixed layer and play a role in heat convergence. This wind stress can act horizontally through Ekman transport or vertically through Ekman pumping (Gill 1982, Chapter 9). Understanding how oceanic heat content both affects and is affected by the atmosphere is key to grasping this complex interaction.

2.3.1 Air-Sea Heat Fluxes

Bjerknes (1964) found that the strength of the heat flux from the ocean to the atmosphere depends on Sea Surface Temperatures (SSTs), T_o, atmospheric temperature at the air-sea interface, T_a, and wind speed, U. The heat flux into the atmosphere is given by the bulk formula, Equation 2.4.5 from Gill (1982):

$$Q_s = c_H \rho_a C_p U (T_o - T_a), \tag{2.3}$$

where Q_s is the Surface Sensible Heat Flux (SSHF) (the heat transfer due to temperature differences at the air-sea interface), ρ_a is the atmospheric density, C_p is the heat capacity of the atmosphere, and c_H is the Stanton number. Surface Latent Heat Flux (SLHF) is described by Equation 2.4.6 from Gill (1982):

$$Q_l = c_E \rho_a C_p U (q_o - q_a), \tag{2.4}$$

where Q_l is the SLHF (the heat transfer due to evaporation at the air-sea interface), c_E is the Dalton number, and q is the specific humidity. In this case, the ocean's specific humidity is assumed to be the saturation value of the atmosphere at the given SST.

Bjerknes (1964) hypothesized that the atmosphere drives short-term ocean temperature anomalies (sub-annual), while the ocean forces the atmosphere on longer timescales (decadal). Frankignoul & Hasselmann (1977) tested this theory, showing that ocean SSTs exhibit decadal variability when forced by a stochastic atmosphere. Numerous studies have supported the weak correlation between SSTs and air-sea heat fluxes, compared to the stronger correlation between atmospheric temperatures and air-sea heat fluxes for short-term variability, confirming that atmospheric processes primarily drive air-sea heat exchanges on these timescales (Bjerknes 1964, Frankignoul 1985, Kolstad et al. 2009).

2.3.2 Oceanic Mixed Layer Dynamics

The ocean's mixed layer depth is modulated by the amount of incoming solar radiation, heat fluxes between the ocean and atmosphere and wind-driven stirring. Heat loss to the atmosphere both cools and increases the salinity of the water at the top of the mixed layer, making it denser. This denser water then sinks, initiating convection that entrains deeper waters into the mixed layer. This explains why the mixed layer deepens during autumn, coinciding with a decrease in solar radiation and increased atmospheric storms (Kraus & Turner 1967). Cayan (1992) demonstrated that mixed layer depth can be approximated by the strength of air-sea heat flux, suggesting that this is the primary driver of mixed layer variability. If the water below the mixed layer is warmer than the mixed layer itself (though not necessarily less dense due to salinity differences), it is entrained into the mixed layer as it deepens, increasing its heat content. Consequently, as the mixed layer becomes deeper, the ocean's heat capacity increases,

which dampens the rate of change of SSTs for the same heat flux.

Assuming that the mixed layer is well-mixed (with approximately constant temperature and salinity throughout), these dynamics can be described by Equation 2 from Frankignoul (1985):

$$\frac{\partial T_o}{\partial t} + \boldsymbol{u}_H \cdot \boldsymbol{\nabla} T_o + \frac{(T_o - T_+)w_e}{h} - \kappa \nabla^2 T_o + \frac{Q - Q_+}{\rho h C_p} = 0,$$

where T_o is the temperature of the ocean mixed layer, assumed to be equal to that of the SSTs, $\boldsymbol{u}_H$ is the horizontal velocity, w_e is the entrainment velocity, κ is the diffusion coefficient, ρ is the density of the ocean, h is the height of the mixed layer, Q is the heat flux, and the $+$ subscript refers to quantities just below the mixed layer depth. The second and third terms describe the change in temperature resulting from transport within and into the mixed layer, respectively, the fourth term describes the effects of diffusion, while the final term accounts for heat fluxes in and out of this volume both at the surface and at the bottom boundary of the mixed layer.

2.3.3 Ocean Current Dynamics

In the ocean, water circulates around the globe through the ocean conveyor belt, a system of interconnected currents that transport heat, salinity, and nutrients. This thermohaline circulation comprises fast surface currents, downwelling and upwelling, and slow deep ocean currents. As seawater moves poleward at the surface, it cools, and some of it freezes, leaving behind any salt it contained. Hence the remaining water becomes saltier and therefore denser. This dense water sinks and travels along deep ocean currents that follow geostrophic flow, eventually upwelling approximately 1,000 years later, often in the Antarctic, before rejoining the fast surface currents (Primeau 2005). This global process is known as the Meridional Overturning Circulation (MOC), with the Atlantic Meridional Overturning Circulation (AMOC) being a major component (McCarthy et al. 2015).

Surface ocean currents are primarily driven by wind stress. In the Northern Hemisphere, the Coriolis effect deflects surface currents at a 45° angle to the right of the wind direction, as described by Ekman (1905). This deflection continues through the Ekman layer, producing an Ekman spiral, where the net water transport occurs at right angles to the wind. If the wind stress has curl, it causes horizontal convergence or divergence of mass. For instance, anticyclonic

wind stress leads to convergence, resulting in downward movement (Ekman pumping), while cyclonic wind stress induces divergence and upwelling. These processes regulate the heat flux at the base of the mixed layer.

On a basin scale, Stommel (1948) demonstrated that the trade winds and jet streams generate anticyclonic ocean gyres, with variations in $\frac{\partial f}{\partial y} > 0$ concentrating streamlines along the western boundary of ocean basins. Here, f is the Coriolis parameter, and y is the meridional coordinate. This creates Western Boundary Currents (WBCs), such as the Gulf Stream (GS) and the Kuroshio Current. Welander (1968) expanded on this by showing that the latitudinal variation in $\frac{f}{H}$, where H is the ocean depth, governs the shape of ocean gyres. These regions of intense flow often produce mesoscale ocean eddies, commonly referred to as ocean weather. These eddies, approximately 100 km in scale, arise from baroclinic instability in regions of strong flow (Gill et al. 1974).

2.3.4 Ocean-Atmosphere Coupling in the North Atlantic

Now with a broad understanding of ocean-atmosphere coupling, how does this manifest in the real world? Fig. 2.5 shows the SST anomalies for the positive phase of the NAO, taken from Cobb & Czaja (2019). A positive NAO phase represents a zonal weather regime while a negative phase resembles a blocking anomaly over Greenland (Grams et al. 2017). During positive NAO phase, wind speeds south of Greenland increase, leading to more heat being removed from the ocean, as indicated by Equation 2.3 and 2.4, and a decrease in SSTs. However, during the negative phase of the NAO, cold dry air is advected from the North American continent over the GS, primarily driving the air-sea heat flux in this region (Bjerknes 1964, Frankignoul 1985, Kolstad et al. 2009). Hence this SST pattern is primarily driven by the atmosphere.

The NAO also acts to generate Ekman transport in the North Atlantic, with the positive phase of the NAO increasing GS transport (Cobb & Czaja 2019), leading to a convergence of heat into the GS extension that acts as a positive feedback on the SST anomalies seen in Fig. 2.5 (Marshall, Johnson & Goodman 2001). Kelly (2004) observed that 26% of heat content variations in the ocean are due to changes in ocean circulation induced partly by wind stress. This is particularly prevalent in WBCs, where Kelly et al. (2010) observed that air-sea heat flux is closely related to heat convergence due to oceanic transport.

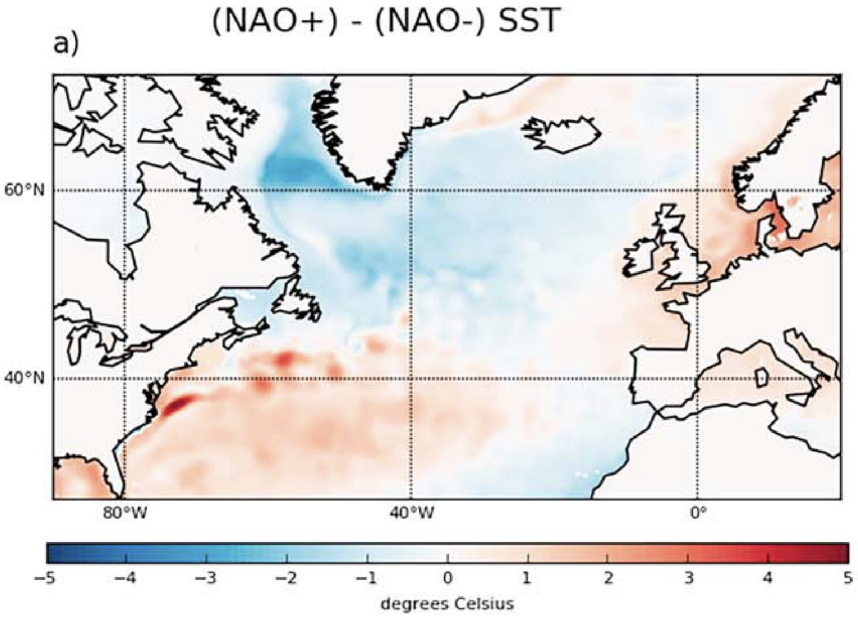


Figure 2.5: Fig. 1 from Cobb & Czaja (2019) illustrating the difference in sea surface temperatures (SSTs) between the positive and negative phases of the NAO, based on the NAO index defined by Hurrell et al. (2003).

Evidence has emerged suggesting that the ocean may force the atmosphere on shorter timescales. Rodwell et al. (1999) showed that much of the NAO variability could be reconstructed in GCMs using knowledge of past SSTs. Additional theory from Marshall, Johnson & Goodman (2001), theorising the NAO and ocean circulation as a delayed oscillator, recreates much of the low-frequency spectrum present in both the atmosphere and ocean. Observations of this coupling using spectral analysis soon appeared in the work of Czaja & Marshall (2001). Most recently, Kolstad & O'Reilly (2024) argued that North Atlantic SSTs in November causally force the NAO for DJF.

While it is clear how the atmosphere can modulate the ocean through heat fluxes and wind stress, it is less clear how the ocean can affect the upper troposphere through heat fluxes in the boundary layer. Minobe et al. (2008) showed the convergence of atmospheric boundary layer surface wind over the front of the GS, which coincided with localised precipitation. This precipitation suggests latent heating in the midtroposphere and cross-isentropic transport from the boundary layer to the upper troposphere. Using a high-resolution regional model, Sheldon et al. (2017) showed that the strength of this convection was dependent on the strength of the SST gradients, as well as the absolute value of the SSTs.

Notably, Bane Jr & Osgood (1989) observed stronger air-sea heat fluxes over the GS warm core

than over the continental shelf, contributing to low-level baroclinicity, which in turn generates vorticities, as seen from the last term on the rhs of the vorticity equation 2.2. Famooss Paolini et al. (2022) showed a strongly different response in coarsely resolved GCMs to GS front shifts compared to high-resolution (50 km or less) models. As in observations, northward shifts of the GS front resulted in more convergence of low-level air, leading to more upward transport as well as more meridional eddy heat transport. This, in turn, resulted in a northward shift in the jet stream, while in lower-resolution models, this process was much weaker, resulting in a southward shift of the jet. The importance of SST resolution for low-level baroclinicity and vertical transport was also observed by Parfitt et al. (2017).

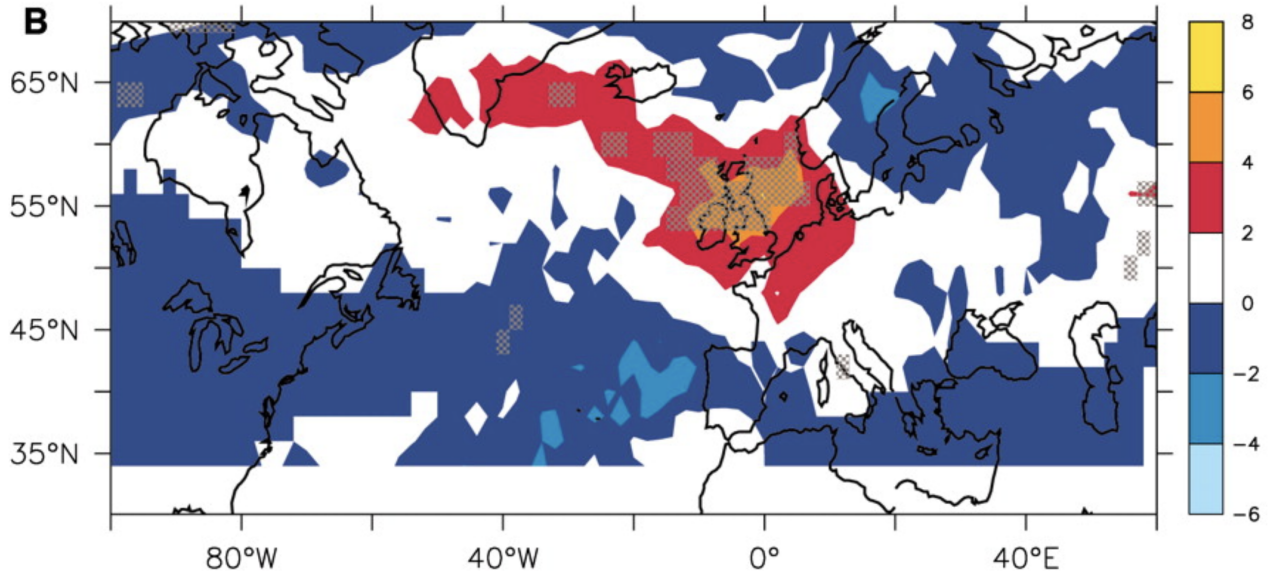


Figure 2.6: Fig. 4B from Häkkinen et al. (2011) showing the anomalous blocking frequency for a high Atlantic Multi-decadal Oscillation (AMO).

As discussed in Section 2.2.3, moisture is vital for the modification of atmospheric blocks. Undoubtedly, the ocean is the largest source of moisture for the atmosphere; however, Yamamoto et al. (2021) showed that the primary moisture uptake for atmospheric blocking particles in the Northern Hemisphere comes predominantly from WBCs. Furthermore, Wenta et al. (2024) observed that one fifth of a block's air mass interacted with the GS region, experiencing intense heating and moistening due to the frequent occurrence of cold air outbreaks (CAOs) in the cold sector of a series of cyclones. Additional evidence from O'Reilly et al. (2016) shows SST gradients act to maintain a block while also adding to its stationarity. Finally, Häkkinen et al. (2011) showed observational evidence that atmospheric blocking increases with the presence of warm waters in the GS extension on decadal timescales, as shown in Fig. 2.6.

2.4 Potential Vorticity

While it is evident that the atmosphere significantly influences the ocean, and the ocean simultaneously impacts the atmosphere across various timescales, additional diagnostic tools are required to effectively quantify this connection in the following chapters. To do this, we shall look at the quantity of potential vorticity (PV), described by Hoskins et al. (1985). PV is a scalar quantity that combines both the thermodynamics and dynamics of an air parcel. Knowledge of this quantity can be used to determine the flow of the fluid given sufficient boundary conditions, a process known as PV Inversion, which is described by Davis (1992). The quantity is fundamental to the field of geophysical fluid dynamics, in part because it is adiabatically conserved. As described in Gill (1982), Ertel's PV is:

$$Q = \frac{\boldsymbol{\zeta}.\nabla\theta}{\rho}, \tag{2.5}$$

where Q is the PV, $\boldsymbol{\zeta}$ is the relative vorticity vector, θ is the potential temperature and ρ is the density. Potential temperature is itself an adiabatically conserved quantity and is defined as the temperature a dry air parcel would have if the parcel were brought adiabatically to some reference pressure. Hence, if this air mass does not contain any water and is transported along isentropic surfaces, changing absolute temperature due to pressure differences, its potential temperature will be unchanged.

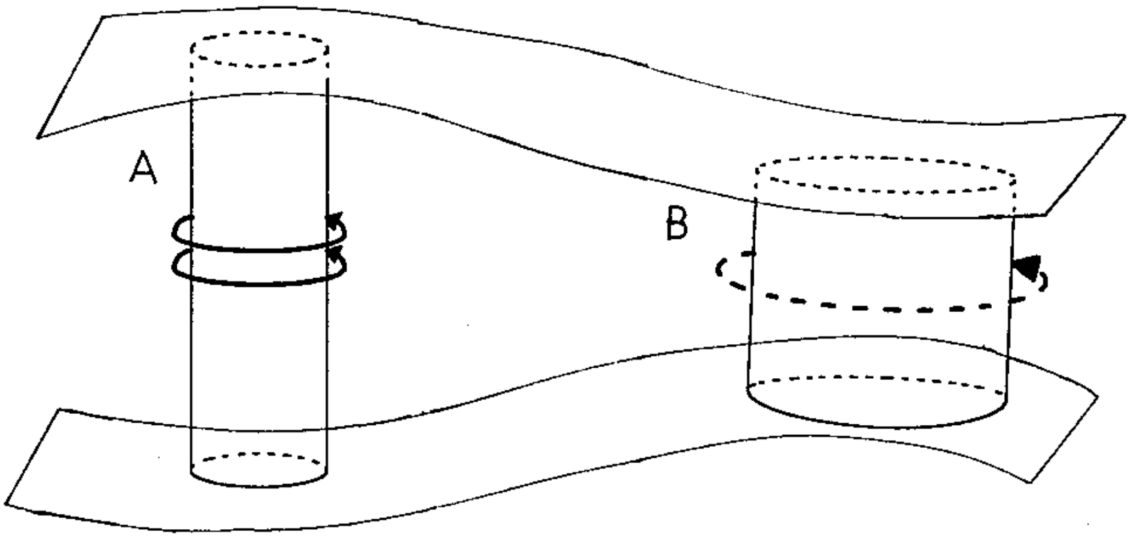


Figure 2.7: Vortex stretching between two isentropic surfaces, taken from Hoskins (1997), Fig. 4.

Since Ertel's PV is a conserved quantity, it effectively describes the vortex stretching previously shown in Equation 2.2, without the need to account for baroclinicity. Fig. 2.7, taken from Hoskins (1997), shows the change in vorticity as an air parcel moves from a weakly stratified region, **A**, to a strongly stratified region, **B**. This air column shrinks as the two isentropes move closer together, and as a result, the vorticity perpendicular to the isentropes decreases. The opposite is true for diverging isentropes. Furthermore, if the isentropes remain equidistant but tilt in a different direction, the magnitude of the vorticity vector stays the same, but it tilts with the isentropes.

Lastly, if tropical air were transported poleward, as discussed in Section 2.1.2, this would result in a change in the Coriolis parameter. Since changes to the vertical profile are assumed to be small compared to changes in the Coriolis parameter, the relative vorticity of the air mass must adjust to conserve PV, compensating for the change in the Coriolis parameter and leading to anomalous anticyclonic rotation. The opposite is true for air moving equatorward. Thus, the direction and speed at which Rossby waves move can also be explained using Ertel's PV.

2.4.1 Symmetric Instability

One important feature of PV is that it indicates air masses that are symmetrically unstable, meaning small perturbations away from an equilibrium state will result in exponential growth away from that equilibrium. This is particularly significant in the mid-latitudes as it describes the convective processes along cyclone fronts, as illustrated in Fig. 2.8. In this figure, upward motion at 500 hPa is shown by the red stippled contours in the top panels, coinciding with negative PV, as theorised by Hoskins (1974), in the cross-section seen in the bottom panels, taken along the dashed white line. When considering a basic flow, $V(x, z)$, Hoskins (1974) demonstrated that for PV to be negative, either $\frac{\partial \theta}{\partial z} < 0$, indicating pure gravitational instability, or the vorticity perpendicular to isentropes $\zeta_\theta < 0$, indicating pure inertial instability. The strength of this negative PV also determines the rate of instability growth. Importantly, as PV is adiabatically conserved, these instabilities can only arise due to friction or heating.

Bennetts & Hoskins (1979) expanded this idea to a moist atmosphere. They defined wet bulb PV using wet bulb potential temperature rather than potential temperature. The reason for this change is that wet bulb potential temperature is only changed by diabatic processes other than latent heat. Equivalently, and for simplicity, we shall use equivalent potential temperature,

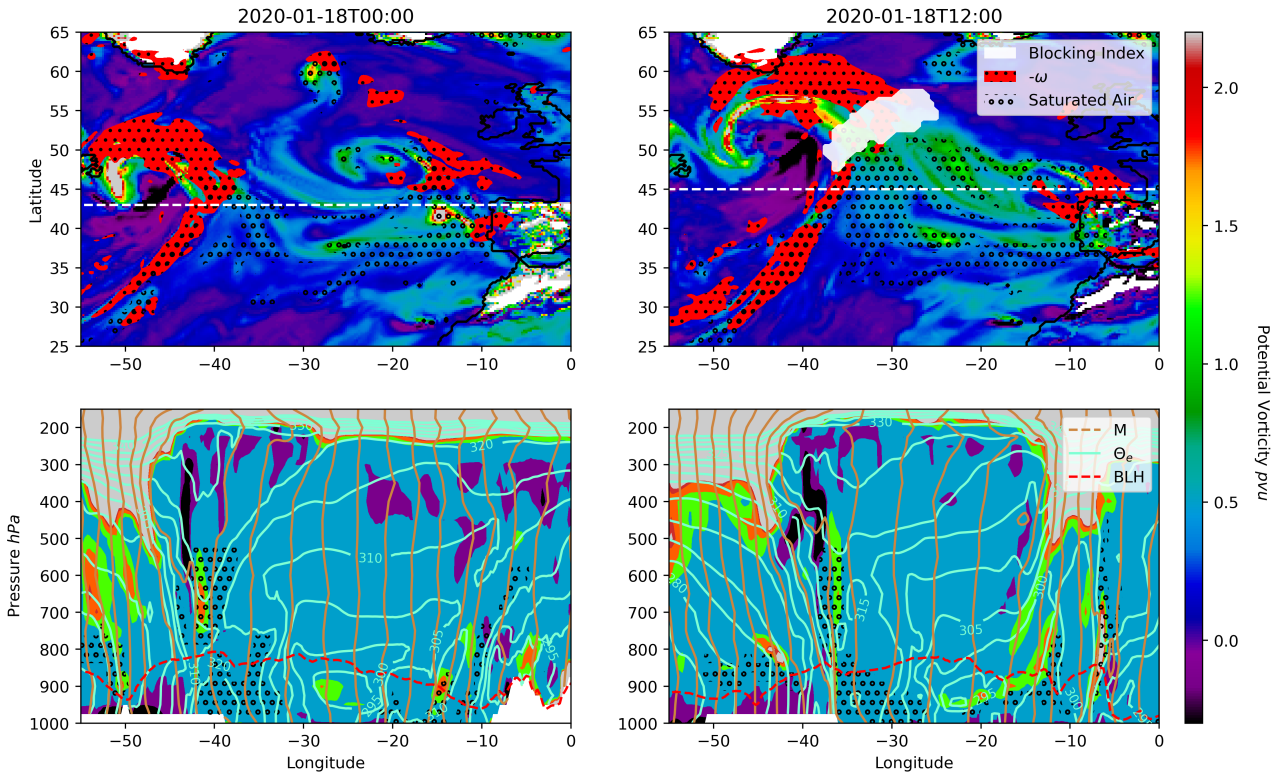


Figure 2.8: The average PV between 900-975 hPa (top) and a PV meridional section (bottom) (in PVU, 1 PVU = 10^{-6} Km^2 s^{-1} kg^{-1}) for a blocking event starting on January 18th, 2020. The white dashed line in the top panels indicates the position of the section used in the bottom panels. The red stippled contour shows upward velocities at 500 hPa where $\omega < -1$ Pa s^{-1}, while the hollow stippling shows air that has a relative humidity above 90% at 975 hPa. The brown, light blue, and red lines in the bottom panels show surfaces of constant momentum, moist potential temperature, and the height of the atmospheric boundary layer, respectively.

θ_e, to define moist PV, which has the same properties. Equivalent potential temperature is conserved for moist adiabatic transport and is defined as the temperature an air parcel would have if the parcel were brought adiabatically to some reference temperature and all of the water vapor inside the parcel condensed (Pauluis et al. 2010). When moist PV is negative, the air mass is said to be conditionally symmetrically unstable. This means that while the air mass might be thermally stable in the vertical direction and inertially stable in the horizontal direction, the air parcel will experience slantwise convection due to the isentropic surfaces being steeper than surfaces of absolute momentum (Emanuel 1983) as seen in the with the light blue and brown contours in the bottom panels of Fig. 2.8 indicating isentropes and surfaces of constant absolute momentum.

2.4.2 Diabatic Effects on Potential Vorticity

As PV is adiabatically conserved, it is possible to follow air masses along isentropic surfaces and see how they interact and affect the overall flow of the fluid of interest (Hoskins et al. 1985). However, as suggested above, the primary concern of this work is the diabatic influence due to air-sea interactions. As described in Section 7 of Hoskins et al. (1985), the change in PV in the presence of diabatic influence is:

$$\rho \frac{DQ}{Dt} = \boldsymbol{\zeta}.\nabla\dot{\theta} + \nabla \times \boldsymbol{F} \cdot \nabla\theta, \tag{2.6}$$

where $\dot{\theta}$ is the Lagrangian rate of change of the potential temperature due to heating effects, and $\boldsymbol{F}$ represents the frictional forces. Since the effects of friction act against the direction of flow, meaning that $\nabla \times \boldsymbol{F}$ points in the opposite direction of the vorticity vector, the overall effect of friction is to dampen the PV.

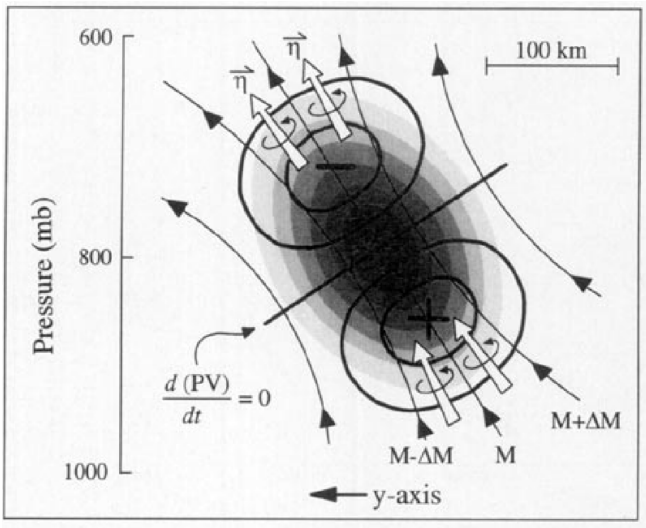


Figure 2.9: Fig. 9 from Stoelinga (1996), showing the effect of latent heating along a WCB. Absolute momentum surfaces and streamlines are shown with thin arrowed lines. Absolute vorticity vectors are shown with white arrows. Shading depicts the strength of latent heating and vertical transport. '+' and '-' symbols show the generation and destruction of PV, respectively.

As seen in Equation 2.6, the effects of heating act in a dipolar manner. Fig. 2.9 shows a schematic of heating along the WCB, with streamlines shown by the thin arrowed contours indicating vertical transport due to strong latent heating, which is shown in shading. The white arrows indicate the vorticity vectors showing the creation of PV at the inflow region and destruction at the outflow region. This led Methven (2015) to theorise that the overall net

transport of PV from inflow to outflow along the WCB is conserved, even though it is modified along the WCB due to latent heating.

Interestingly, this dipole behaviour breaks down at the air-sea interface, where the destruction of PV due to SSHF from the ocean to the atmosphere heats the atmospheric boundary layer and cools the oceanic mixed layer such that $\frac{\partial \dot{\theta}}{\partial z} < 0$ for both domains, as theorised by Marshall, Jamous & Nilsson (2001) and observed by Czaja & Hausmann (2009). This effect of air-sea heat fluxes on modifying PV was also observed by Vannière et al. (2016), who noted the generation of negative PV in the cold sector of a cyclone due to the destabilisation of the atmospheric boundary layer. This monopole signal is also present when PV is modified mechanically, as wind stress induces Ekman transport in both the atmospheric boundary layer and the oceanic mixed layer that acts to overturn isentropes.

Finally, the PV impermeability theorem from Haynes & McIntyre (1990) is a key result that further constrains the conservation of PV. This theorem states that in a volume enclosed by surfaces of constant entropy, the PV substance, ρQ, is constant, even in the presence of diabatic effects within the volume. As suggested by Fig. 2.9, the creation and destruction of PV are in equal parts, so any heating inside these isentropes does not change the total amount of PV substance. This is a powerful result, as it implies that the only way to change the overall PV inside a volume is when these isentropes intersect a surface, as is often the case for air-sea interactions.

2.5 Dynamical Systems Theory

Dynamical systems theory is a field in mathematics focused on the behaviour of systems that evolve according to specific equations of motion. As explained by Strogatz (2018), these equations can be either iterative maps for discrete systems, such as the logistic map first used in Lorenz (1964), or differential equations, like those used to integrate forecasting systems for weather prediction. These differential equations are written in the form:

$$\dot{\boldsymbol{x}} = \boldsymbol{f}(\boldsymbol{x}), \tag{2.7}$$

where $\boldsymbol{x}$ is the state vector of the system, and $\boldsymbol{f}$ is the function that transforms the state

vector into its velocity vector, $\dot{\boldsymbol{x}}$. The range of possible dynamics depends on the specific set of differential equations, though they are limited to certain categories of motion depending on the number of degrees of freedom, n, as described in Fig. 1.3.1 from Strogatz (2018), shown here as Fig. 2.10. For simple one-dimensional systems, only growth, decay, or equilibrium is possible. Moving to two dimensions, oscillation becomes possible, and finally, in three or more dimensions, chaotic motion can occur, though this requires non-linearity in the system, which will be discussed in Section 2.5.1.

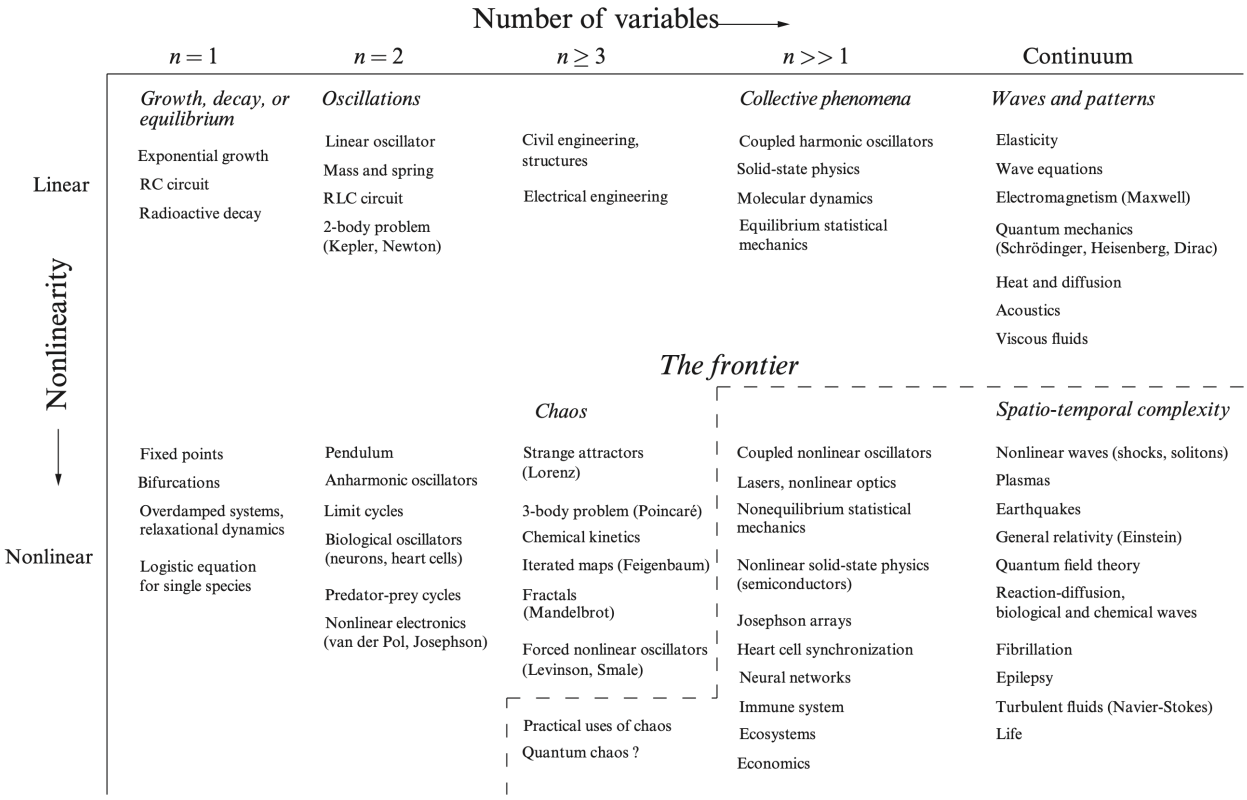


Figure 2.10: Fig. 1.3.1 from Strogatz (2018) describes the types of behaviours possible for dynamical systems of different dimensions and increasing non-linearity.

A primary concern for dynamical systems theorists are fixed points, which represent the equilibrium of the system. A fixed point of a system is one in which $\boldsymbol{x}(t+1) = \boldsymbol{x}(t) = \boldsymbol{x}^*$ for all t. To determine the flow around a fixed point, the system must first be linearized to approximate its stability and behaviour. This is done by perturbing the equilibrium state by an infinitesimal amount. The resulting equation of motion, with higher-order terms ignored, determines the linear behaviour of the system near that fixed point. This process produces the Jacobian matrix:

$$\boldsymbol{J} = \frac{\partial \boldsymbol{f}}{\partial \boldsymbol{x}}, \tag{2.8}$$

which describes the linear behaviour of the equations at a given point. This Jacobian matrix is then evaluated at the fixed point of interest $\boldsymbol{x}^*$, and its eigenvalues (or local Lyapunov exponents), λ, and eigenvectors determine the nature and direction of stability near that fixed point. If the real component of the eigenvalue is positive, that fixed point is said to be unstable, and the perturbed trajectory will grow exponentially away from the fixed point; the opposite is true for negative eigenvalues. A fixed point is said to be globally stable if it is approached from all initial conditions. In simple cases, this can be proven by inspection, but in complex cases, one must show that a Lyapunov function (a smooth positive-definite function) is strictly decreasing for all state vectors.

If the eigenvalues have an imaginary component, the trajectories will oscillate around the fixed point, forming either an unstable or stable spiral depending on whether the real part of the eigenvalues is positive or negative. However, if $Re(\lambda) = 0$ for any eigenvalue, it appears as if there is neither growth nor decay, making a stable limit cycle possible. This type of fixed point is called a center, or the center manifold of the dynamical system. These cases are delicate and require further analysis to determine the stability around the fixed point and whether a limit cycle actually exists.

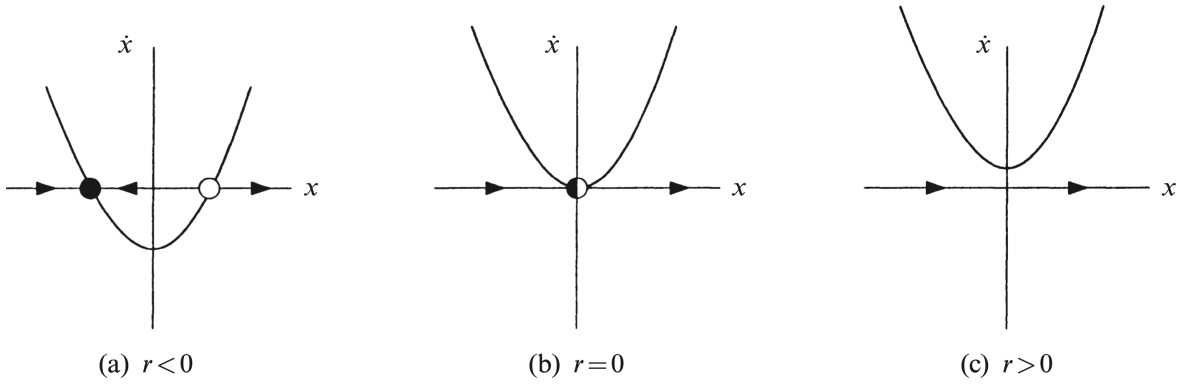


Figure 2.11: Saddle node bifurcation for the equation $\dot{x} = r + x^2$ where r is the control parameter, taken from Strogatz (2018), Fig. 3.1.1. Filled and hollow dots denote stable and unstable fixed points, respectively, while half-filled dots denote half-stable fixed points.

Bifurcation theory extends this analysis by examining how the number of fixed points and their stability change as the system's parameters are varied. For example, Fig. 2.11 shows

the annihilation of a stable and unstable fixed point as control parameter r is increased. For this system, a bifurcation occurs at $r = 0$, specifically a saddle node bifurcation. Many other types of bifurcations exist, such as transcritical bifurcations, in which a fixed point exchanges stability with another, or a Hopf bifurcation, in which a stable fixed point becomes unstable, and a limit cycle appears. In one dimension, only the creation, destruction, or destabilization of a fixed point is possible, but in two or more dimensions, oscillations can also be turned on and off. For more interesting behaviour we must move to three dimensions.

2.5.1 Chaos Theory

Chaos theory is a branch of dynamical systems theory that deals with complex irregular behaviours that arise from seemingly simple rules. First discovered by Lorenz (1963) in his seminal paper *Deterministic Non-Periodic Flow*, this classification is characterized by an important property: sensitivity to initial conditions. When a system has this property, nearby trajectories that start close to one another tend to diverge as they traverse across an attractor. Hence, any error in measuring the initial conditions of the system tends to grow exponentially at the rate of the largest Lyapunov exponent (Kuptsov & Parlitz 2012). Therefore, a requirement of sensitivity to initial conditions is a positive Lyapunov exponent. To explain this, we shall examine the model Lorenz studied.

Fig. 2.12 shows the Lorenz (1963) model in phase space, with the colouring showing the local dimension of the attractor. This quantity measures how many degrees of freedom there are at different regions along the attractor, or more simply, how many directions the trajectory can go. For non-chaotic systems, this is always equal to 1 along the trajectory. However, in chaotic systems, this can be any number from one to the dimension of the phase space, n. For example, a local dimension of two indicates that the system diverges along a planar direction in that region. Hence, this number is a measure of unpredictability along the attractor, as higher local dimensions indicate more directions in which a trajectory can diverge. The distribution of the local dimension across the whole attractor is related to the largest Lyapunov exponent (Young 1982), and therefore unpredictability for the system as a whole.

For the Lorenz (1963) system shown in Fig. 2.12, we can see one main region where the local dimension is rather high, shown in dark blue; the intercept of the two circular lobes in the middle of the attractor. As the trajectory moves along the left and right lobe of the attractor

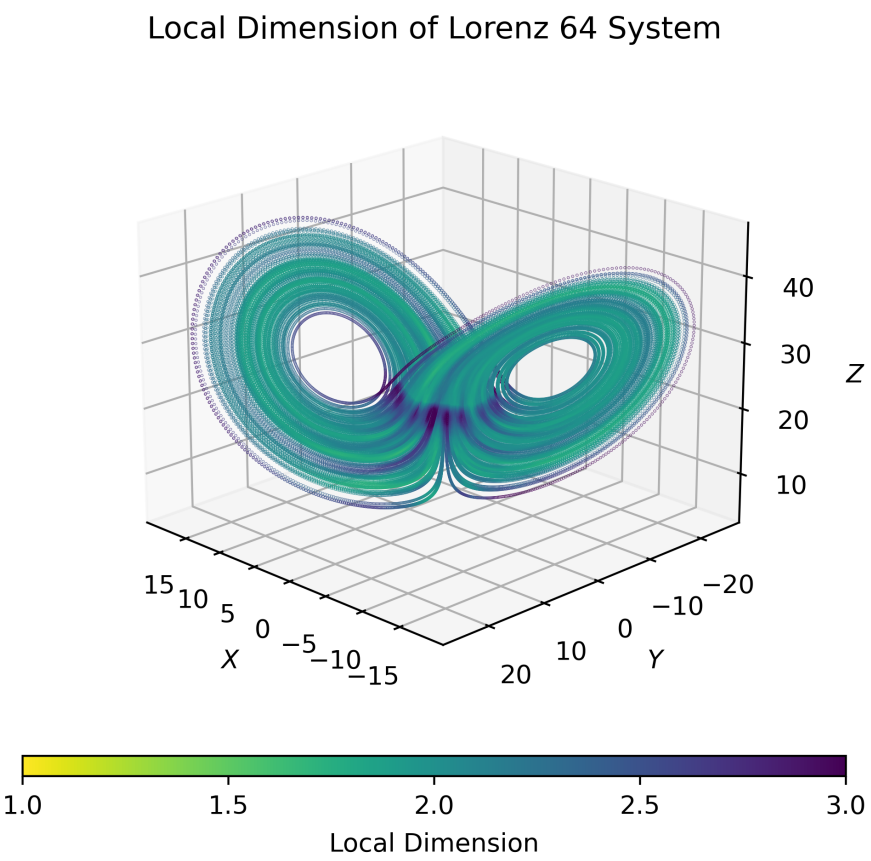


Figure 2.12: The Lorenz (1963) attractor for parameters $\sigma = 10$, $\rho = 28$, and $\beta = 8/3$. The colour shading shows the local dimension of the attractor calculated following Faranda et al. (2017).

in a clockwise and counterclockwise direction respectively, this dark region indicates the exit of the trajectories as they move past the intercept of the lobes. At this point, one small nudge could send the trajectory to either the left or right lobe, and equally to the outer or inner part of those orbits. Hence, any error in this region is likely to grow far quicker than in other regions along the attractor.

While this unpredictability inherent in chaos is commonly misunderstood as randomness, it is, in fact, entirely deterministic. Hence, if the equations of motion of the system are known, integrating the system forward from some given initial condition will give the same result if we repeat this integration from the same initial point at a later time. However, if that initial position is perturbed by a small amount that resembles measurement errors in the system, δ_0, the trajectories will appear to move together for a time until eventually they diverge, and no longer can we correctly correlate the movement of one trajectory with another. That time window, $t_{Horizon}$, where there is some predictability in the system is called the *time horizon*

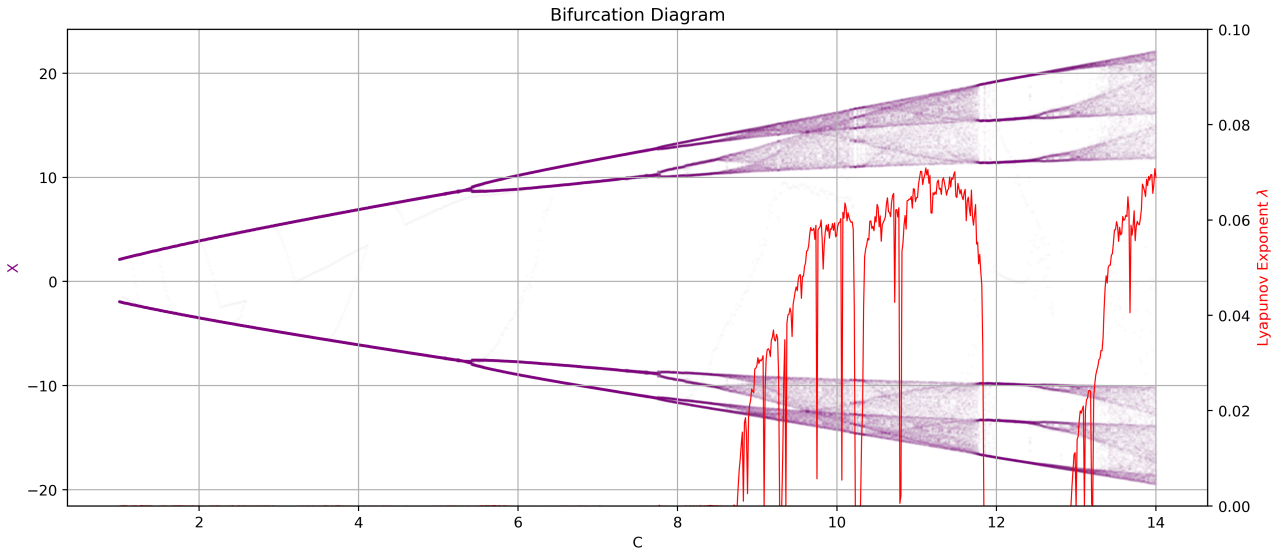


Figure 2.13: Bifurcation diagram for the Rossler (1976) system for variable x, with bifurcation parameter c. Parameters $a = b = 0.1$. The largest Lyapunov exponent is shown in red.

and is defined as such:

$$t_{Horizon} \sim O\left(\frac{1}{\lambda} \ln \frac{a}{\delta_0}\right), \tag{2.9}$$

where λ is the largest Lyapunov exponent, and a is some acceptable distance the trajectories diverge before we consider predictability to be lost. Therefore, generally, if one desires to double the horizon time of a system, the resolution in which the system is measured must be squared. This has major implications for weather prediction, as timely and reliable forecasts are limited by computational constraints.

As with non-chaotic systems, bifurcations can occur as control parameters in the model are adjusted. Fig. 2.13 shows the local extrema of the Rossler (1976) system as control parameter c is adjusted. For small values of c, there is a stable limit cycle, as shown by the two solid lines indicating the maximum and minimum of the trajectory relative to variable x. As this parameter is increased, there are a series of period-doubling bifurcations before eventually a chaotic regime is achieved, as shown by the largest Lyapunov exponent illustrated by the red curve. Eventually, the system reaches a window of predictability in which a 3-periodic orbit exists. This is followed by another series of period-doubling bifurcations and another chaotic regime. As this parameter is increased, the balance between the negative and positive feedbacks in the system is adjusted until eventually the system is no longer damped into a stable attractor

but exists in a strange attractor.

Suppose one were to design a system that is chaotic, what are the ingredients needed? Firstly, the system must be bounded, as cases that are sensitive to initial conditions but unbounded, such as infinite exponential growth, are not chaotic and rather trivial. Hence, the rate of change of volume of the system is always decreasing, or equivalently, $\dot{\boldsymbol{f}} < 0$ for all points in the basin of attraction. Therefore, the system needs some kind of damping or negative feedback. Additionally, as discussed above, there are regions along the attractor where there is exponential growth between trajectories, which implies the presence of positive feedback. However, if these feedbacks happen along directions that are independent of each other, there is no opportunity for these two processes to affect one another, and hence no interplay between the positive and negative feedbacks in the system. This points to the next requirement: coupling between variables.

As indicated by the map in Fig. 2.10, chaotic behaviour can only exist in three dimensions or more, another requirement when designing chaotic systems. This is a byproduct of the Poincaré-Bendixson theorem, which states that if a trajectory is bounded in a region that does not contain any fixed points, that trajectory must eventually approach a closed orbit. However, this theorem only applies in two dimensions and breaks down at higher dimensions. This means that it is now possible for a trajectory to wander around indefinitely in a closed bounded region, densely filling space.

Additionally, the map in Fig. 2.10 states that the chaotic system also requires some non-linearity. Importantly, linear functions are monotonic, i.e., they are either always increasing or decreasing in their domain, while non-linearity can have the same output for multiple inputs. This implies the ability to "fold" the state back on itself, as seen in the strange attractor in Fig. 2.12. This means that the system can contain some "stretching" through positive feedbacks, allowing for sensitivity to initial conditions, and "folding" through its non-linearity, allowing for a bounded system.

For an analogy, let's imagine a conversation between two people. Initially, these people aren't listening to one another; they sit side by side talking to themselves. Their conversations are independent and might lead to an inevitable end, spiral out of control, or go around in a loop, the behaviour of two lower dimensional independent systems. Now, let's interrupt their private conversations and have them talk to each other, but they are only allowed to say two

words, “Marco” and “Polo.” While one says “Marco,” the other replies “Polo,” and on and on indefinitely. This is a simple coupled linear system, as the conversation is entirely predictable given the initial point. Finally, let’s allow them the use of their full vocabulary, but now impose the condition that one must start the conversation with the question, “How are you?” This question can be asked in any number of different ways, with inflection on any of the three words likely to elicit an entirely different response. Alternatively, the pace and tone of the question would equally affect the response. But importantly, this is a similar initial condition no matter the delivery. As one can imagine, these conversations starting with the identical three words but different inflections would massively diverging given enough iterations. This would be an example of a coupled, non-linear system exhibiting a clear sensitivity to initial conditions. This is the kind of interaction that will be explored in the coming chapters, specifically the conversation between the Gulf Stream and the North Atlantic jet stream.

Chapter 3

Observational Evidence for Oceanic Maintenance of Atmospheric Blocking

This chapter is based on the paper "Oceanic Maintenance of Atmospheric Blocking in Wintertime in the North Atlantic" (Mathews & Czaja 2024), submitted to Climate Dynamics in January 2024. I performed all the analyses presented in this chapter, excluding the calculation of the atmospheric blocking metric, which was generously provided by Dr. Lukas Papritz.

Key findings: Oceanic preconditioning through anomalous heat transport via the Gulf Stream in late summer results in increased Greenland blocking in DJF.

3.1 Introduction

As described by Woollings et al. (2018), atmospheric blocking refers to a persistent, quasi-stationary weather system in mid to high latitudes that disrupts the usual westerly flow. These blocks can be responsible for localised extreme high temperatures in the summer and non-local extreme cold temperatures in the winter, as demonstrated, for example, by Pfahl & Wernli (2012). Attempts to project oceanic influence on such large-scale atmospheric dynamics date back to Bjerknes (1964). He conjectured that the atmosphere drives the majority of short-term inter-annual sea surface temperature (SST) variability, while the ocean is responsible for longer-term variability. More recently, Häkkinen et al. (2011) demonstrated that decades marked by a heightened frequency of atmospheric blocks align with warmer subpolar oceans and weaker ocean gyres as a result of wind-driven forcing. This aligns with reduced heat removal within the subpolar gyre, subsequently contributing to warmer waters, as well as

an increased turbulent heat flux (THF) from the Gulf Stream extension to the atmosphere. These observations collectively indicate the influence of atmospheric forcing on the ocean. In terms of the atmospheric response to changes in SSTs, O'Reilly & Czaja (2015) for the North Pacific, and O'Reilly et al. (2016) for the North Atlantic, showed that the state of SST fronts affects the frequency of atmospheric blocks on annual and sub-seasonal timescales, respectively. Furthermore, Famooss Paolini et al. (2022) suggested that the effects of the SST front on these blocks can only be observed with increased model resolution.

In order to accurately establish a connection between oceanic conditions and atmospheric blocks, it is crucial to utilise comparable parameters. Potential vorticity (PV) is a scalar quantity conserved by the flow in the absence of heating or friction. As defined by Schwierz et al. (2004), an atmospheric block is a negative PV anomaly in the upper troposphere that surpasses a certain amplitude, size, overlap, and stationarity threshold. Therefore, a direct comparison can be drawn between the generation of PV anomalies through diabatic air-sea interactions and atmospheric blocking indices. Furthermore, the PV impermeability theorem from Haynes & McIntyre (1990) asserts that PV substance remains constant across isentropic surfaces unless it encounters a boundary, such as the air-sea interface. In this context, PV can be introduced into the system, thereby influencing the fluid dynamics. By analyzing diabatic processes within the atmospheric boundary layer, Vannière et al. (2016) demonstrated that negative PV air masses are produced in the cold sector of a cyclone, primarily through large heat fluxes from the ocean to the atmosphere. These heat fluxes diminish the static stability within the boundary layer to such a magnitude and consistency that convection cannot sufficiently act to stabilize the temperature profile. Consequently, this results in a persistent negative PV signature at low levels of the troposphere. This finding is reinforced by Attinger et al. (2019), who extensively elucidated the role of individual diabatic processes in extratropical cyclones.

The heat flux from the ocean to the atmosphere does not only affect the PV of the atmosphere, but also the heat content of the ocean. Cayan (1992) noted that these heat fluxes exhibit a negative correlation with the rate of SSTs. While SST anomalies are primarily driven by stochastic atmospheric forcing as shown by Frankignoul & Hasselmann (1977), they are also altered by oceanic temperature advection, entrainment of the oceanic mixed layer and mixing (e.g. Frankignoul 1985 and more recently Bishop et al. 2017). The strength of these air-sea interactions is primarily due to the difference in air-sea temperatures and hence any buildup

of oceanic heat has an effect on the strength of these fluxes, as observed for example by Kelly et al. (2010). The depth of the mixed layer in the ocean also determines how much thermal inertia these SST anomalies have. The deep mixed layer in the winter (Kraus & Turner 1967) slows down temperature change due to air-sea interactions (Cayan 1992) and acts as a heat reservoir for the atmosphere.

The importance of diabatic processes for atmospheric blocks is beginning to be understood. Pfahl et al. (2015) showed that 30-45% of the air mass involved in atmospheric blocks has undergone at least 2K of latent heating. Additionally, as shown by Yamamoto et al. (2021), these blocks source 28%-55% of their moisture for diabatic heating from the ocean, indicating that 11%-23% of blocking particles originate from oceanic pathways. This is corroborated by the case study from Wenta et al. (2024), showing that 43% of moist particles originate between the surface and 800hPa, 28% of which interact with the Gulf Stream. Moreover, 88% of the along-trajectory potential temperature variability of these particles is explained by their accumulated THF (Yamamoto et al. 2015). A portion of this heating occurs along the fast warm ascending air stream in the cyclone known as the warm conveyor belt (WCB). After the particle's ascent, the diabatically modified air mass is deposited in the upper troposphere on the western flank of the block, advecting negative PV anomalies against the eastward background flow (Steinfeld & Pfahl 2019). A previous study by Steinfeld et al. (2020) showed that restraining the latent heating along the WCB resulted in some blocks experiencing a reduction of size, amplitude and duration, while others did not develop at all. Clearly the next step in understanding this diabatic contribution to atmospheric blocking is to extend our gaze to the ocean, as both a source of negative PV air masses, and thus a source of negative PV anomalies, via surface sensible heat flux (SSHF), and a source of moisture for WCB ascent via surface latent heat flux (SLHF).

In this study we bring the discussion further. We demonstrate, employing the novel perspective provided by a moist PV framework, that the diabatic influence on wintertime North Atlantic blocks is not only a result of stronger air-sea interactions over the Gulf Stream and its extension, but also that oceanic preconditioning through heat advection and heat content anomalies affects both the block's size and frequency in the North Atlantic basin. This paper is structured as follows. In section 3.2 we describe the data and methods. Analysis is done in section 3.3. Details of the method and orders of magnitude are discussed in 3.4, followed by our conclusions

in section 3.5.

3.2 Method

The results presented in this paper are derived from ERA5 data spanning from 1979 to 2020 (ERA5, Hersbach et al. (2020)). The Florida Straits heat transport data from the RAPID array is utilised for the period between 2004 and 2018, as calculated by McCarthy et al. (2015), rather than the total ocean heat transport at 26N. Additionally, the top 300 meters of heat content data is obtained from Argo measurements covering the same period from 2004 to 2018 (Argo (2023)).

The blocking mask was computed using the method described by Schwierz et al. (2004) with ERA5 data. To process the data for this algorithm, the PV field was averaged within the 150hPa to 500hPa range. Then, a 31-day running mean climatology was subtracted to isolate PV anomalies in the upper troposphere. Anomalies less than -1.3PVU, exhibiting at least a 70% spatial overlap between timesteps, and persisting for a minimum of 5 days were identified as blocks.

Moist PV was calculated by substituting equivalent potential temperature for potential temperature in Ertel's PV equation (Gill 1982), as shown below:

$$Q_e = \frac{\vec{\zeta} \cdot \vec{\nabla}\theta_e}{\rho}, \tag{3.1}$$

where Q_e is the moist PV, ζ is the vorticity vector, ρ is the density and θ_e is the equivalent potential temperature. The calculation of equivalent potential temperature follows the method outlined by Bolton (1980).

For composite analysis, we utilised the moving block bootstrap technique as introduced by Wilks (1997) to preserve both temporal and spatial correlations within the fields. We employed five hundred bootstrap samples. The size of the resample block was based on the length of time required for the observed field to decorrelate. For example, when calculating a blocking frequency composite, the blocking field was resampled in blocks of 12 days. This duration was chosen as it was approximately the time needed for any random point in the blocking field to become decorrelated with itself. Subsequently, the composite calculation was performed on

each bootstrap sample, resulting in a distribution of randomly generated composites. From this distribution, the false discovery rate could be extracted, providing the 95% confidence interval (Wilks 2016).

Significance values for cross-correlation analysis are determined as follows. Two time series, each the same length as the observed time series, were generated using a first-order autoregressive model with the same autocorrelation characteristics as the observed time series. Then a cross-correlation was performed between these two synthetic time series. This process was repeated 500 times, generating a distribution of the cross-correlation coefficients. The significance interval was then determined from this distribution.

NAME	DATA SET	UNITS	FREQUENCY	LOCATION	DESCRIPTION
Heat Flux	ERA5	Wm^{-2}	6 hourly	Air-sea interface	Mean THF within the $350Wm^{-2}$ DJF climatology (orange contour Fig. 3.3).
PV	ERA5	PVU	6 hourly	950hPa	Mean PV within the $350Wm^{-2}$ DJF climatology (orange contour Fig. 3.3).
Block On	ERA5	Binary	6 hourly	150-500hPa	Block presence within the 7.5% DJF climatology (green contour, Fig. 3.3)
Block Area	ERA5	m^2	6 hourly	150-500hPa	Total block area within the 7.5% DJF climatology (green contour, Fig. 3.3)
Heat Content	ARGO	J	Monthly	Top 300m of ocean	Total ocean heat content within the $350Wm^{-2}$ DJF climatology (orange contour Fig. 3.3).
Heat Transport	RAPID	W	12 hourly	Oceanic profile at $26N$	Heat transport through the Straits of Florida

Table 3.1: The collection of time series used in this analysis, with a description of which data set they belong to, their units, frequency, location and how they were calculated.

The time series employed in this study, as detailed in Table 3.1, were deseasonalised. This process involved calculating the average value for each specific time step within a year (e.g., January 1st, 0600hrs), applying a 30 day running average to that seasonal cycle and then subtracting it from the respective time series to eliminate seasonal variations. This was done to eliminate correlations arising from seasonal variability in these variables. Additionally, linear

detrending was applied to all time series to limit the the influence of long term signals such as multi-decadal variability or anthropogenic forcing.

3.3 Results

3.3.1 Synoptic and Climatological Conditions

To motivate our analysis, we first describe the synoptic situation of a cyclonic event that occurred on January 18^{th} 2020. Fig. 3.1 shows the PV field (coloured field) for the preconditioning (top panel), induction (middle panel) and maintenance (bottom panel) processes of an atmospheric block over the North Atlantic. The left panels display a cross section of these events, with the position of the cross section indicated by the dotted white line in the corresponding right panels. The right panels illustrate the lower troposphere average (900hPa - 975hPa) of this field. Focusing on the right panels, the purple and black colors indicate regions of negative PV air mass, primarily located in the cold sector of the cyclones and its wake as it moves over the North Atlantic. Although this negative PV air-mass is unstable (Hoskins 1974), it pools in the wake of the cyclone, weakening with its distance from the cold sector. As the cyclone moves over the Gulf Stream, this negative PV region in the cold sector corresponds to areas of extreme THF as shown by the orange contour. The preference this heat flux has to warmer waters is clearly seen in Fig. 3.1, in which the THF contour roughly coincides with the Gulf Stream surface warm core. Note that negative PV is also present ahead of the cyclone and to the southeast of the cyclone's cold front. This negative PV signal was seen in the cold sector of a previous cyclone (not shown), which can now be observed decaying southwest of the Irish coast.

The middle panel in Fig. 3.1 depicts the induction of a block with the white contour indicating the blocking mask. This corresponds to the outflow of the WCB as illustrated by the red stippled contours which depict upward velocities at 500hPa where $\omega < -1\text{Pas}^{-1}$. Moreover, there is northward advection of upper tropospheric anticyclonic air contributing to the generation of this negative PV anomaly (not shown). This is a typical situation for many block's genesis over the North Atlantic, and is in agreement with Steinfeld & Pfahl (2019).

Focusing on the left panels, the presence of negative PV air masses is primarily within the atmospheric boundary layer, as denoted by the dashed red line, but also present in thin filaments

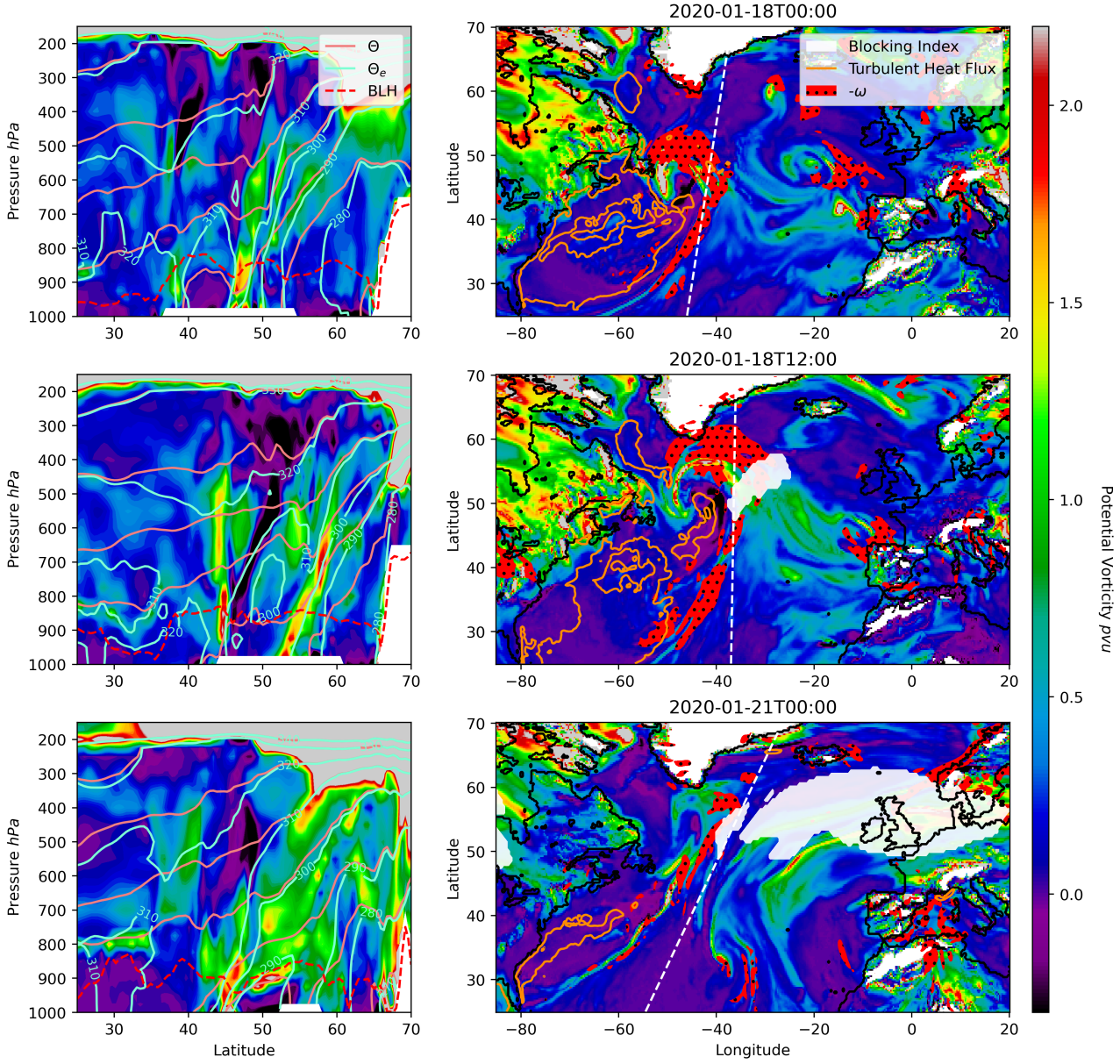


Figure 3.1: PV section (left) and PV averaged between 900-975 hPa (in PVU, 1 PVU = 10^{-6} Km^2 s^{-1} kg^{-1}) (right) for a blocking event starting on January 18th, 2020. In the left panels, the light red, light blue, and dashed red contours indicate the potential temperature, equivalent potential temperature, and boundary layer height respectively. In the right panels, the white contour indicates the blocking mask, the orange contours show the 500 Wm^{-2}, 1000 Wm^{-2}, and 1500 Wm^{-2} turbulent heat flux, and the red stippled contour shows upward velocities at 500 hPa where $\omega < -1$ Pa s^{-1}. The dashed white line indicates where the section is taken.

extending from the boundary layer to the upper troposphere. These filaments are co-located with the ω contours in the right panels, and hence are transported upwards at 500hPa. This observation suggests an injection of negative PV air masses from the boundary layer into the upper troposphere which contributes to the negative PV anomaly of this atmospheric block.

The bottom panel depicts a typical maintenance process in which a subsequent cyclone deposits

a diabatically modified air mass on the western flank of the block, thus advecting negative PV anomalies westward (Steinfeld & Pfahl 2019) and preventing this structurally unstable object from decaying (Holmberg et al. 2023). This is seen in the detached white contour which has just appeared at this time step and merges with the larger contour in the next time step (not shown).

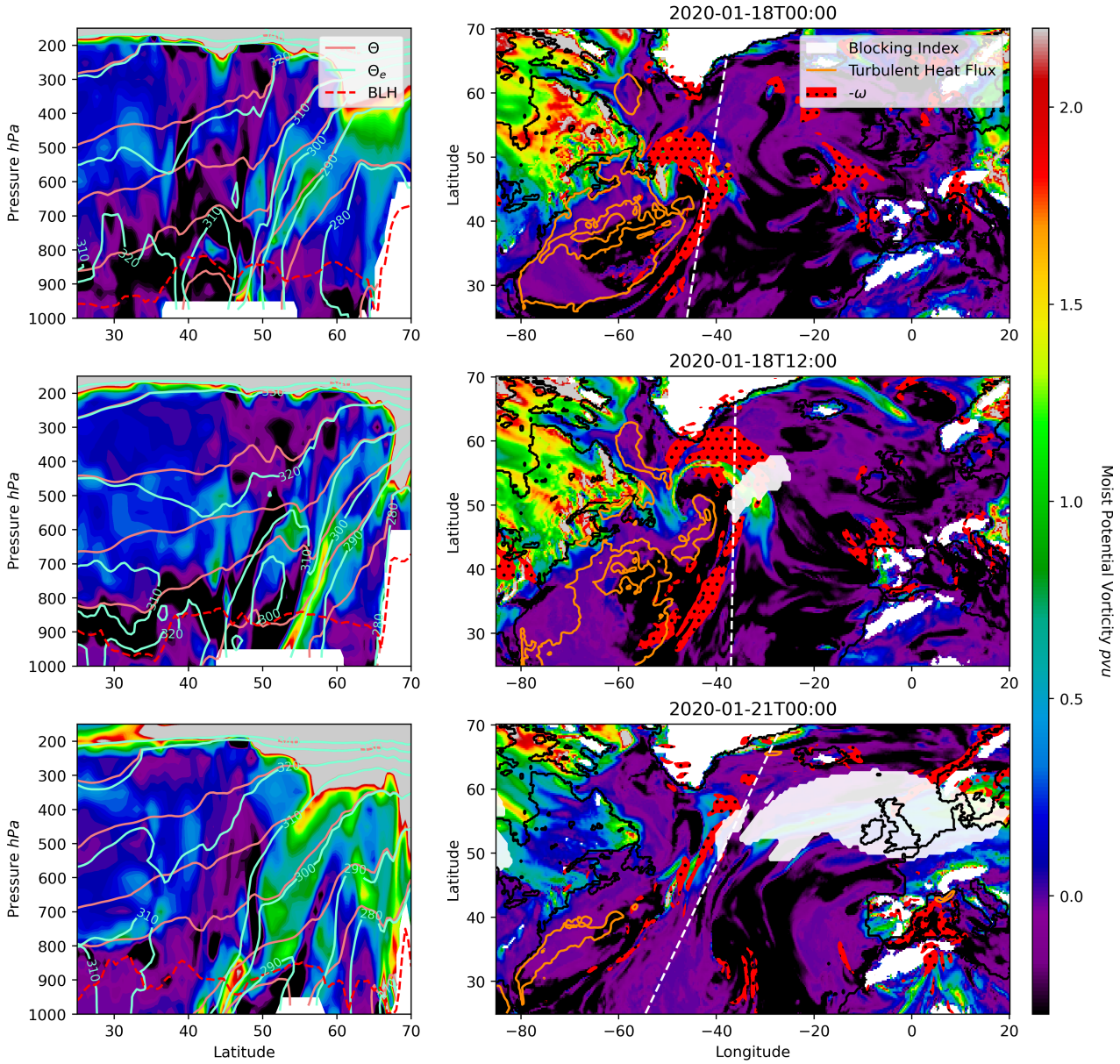


Figure 3.2: As in Fig. 3.1 but now showing moist PV.

Focusing on diabatic effects, we analyse this event from a moist PV framework, as shown in Fig. 3.2. As discussed in Bennetts & Hoskins (1979), moist PV can only be changed by diabatic effects other than latent heat release, and when the angle between the moist and dry isentropes in the horizontal plane is non-zero. For clarity, PV calculated using dry isentropes will now

be called "dry" PV. The right panels illustrate the ubiquitous presence of negative moist PV air masses over the North Atlantic, with the sole exception being along cyclonic fronts. Since moisture fluxes now influence equivalent potential temperature, and consequently moist PV, as demonstrated by Pauluis et al. (2010), we observe the additional impact of SLHF on the boundary layer moist PV. Therefore negative moist PV in the boundary layer has a larger magnitude when compared to "dry" PV, on the order of O(1PVU). Moreover, as indicated by the light blue contours representing equivalent potential temperature, this air mass undergoes minimal change in equivalent potential temperature during its ascent from the boundary layer to the upper troposphere along moist isentropes, as observed by Martínez-Alvarado et al. (2014). Therefore, moist PV experiences minimal change due to heating along the WCB. Conversely, when examining the light red contours indicating potential temperature, we find, from a dry perspective, that the air mass along these filaments must experience at least 20K of heating in order to ascend from the boundary layer to the upper troposphere, a value consistent with observations by Madonna et al. (2014) in WCBs. It is worth noting that both the dry and moist isentropes converge with increasing height due to the scarcity of moisture at these pressure levels, which accounts for the similarities observed between PV and moist PV in Fig. 3.1 and 3.2 in the upper troposphere.

We now turn to the climatology. Fig. 3.3 shows the DJF (December, January, February) mean of both the THF and the PV at 950hPa. Positive THF indicates heat flux from the ocean to the atmosphere. This figure shows an increased THF along the warm core of the Gulf Stream and its extension, with the presence of low PV air masses above. The latter's presence extends to the continental shelf, into the Labrador Sea and Irminger Basin. It notably aligns with the positive THF pattern observed over the North Atlantic and demonstrates a distinct sensitivity to the demarcation between the continental shelf and the deep ocean.

Fig. 3.4 presents the DJF mean of the negative PV frequency throughout the troposphere. In the lower troposphere (bottom panels), there is a pronounced spatial signature that corresponds to the THF signature observed in Fig. 3.3. This signature weakens with increasing height. In the middle troposphere (middle panels), this signal diminishes, although it still displays a stronger presence over the storm track, before increasing again at 300hPa. The spatial pattern observed at 300hPa closely resembles the WCB climatology for DJF as observed by Madonna et al. (2014), depicted in their Fig. 4.

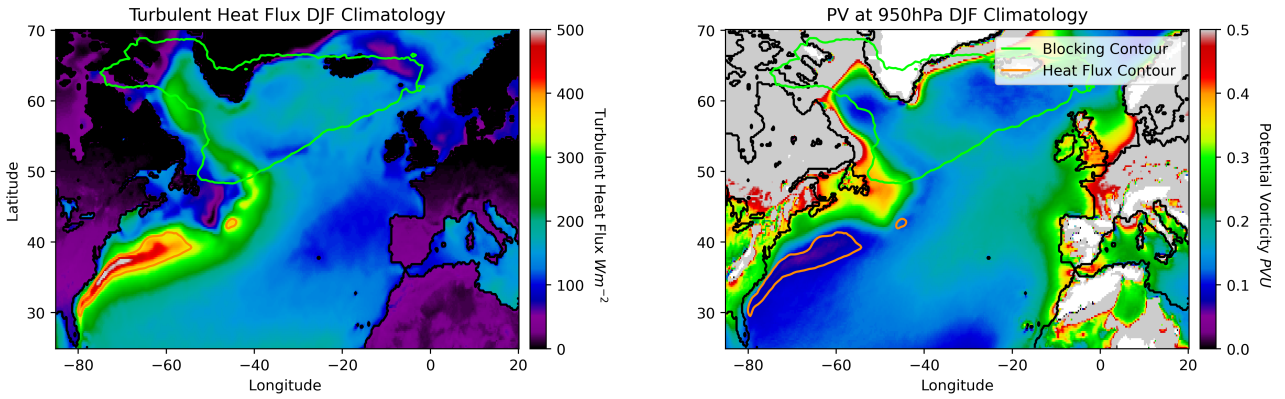


Figure 3.3: DJF climatology of the THF and PV at 950hPa over the North Atlantic. The green and orange contours represent the 7.5% blocking frequency and the 350Wm^{-2} THF climatology during DJF, respectively.

The white contours in Fig. 3.4 represent the frequency of negative moist PV. In contrast to the "dry" PV situation, negative moist PV is widespread in the lower troposphere and shows a gradual decrease towards the upper troposphere, where it aligns with the negative PV signal. It is worth noting that our moist PV diagnostic does not show this decrease in the middle troposphere, unlike that of "dry" PV. We interpret this results as reflecting the negligible effects of latent heating on moist isentropes (Pauluis et al. 2010) along the warm conveyor belt.

Cross correlation analysis between the heat flux and PV time series described in section 3.2 (refer to Table 3.1), confirms the influence of oceanic heat fluxes on boundary layer air (not shown). There is a minimum correlation of -0.54 between these two 6-hourly time series when the heat flux time series leads by 6 hours. This strengthens to a minimum of -0.74 when performing a one month running mean, having the strongest correlation with the heat flux time series leading by 42 hours. Expanding the moving average window leads to a reduced correlation between the two time series, highlighting that this phenomenon operates on timescales of approximately one month or less. This relationship is in agreement with Vannière et al. (2016) who shows that negative PV air masses are generated in the cold sector of cyclones through the reduction of static stability in the atmospheric boundary layer caused by strong upward air-sea heat fluxes.

We now examine the effects of blocking presence over the North Atlantic on these boundary layer processes over the Gulf Stream. Fig. 3.5 displays a composite of the surface pressure during instances of blocking within the 7.5% DJF blocking frequency climatology contour (green contour) compared to the absence of blocking in this same contour. This composite reveals a

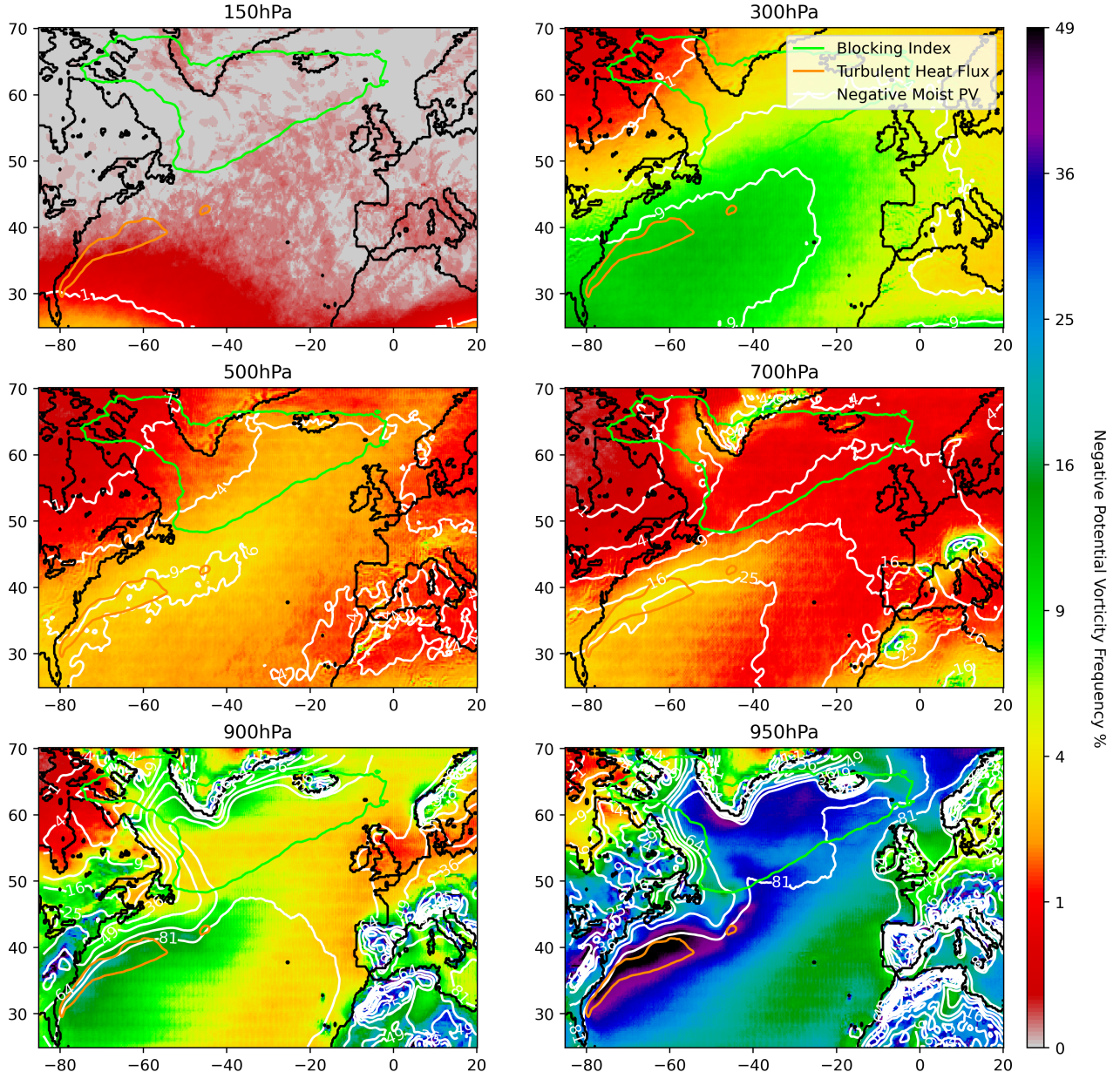


Figure 3.4: DJF climatology of the negative PV frequency. The white contours indicate the frequency of negative moist PV. The green and orange contours represent the 7.5% blocking frequency and the 350 Wm^{-2} THF climatology during DJF, respectively.

high-pressure anomaly centred south of Iceland and a low-pressure anomaly centred on the Azores, indicative of a negative North Atlantic Oscillation (NAO) signal. A negative NAO is associated with weaker westerlies and reduced circulation of warm, moist air from the equator, leading to an increased occurrence of cold air outbreaks across the Gulf Stream (Bjerknes 1964, Cayan 1992, Cellitti et al. 2006, Kolstad et al. 2009), as highlighted by the white arrows denoting anomalous 10m wind. Consequently, a significant increase in THF is observed over the Gulf Stream when blocking is present over the North Atlantic, which coincides with negative PV

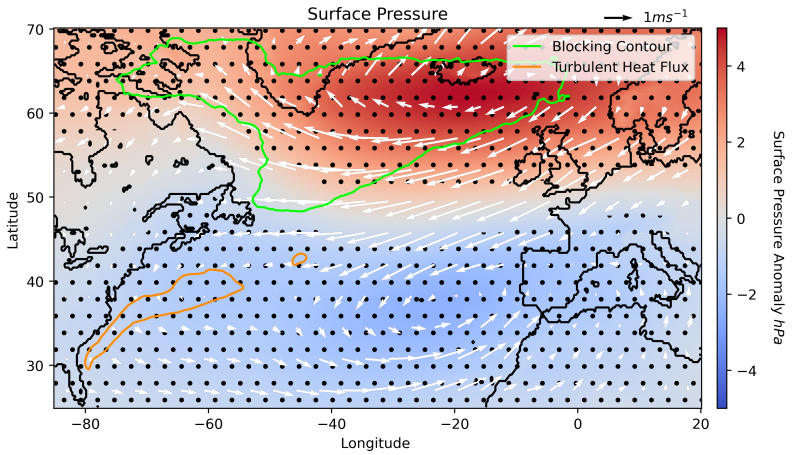


Figure 3.5: Surface pressure anomaly (in hPa, color) composite during periods when a block is present inside the green 7.5% DJF blocking frequency climatology contour minus blocking absence in this same contour . The white arrows indicate the 10m wind anomalies, with the black arrow showing the size of the 1m/s vector. The orange contour represents the 350 Wm^{-2} THF climatology during DJF. The stippling indicates 95% confidence.

anomalies in the atmospheric boundary layer over the same region (not shown). Next, we'll investigate how the ocean impacts atmospheric blocking in the North Atlantic and explore the related air-sea interactions, by extending our analysis to summertime months before the winter blocking season.

3.3.2 Oceanic Preconditioning

The top panel in Fig. 3.6 shows the cross-correlation between the seasonally averaged blocking area time series (refer to Table 3.1) in DJF and the Florida Straits heat transport time series, depicted in light blue, as well as the heat content time series, depicted in dark orange. The DJF blocking area exhibits a maximum correlation with heat transport five months prior (July, August, September), a signal far stronger than that of heat transport across the entire North Atlantic with blocking time series (not shown). Since both the heat transport and blocking area time series autocorrelations decorrelate far faster than five months (one month and 12 days respectively), this is suggestive of oceanic heat transport forcing the upper troposphere. Simultaneously, there is a notable maximum negative correlation with the heat transport, likely stemming from the wind stress associated with North Atlantic blocking, as observed in Fig. 3.5, although due to the lack of temporal division, causality is far more difficult to infer. Notably, the strength of this correlation can exceed 0.6, depending on the period during which atmospheric blocking is analysed. Examining now the relationship between the heat content and blocking

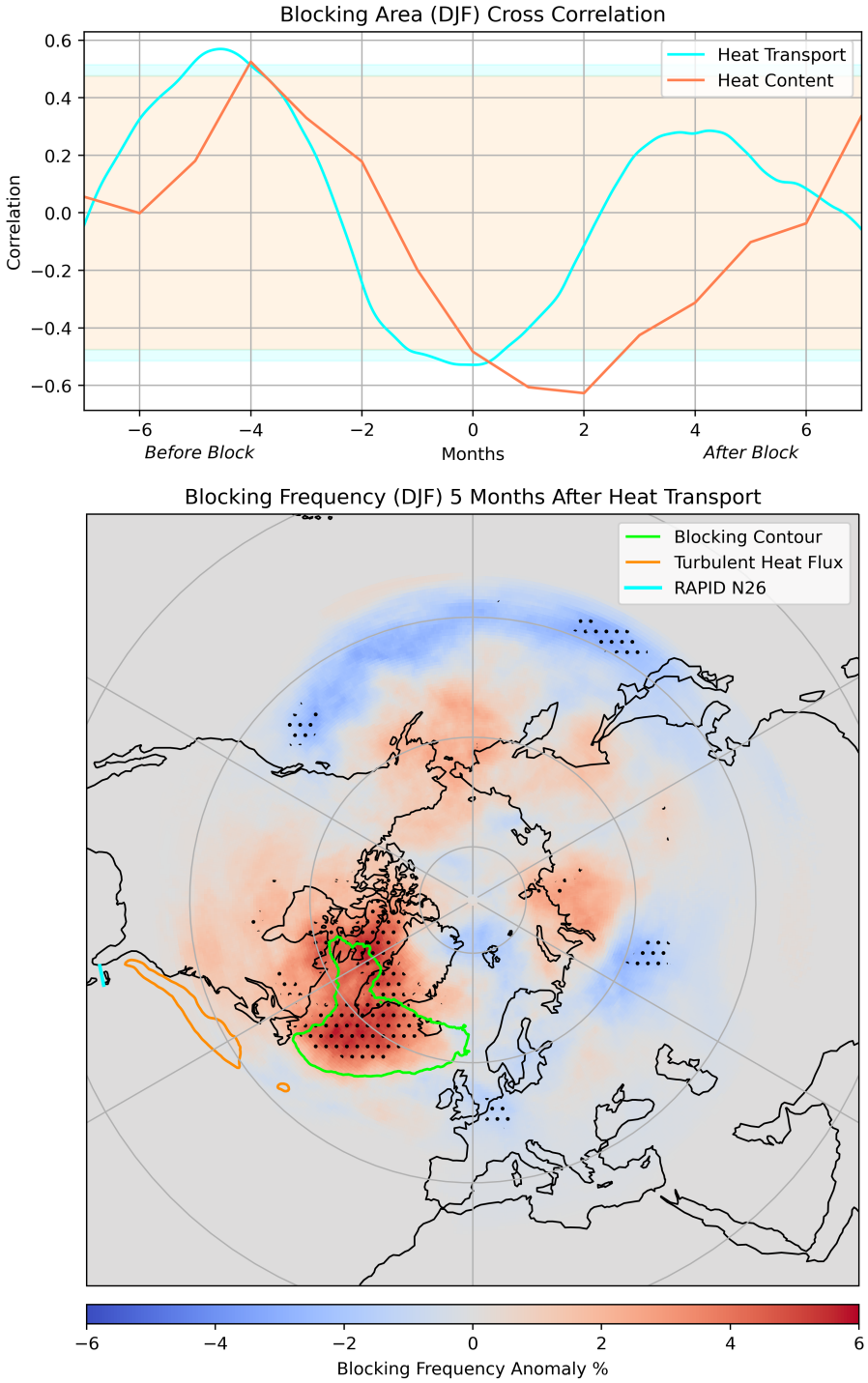


Figure 3.6: The top panel shows the cross correlation between the seasonally averaged blocking area time series (refer to Table 3.1) in DJF and the Florida Straits heat transport (light blue), and the heat content (dark orange) time series. The 95% confidence interval is shown with a coloured fill. The bottom panel shows the composite of the blocking frequency in DJF, 5 months after increased heat transport through the Florida Current. The green and orange contours represent the 7.5% blocking frequency and the 350Wm^{-2} THF climatology during DJF, respectively. The light blue line shows the RAPID N26 mooring. Dotted stippling indicates 95% confidence.

area time series, we observe a maximum positive correlation when the heat content leads by four months, and a maximum negative correlation when it lags by two months. The latter suggests that the block removes heat from the oceanic mixed layer, a relationship similar to that seen by Kelly et al. (2010) between oceanic heat content and THF. The former is consistent with a five month lead seen in the heat transport time series (light blue curve) and a one month time timescale to build this heat anomaly.

The bottom panel in Fig. 3.6 shows a blocking frequency composite in DJF, five months after increased heat transport through the Straits of Florida. Both the blocking field and heat transport time series are seasonally averaged. This figure demonstrates an increase in atmospheric blocking within the 7.5% DJF blocking frequency climatology (green contour) following increased heat transport in the preceding JAS, with an increase of up to 6%. Additionally, a reduction is observed at lower latitudes around the globe, accompanied by a non-significant positive signal northward of these areas suggestive of northward shift for atmospheric blocks.

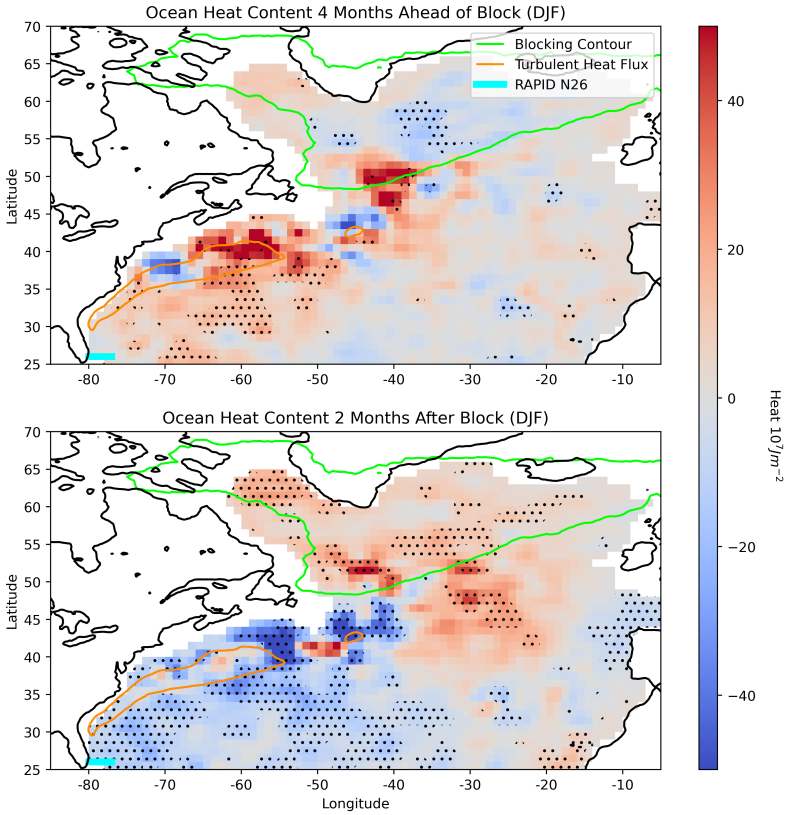


Figure 3.7: A composite of the top 300m Argo heat content 4 months before (top panel) and 2 months after (bottom panel) increased blocking area inside the green contour representing the 7.5% blocking frequency climatology during DJF. The orange contours represent the 350Wm^{-2} THF climatology during DJF. The light blue line shows the RAPID N26 mooring. Dotted stippling indicates 95% confidence.

To investigate further the heat content change in the ocean, the top panel in Fig. 3.7 presents a composite of the top 300m ARGO heat content in SON (September, October, November) before a period of increased area blocked inside the green contour. This period corresponds to the time of maximum correlation between ocean heat content and blocking area time series (refer to Table 3.1) in DJF, as depicted in the upper panel of Fig. 3.6 (dark orange curve). The composite reveals a statistically significant increase in heat content along the Gulf Stream and its extension. Notably, this signal exhibits a strong resemblance to the SST pattern observed by Rodwell & Folland (2002) with the similar lead time to NAO anomalies. Additionally, this spatial signal is seen when preforming a composite of oceanic heat content in SON using the heat transport time series in the subsequent JAS (not shown).

Conversely, the bottom panel in Fig. 3.7 displays the same composite of heat content, but in FMA (February, March, April). FMA aligns with the time of maximum negative correlation between ocean heat content and blocking area time series (refer to Table 3.1) in DJF, as shown in the upper panel of Fig. 3.6 (dark orange curve). This composite exhibits a statistically significant decrease in heat content along the Gulf Stream and its extension, along with a significant increase throughout the subpolar gyre. This signal bears resemblance to the well-known SST NAO tripole synonymous with atmospheric forcing (Cayan 1992, Visbeck et al. 2003).

3.3.3 Mechanism

The above results outline the series of events that connects atmospheric blocking to oceanic pathways, and details the coupling between them. This mechanism happens in tandem with dry and moist mechanisms outside of the boundary layer. These results are summarised here in Fig. 3.8 and are now linked with previously published research in order to describe the mechanism fully.

A number of months prior to a period of increased atmospheric blocking there is increased heat transport through the Florida Straits into the Gulf Stream region. This anomalous heat transport generates surplus heat in this region, which is then entrained into the mixed layer in autumn as described by Kraus & Turner (1967), resulting in a larger volume of the ocean becoming available for air-sea interactions (Kelly et al. 2010). This is illustrated in the schematic in Fig. 3.8 (label **A**).

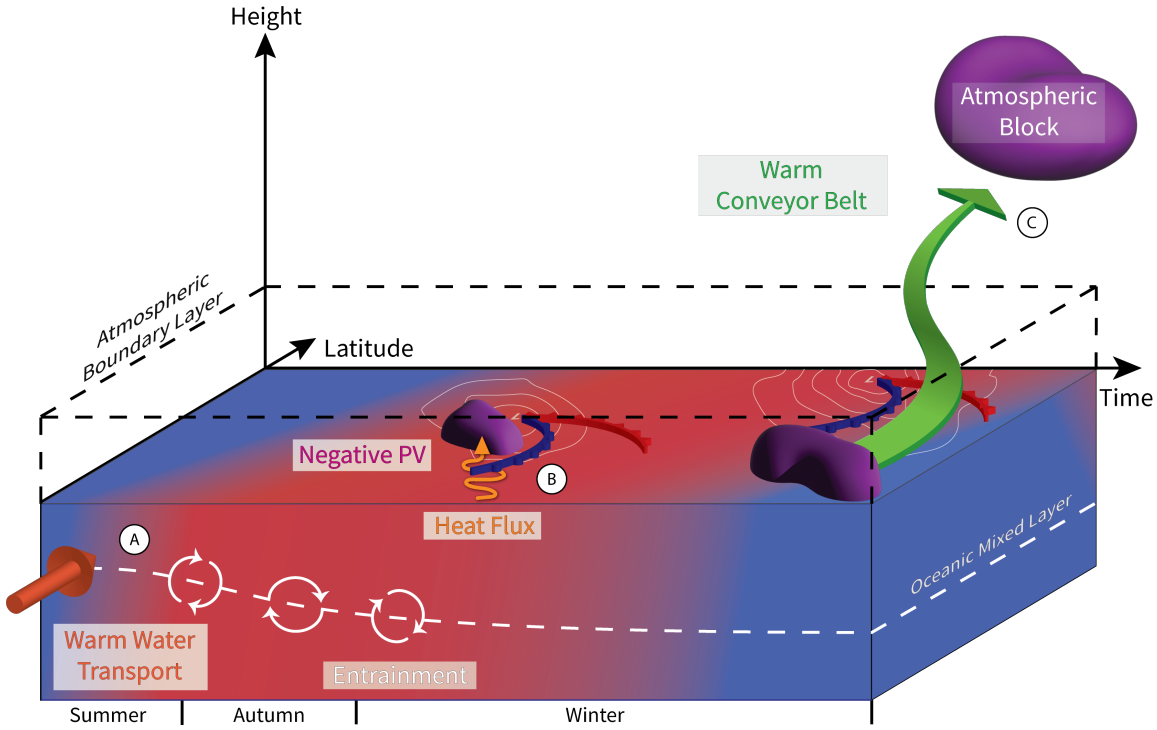


Figure 3.8: A schematic summarising the series of events that lead to oceanic maintenance of atmospheric blocking. The bottom slab represents the ocean, with blue and red colors representing anomalously cold and warm water respectively. The red, orange and green arrows show the warm water transport, heat flux from the ocean to the atmosphere and the WCB respectively. The purple blobs show anomalously low PV. Low pressure systems are illustrated with red and blue fronts and grey isobars. The markers A, B, and C are described in the main text.

The surplus heat in the oceanic mixed layer then allows for stronger THF events, as shown by Kelly (2004) and illustrated in Fig. 3.8 (label **B**). The positive THF seen in Fig. 3.1 primes the atmospheric boundary layer. Negative PV air masses are generated via the SSHF in the cold sector of the cyclone (Vannière et al. 2016, Attinger et al. 2019) and pool in the wake of this cyclone. Furthermore, these negative PV air masses becomes saturated with moisture due to the intense SLHF in the cold sector. It is important to note that while SLHF doesn't directly affect the PV of the air mass, it does impact the moist PV. As a result, a considerably greater amount of negative moist PV is generated within the boundary layer, as observed in Fig. 3.2.

Similar to the mechanism described by Papritz et al. (2021), which explains the handover of a moist air mass from one cyclone to another, the negative PV air masses that are pooled in the cold sector of a cyclone are subsequently transported in the WCB of a succeeding cyclone and injected into the upper troposphere, as shown by Wenta et al. (2024). This contributes to the development of a negative PV anomaly, potentially initiating an atmospheric block, as

observed in the middle panel of Fig. 3.1 and illustrated in Fig. 3.8 (label **C**).

The moisture from these air masses is utilised for latent heating along the WCB, allowing this air mass to ascend from the boundary layer to the upper troposphere across dry isentropic surfaces, as demonstrated by Madonna et al. (2014). This heating along the WCB increases the "dry" PV below the region of heating and decreases it above (Hoskins 1997). However, from a moist framework, these air masses experience minimal change in equivalent potential temperature as they travel along the WCB, as observed, for example, by Martínez-Alvarado et al. (2014). Therefore, as shown in Fig. 3.2, the inflow of moist PV is roughly equivalent to the outflow along the WCB. Due to the lack of moisture in the upper troposphere, moist PV is approximately equal to PV, as seen between Fig. 3.1 and 3.2 and in Fig. 3.4, and therefore the PV transported to the block is approximately equal to the moist PV in the boundary layer. In a moist framework, the SLHF serves to steepen moist isentropes, connecting the boundary layer to the upper troposphere. This corroborates with the findings of Sheldon et al. (2017), who suggested that lower Gulf Stream SSTs led to reduced upward transport via WCBs.

Now with the block formed over the North Atlantic, cold dry air is continually advected over the Gulf Stream (Bjerknes 1964, Cayan 1992, Cellitti et al. 2006, Kolstad et al. 2009) as seen in Fig. 3.5, initiating the positive feedback mechanism that maintains the block. This cold dry air keeps the THF anomalously high, which results in negative PV air masses being repeatedly deposited into the upper troposphere, acting against any decay process within this dynamically unstable object (Holmberg et al. 2023). However, this continuous removal of heat from the ocean lowers the heat content, as seen in Fig. 3.6 (top panel), Fig. 3.7 (bottom panel), resulting ultimately in a reduced THF. The length of time for this positive feedback to diminish is determined by the amount of surplus heat in the WBC and therefore, the duration of the block is determined, in part, by the oceanic preconditioning. Once the supply of negative or low PV air mass has been cut off, the block begins to decay. This negative feedback process is also seen in Cobb & Czaja (2019) in which the reduction (extension) of the warm core of the Gulf Stream, as a result of consecutive negative (positive) NAO periods, resulted in less (more) negative PV air masses occurring in the atmospheric boundary layer of this region. The timescale of this negative feedback driven by air-sea interactions in our study is about 3 months.

3.4 Discussion

3.4.1 Method

In the heat content composite analysis, we observed a strong ENSO signal seen in the Pacific (not shown). As a result, the ENSO 3.4 (Huang et al. 2017) signal was removed from the oceanic heat content fields and the composite time series using a linear regression in order to check whether this had any influence on the composites. We found it did not and we are thus confident that the heat content anomalies seen in Fig. 3.7 are not related to ENSO variability.

3.4.2 Orders of Magnitude

We now check that the qualitative arguments summarized in Fig. 3.8 are quantitatively plausible by calculating orders of magnitude for the associated steps. Starting with the oceanic preconditioning, as illustrated in Fig. 3.8 label **A**, considering that the Florida Straits heat transport time series (refer to Table 3.1) has a standard deviation of $O(10^{14}\mathrm{W})$ and the heat content anomalies in Fig. 3.7 (middle panel) are $O(10^{8}\mathrm{Jm}^{-2})$ with an area of $O(10^{12}\mathrm{m}^{2})$, this suggests that the timescales needed to create these oceanic heat anomalies are on the order of months. Analyzing the autocorrelation of the heat transport time series shows this index decorrelating with itself after one month, and hence these heat anomalies are consistent with oceanic heat transport. This oceanic transport timescale is also observed by Hirschi et al. (2019).

Considering the magnitude of the quantities above can give further insight into the amount of negative moist PV that air-sea interactions can generate, as illustrated in Fig. 3.8 label **B**. The change in moist PV in the boundary layer, ΔQ_e, as a result of heat exchange from the ocean to the atmosphere can be given by (see Appendix):

$$\Delta Q_e = -f\left(\frac{\Delta t_A}{\Delta t_O}\right)\frac{\Delta HC}{C_A(\rho_{BL}h_{BL})^2}, \tag{3.2}$$

where Δt_A is the timescales an air particle interacts with the WBC $O(10^5\mathrm{s})$, Δt_O is the oceanic timescale $O(10^6\mathrm{s})$ as discussed above and seen in Fig. 3.6 (top panel), f is the Coriolis parameter $O(10^{-4}\mathrm{s}^{-1})$, ρ_{BL} is the density of air in the atmospheric boundary layer $O(1\mathrm{kgm}^{-3})$, h_{BL} is the

height of the atmospheric boundary layer $O(10^3\text{m})$ and $C_A = 1005\text{Jkg}^{-1}\text{K}^{-1}$ is the specific heat capacity of air. As stated above, the excess heat content per area in the oceanic mixed layer prior to an increased period of blocking, ΔHC, is $O(10^8\text{Jm}^{-2})$. This results in an upper bound on the amount of moist PV generated by excess oceanic heat content of $O(1\text{PVU})$. Approaching this calculation from both an air-sea flux and a warm water transport anomaly perspective (both with orders of magnitude of $O(10^2\text{Wm}^{-2})$) results in the same generation of negative moist PV of $O(1\text{PVU})$. Although this magnitude serves as an upper bound, Fig. 8(d) from Vannière et al. (2016) demonstrated that the generation of negative moist PV in the cold sector is on the order of 1 PVU per day due to THF, a value comparable to that for moist PV.

Finally, considering the moist-adiabatic transport of this boundary layer air mass to the upper troposphere, as illustrated in Fig. 3.8 label **C**, we can approximate the boundary layer moist PV to the upper-level PV due to the absence of moisture sources upon ascent, i.e., $\Delta Q_e \approx \Delta Q_{Upper}$. Assuming conservation of mass along the WCBs, then the ratio of oceanic contributions to atmospheric blocking can be given by (see Appendix):

$$r = \left(\frac{\Delta P_{BL}}{\Delta P_{Block}}\right)\left(\frac{A_{BL}}{A_{Block}}\right)\left(\frac{\Delta Q_{BL}}{Q_{Block}}\right), \tag{3.3}$$

where ΔP represents the pressure difference from the bottom to the top of the volume considered, and A is the horizontal area of that same volume. Since latent heating does not affect moist PV, and therefore negative moist PV is primarily generated in the boundary layer, examining the white contours in Fig. 3.4 suggests that approximately $O(10\%)$ of the total boundary layer air mass over the North Atlantic is transported to the upper troposphere. This implies that the area of air mass in the boundary layer that contributes to atmospheric blocking is $A_{BL} \approx O(10^6\text{km}^2)$ which is the same order of magnitude as the area of the block, A_{Block}. Given that the thickness in the block, ΔP_{Block}, is 350hPa, and that of the boundary layer, ΔP_{BL}, is 50-100 hPa, and since the negative anomalies generated in the boundary layer are of the same order of magnitude as the negative PV anomalies in the block $O(1\text{PVU})$, this suggests that oceanic pathways contribute about $r \approx \frac{50-100}{350} \times 1 \times 1 \approx 15\% - 30\%$. This value is remarkably similar to the observations of Yamamoto et al. (2021).

3.4.3 Prediction

By far, the earliest precursor to increased atmospheric blocking over the North Atlantic, as revealed by our study, is the heat transport through the Florida Straits. As shown in the top panel of Fig. 3.6, the heat transport in JAS (ASO) exhibits a significant correlation with the atmospheric blocking area in DJF (JFM) with a coefficient of 0.57 (0.76 not shown). While the anomalous heat transport shows some dependence on atmospheric forcing via Ekman transport, Hirschi et al. (2019) demonstrated that the volume transport, and consequently the heat transport, through the Florida Straits can partly be explained by variations in the length of the Loop Current in the Gulf of Mexico. When a vortex is shed by this current into the Gulf of Mexico, the volume of the Loop Current contracts, leading to an increased heat transport through the Florida Straits into the North Atlantic. Astonishingly, this vortex shedding in the Loop Current closely mirrors the wave-breaking process that occurs in the jet stream, ultimately forming atmospheric blocks.

It is important to emphasise that we are not advocating that this process creates a block, rather that it biases the statistics. To draw an analogy, if the occurrence of atmospheric blocks were akin to rolling a dice, oceanic preconditioning effectively changes the dice to a weighted one. Given the high correlation values, this underscores the significance of the Florida Straits heat transport, and possibly the Loop Current, as a source of predictive skill for atmospheric blocking.

3.5 Conclusion

In this study, atmospheric and oceanic variables were analysed preceding, during and succeeding blocking events using ERA5 (1979-2020), ARGO (2004-2018) and RAPID (2004-2018) data sets. It was shown that:

- Blocking presence over the North Atlantic is linked to increased oceanic heat transport through the Straits of Florida several months prior, followed by an anomalously high oceanic heat content along the Gulf Stream and its extension, and finally with near simultaneous air-sea interactions over the same region.

- The turbulent heat flux over the Gulf Stream and its extension strongly correlates with the PV in the atmospheric boundary layer over the same region. This diabatic process is a major contributor to the generation of negative PV air mass in the boundary layer.

- Negative PV air masses were observed to be transported from the atmospheric boundary layer along the warm conveyor belt of a cyclone to the upper troposphere, where it was found to contribute to the negative PV anomaly of an atmospheric block.

- Air masses with negative PV were observed throughout the troposphere, with the majority of the negative PV present in the boundary layer, followed by 300hPa, and finally the middle troposphere. The reduction in negative PV frequency in the middle troposphere indicates the effects of diabatic processes along the warm conveyor belt. These were not observed when examining negative moist PV frequency.

- We hypothesize that when a block is formed over the North Atlantic, it can feedback positively on itself through the advection of cold dry air over the Gulf Stream, resulting in continued high turbulent heat flux, which maintains the block.

- We further hypothesize that the continued high turbulent heat flux eventually removes the surplus heat from the ocean, which leads to the decay of this air-sea interaction. This severs the atmospheric block from its maintenance pathway, resulting in a negative feedback effect. This suggests that the block's duration is determined, in part, by the surplus heat in the ocean prior to the block.

- Observations suggest a predictive skill in wintertime blocking area arising from the previous summer heat transport by the ocean across the Florida Straits (correlations of 0.6 and higher depending on the period of interest).

It is important to emphasize that, traditionally, atmospheric blocking has been understood within the context of dry and adiabatic quasi-geostrophic dynamics (Shutts 1983). In this view, the ocean's role is limited to introducing only perturbations to this dynamics, which is not inconsistent with our results. Nevertheless, in many studies of this type, Marshall & Molteni (1993) for example, there is an assumed underlying structure of the dynamics, which our study suggests could be attributed to air-sea interactions and could also lend more credence to the view that North Atlantic blocking reflects a fundamentally coupled phenomenon between

ocean and atmosphere. Preliminary results from a simple dynamical system model, similar to the work of Palmer (1993), indicate that the different time scales between the atmosphere and the ocean can generate this intrinsic chaotic behaviour of the coupled system. Ultimately, numerical experiments with high-end climate models are is required to thoroughly test this intriguing new paradigm for atmospheric blocking in the North Atlantic.

Chapter 4

Testing the Gulf Stream's Influence on Atmospheric Blocking

The bulk of this chapter is based on the paper "Gulf Stream Moisture Fluxes Impact Atmospheric Blocks Throughout the Northern Hemisphere" (Mathews et al. 2024), submitted to Geophysical Research Letters in February 2024. For this work, I ran ensemble forecasts on the ECMWF IFS with the assistance of Dr. Frederic Vitart and Dr. Christopher Roberts and analysed the output.

Key findings: Gulf Stream moisture flux suppression reduces atmospheric blocking across the northern hemisphere.

4.1 Introduction

Understanding the mechanisms governing the formation and persistence of large-scale anticyclonic anomalies, commonly known as atmospheric blocks, is crucial for advancements in weather forecasting (Grams et al. 2018) and predicting the associated extreme temperatures (Pfahl & Wernli 2012). Nearly a decade ago, Pfahl et al. (2015) linked these synoptic-scale features to upstream latent heating, an observation later substantiated by Steinfeld et al. (2020). Their experiment, suppressing latent heating along the warm conveyor belt of a cyclone, resulted in the subsequent suppression of atmospheric blocks, with some blocks failing to form at all.

The ocean's role as a primary moisture source for atmospheric blocks was highlighted by Yamamoto et al. (2021), with theories by Mathews & Czaja (2024) suggesting that western bound-

ary currents, like the Gulf Stream, modulate atmospheric blocking. This link was evidenced by increased blocking following heightened Gulf Stream heat transport, leading to warm water anomalies that boost surface latent heat flux (SLHF), and consequently moisture, aiding block formation by transporting anomalously low potential vorticity (PV) air from lower to upper levels (Wenta et al. 2024).

Emphasis has also been placed on both oceanic and atmospheric resolution to accurately represent air-sea interactions in coupled models (Hewitt et al. 2017). Notably, Famooss Paolini et al. (2022) found that models with atmospheric resolution coarser than 50km exhibited an entirely different response to sea surface temperature anomalies, showing weakened vertical motion and meridional transient eddy heat transport.

In this study, we examine the impact of moisture fluxes from the Gulf Stream region on atmospheric blocking in the northern hemisphere (NH) through a sensitivity experiment conducted using the European Centre for Medium-Range Weather Forecasts (ECMWF) Integrated Forecast System (IFS). While this study emphasises changes in atmospheric blocks, we also examine the effect on the broader Rossby wave spectrum. The paper is laid out as follows: Section 4.2 describes the model setup and the diagnostic methods used. Section 4.3 shows the effects Gulf Stream moisture suppression has on the upper troposphere, followed by our conclusions in Section 4.4.

4.2 Data and Methodology

4.2.1 Model Set Up

The results in this study are based on coupled ensemble reforecasts using the ECMWF IFS cycle 47r3 (ECMWF 2023), configured as follows. The atmosphere is set up with 15 ensemble members, 137 model levels and run on Tco639, Tco319, and Tco199 cubic octahedral reduced Gaussian grids, corresponding to resolutions of approximately 18km, 32km, and 50km, respectively. The IFS is coupled hourly to a 75-level NEMO v3.4 ocean model (Madec et al. 2017) and an LIM2 sea ice model (Bouillon et al. 2009, Fichefet & Maqueda 1997), both utilising the ORCA025 tripolar grid with a grid spacing of approximately 0.25°. The ocean and atmosphere are fully coupled throughout the 46-day forecast, producing output every 12 hours. Fifteen reforecasts are used, and the initial dates are listed in Table 4.1. This results in a total of 690

Table 4.1: Initial dates used for the reforecasts and the date the first block was detected over the North Atlantic in ERA5 data. Winter reforecasts are depicted in **bold**.

Initial Dates	Block Detected
10th December 2009	13th December 2009
9th December 2010	13th December 2010
27th December 2016	30th December 2016
14th May 2018	17th May 2018
30th March 2019	2nd April 2019
19th May 2019	22nd May 2019
20th June 2019	23rd June 2019
20th July 2019	24th July 2019
11th September 2019	14th September 2019
14th October 2019	18th October 2019
19th November 2019	22nd November 2019
27th November 2019	30th November 2019
12th January 2020	18th January 2020
15th January 2020	18th January 2020
21st November 2022	1st December 2022

forecasted days, with 414 falling in extended winter (NDJFMA) and 276 in extended summer (MJJASO). The atmospheric, land, and wave fields were initialised from ERA5 (Hersbach et al. 2020), while the ocean and sea ice fields were initialised from OCEAN5 and ORAS5 respectively (Zuo et al. 2019). These dates were chosen based on the occurrence of a cyclone over the North Atlantic preceding the initial block detected in the North Atlantic or Europe region, as observed from ERA5 data. The forecast was initiated approximately 4 days before the observed block was initially detected to allow the contributing cyclone to sufficiently interact with the Gulf Stream. These events were chosen randomly with priority given to more recent dates due to higher-quality data assimilation (de Rosnay et al. 2022). All results shown are for resolution Tco639 unless otherwise specified.

To assess the impact of Gulf Stream (GS) SLHF on atmospheric blocking, a sensitivity experiment was conducted. It compared the full physics control run to a corresponding simulation with GS SLHF suppressed (here-after referred to as NO_GS_SLHF). GS SLHF is turned off by applying a mask to the moisture transfer scheme (ECMWF 2021), preventing moisture transfer where the mask is applied. This mask linearly relaxed, allowing complete moisture transfer after a distance of 5° from the original mask, as illustrated by the grey contours in Fig. 4.1. The mask roughly corresponds to the region of 200Wm^{-2} SLHF from wintertime ERA5 climatology

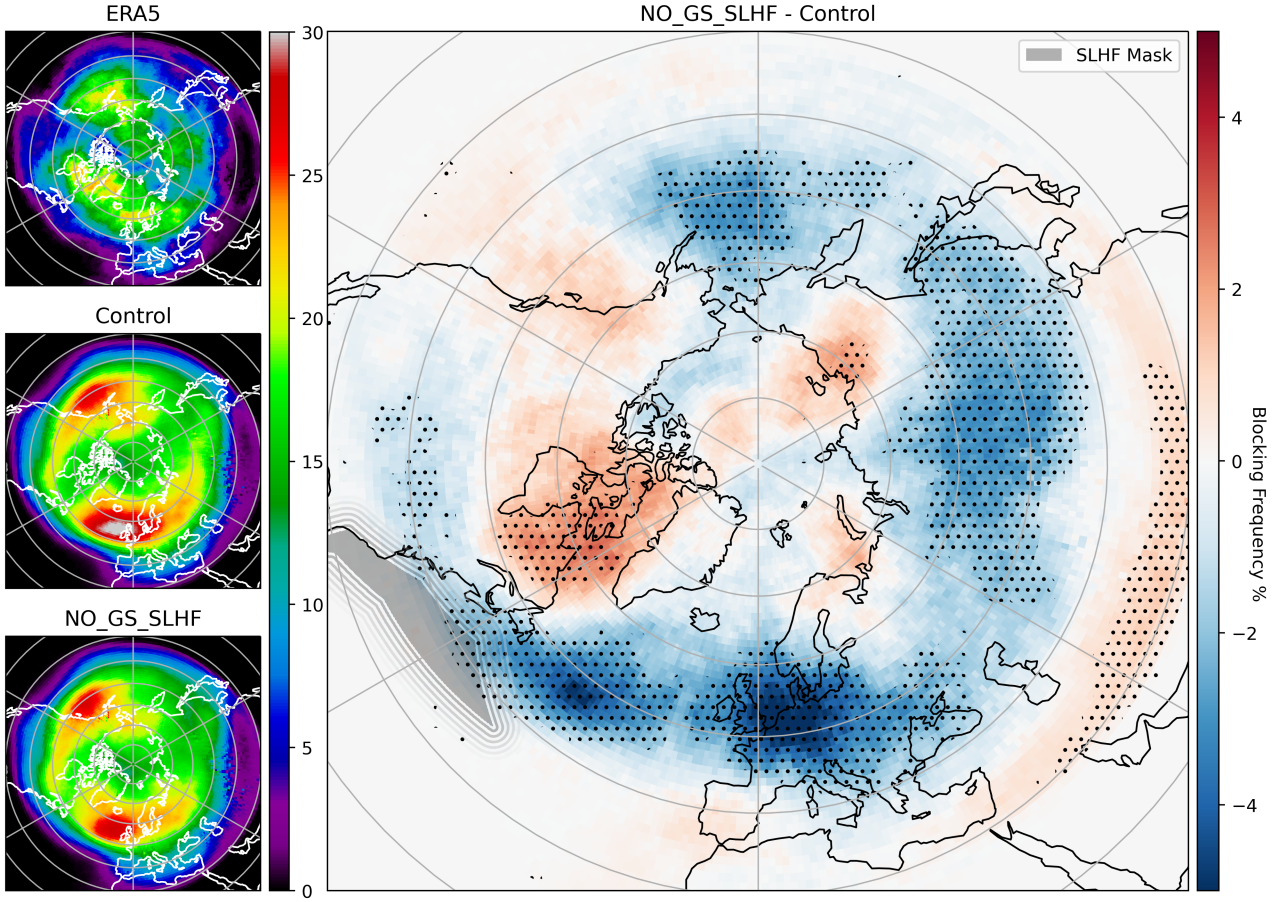


Figure 4.1: Mean blocking frequency for ERA5 (top left), the control run (middle left), the NO_GS_SLHF run (bottom left), and the difference between the NO_GS_SLHF and control runs (right). The grey contours indicate the SLHF mask applied, with the darkest (lightest) contour indicating complete suppression (permission). Stippling indicates areas that exceed the 95% confidence interval.

in the North Atlantic and was applied throughout the entire run.

4.2.2 Diagnostic Methods

Following Schwierz et al. (2004), blocking is identified as an upper-level negative PV anomaly that surpasses defined thresholds for overlap, amplitude, spatial scale, and duration. Initially, the PV field is averaged between 500hPa and 150hPa, and a two-day running average is applied. To calculate the anomaly, a two-day smoothed daily ERA5 climatology is subtracted from the averaged PV field. The upper PV anomaly field is then analysed using the Steinfeld (2020) algorithm, with thresholds for overlap, duration, amplitude, and size being 40%, 5 days, -1.2PVU and 10^6km^2 respectively. The relatively low overlap threshold is chosen due to the 12-hourly temporal output from the model and to maximise the difference between the

NO_GS_SLHF and control runs. Various threshold values were tested, and most results were comparable across different overlap and amplitude thresholds, as discussed in Section 4.3.4. Each detected block is labelled, and its characteristics, including duration, size, and intensity (total PV per area), are calculated for each time step. These characteristics are related to the overall blocking frequency in the NH, as seen in Table 4.2, through the equations:

$$\text{Frequency}(x, y) = \frac{1}{TDM} \sum_{t=1}^{T} \sum_{d=1}^{D} \sum_{m=1}^{M} f(x, y, t, d, m), \tag{4.1}$$

$$f(x, y, t, d, m) = \begin{cases} 1, & \text{if blocking is detected at grid point} \\ 0, & \text{otherwise} \end{cases}, \tag{4.2}$$

$$\iint_{NH} \text{Frequency}(x, y) dx dy = \frac{\sum_{n=1}^{N} \text{Duration} \times \overline{\text{Size}}}{\text{Forecast Length}}, \tag{4.3}$$

where T, D, M, and N represent the number of time steps, initial dates (as seen in Table 4.1), ensemble members, and blocks detected, respectively. The over-bar denotes the average over the life cycle of the block.

The phase speed-wavenumber analysis follows the approach outlined in Jiménez-Esteve et al. (2022). First, a fast Fourier transform is applied in both the longitudinal and temporal directions. Then, the phase speed of the Rossby waves is calculated according to Randel & Held (1991), weighting this spectrum along latitudinal directions. Finally, the spectrum is averaged along the latitudinal direction.

Warm Conveyor Belts (WCBs) are identified using the convolutional neural network from Quinting & Grams (2022). This neural network takes a number of input fields, such as relative humidity, relative vorticity, moist potential vorticity etc., and outputs a probability of there being a WCB inflow, ascent and outflow. If these probabilities are above a certain threshold, the field is masked to identify a WCB.

Statistical significance at the 95% confidence interval is determined using a two-tailed t-test between the ensemble members of the NO_GS_SLHF and control runs.

4.3 Results

4.3.1 The Effect on Atmospheric Blocking

Fig. 4.1 compares average blocking frequencies from ERA5 data covering the same dates as the IFS experiment, control, and NO_GS_SLHF simulations over a 46-day forecast. Both simulations show a more extensive frequency of atmospheric blocking across the Northern Hemisphere than observed in ERA5, with a smoother signal attributed to ensemble averaging. The overestimation of blocking frequency in our experiments is in contrast to the underestimation identified in previous IFS versions (e.g. Davini et al. (2021)), but is consistent with a positive NH blocking frequency bias in ECMWF operational reforecasts for the same IFS cycle when calculated over a longer period (not shown). The NO_GS_SLHF simulation reveals a significant decrease in blocking frequency, by up to 30%, over the North Atlantic storm track, Western Europe, Russia, and the North Pacific compared to the control, as highlighted in the right panel of Fig. 4.1. Conversely, NO_GS_SLHF shows an increase in blocking over northeastern Canada and central Asia, though with a smaller spatial footprint and intensity, suggesting a complex shift in blocking patterns.

We evaluated the sensitivity of blocking to GS moisture fluxes using a geopotential height reversal index (Davini et al. 2012) and a geopotential height anomaly index (Woollings et al. 2018). Interestingly, the diagnosed biases are sensitive to the choice of blocking index, with IFS forecasts under-representing blocking frequency compared to ERA5 with the reversal index (Fig. 4.2) but slightly over-representing blocking frequency with the anomaly index (Fig. 4.3). Nevertheless, both geopotential indices are consistent with the PV blocking metric and show a decrease in blocking frequency over the North Atlantic storm track and Europe when moisture flux is suppressed, with a similar relative magnitude. However, only the anomaly indexes shows a strong signal propagating to the North Pacific basin, as depicted in Figure 4.1.

Results from the first two weeks of reforecasts align more closely with ERA5 (Fig. 4.4), indicating a significant decrease in blocking over the North Atlantic and Western Europe in the NO_GS_SLHF run compared to the control run. This suggests that the signal has not had sufficient time to propagate from the North Atlantic to the North Pacific. A reduction in blocking frequency across the entire Northern Hemisphere during this period was observed, as outlined in Table 4.2.

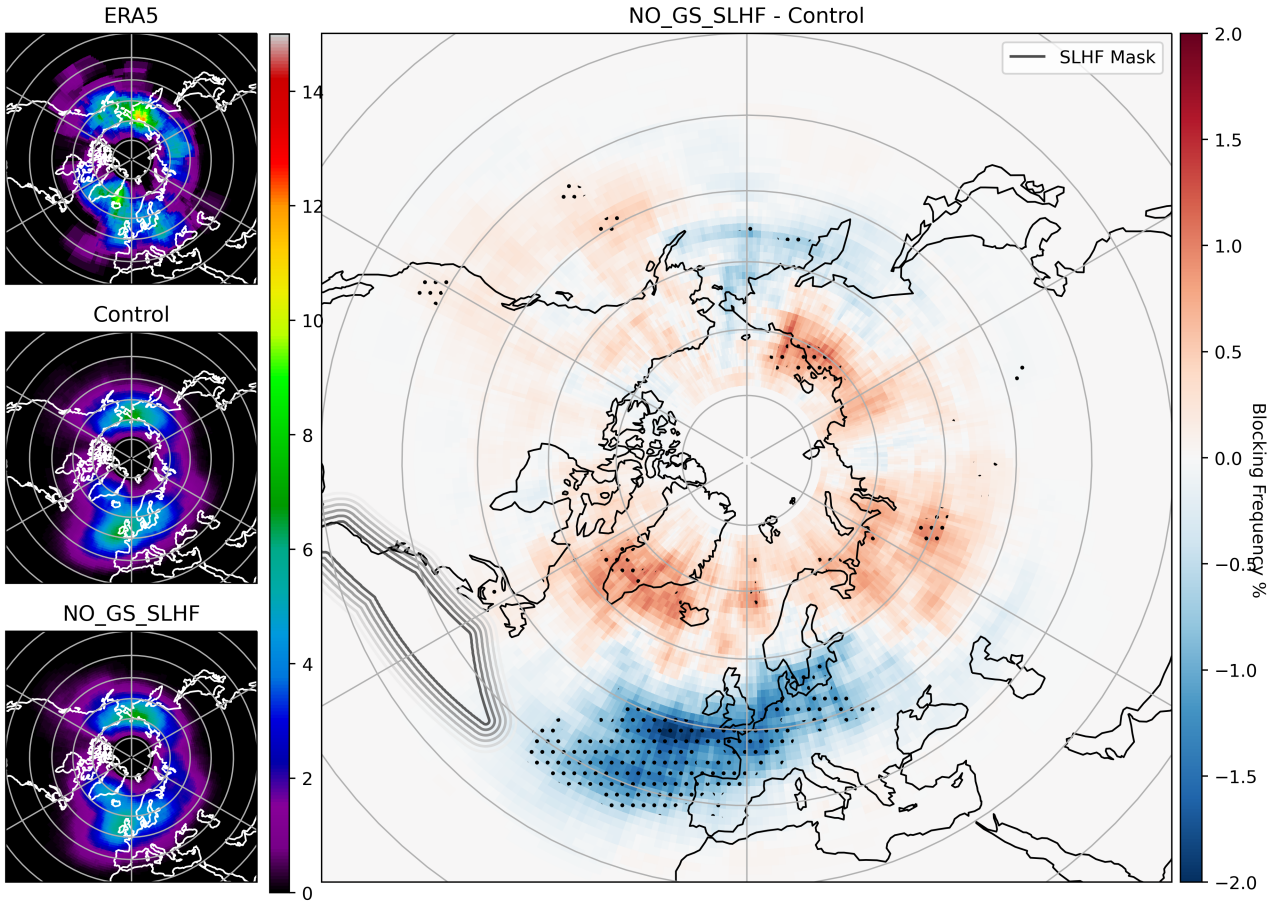


Figure 4.2: As in Fig. 4.1 but now calculated using the **geopotential height reversal index**.

Table 4.2: Percentage change in blocking frequency over the NH relative to the control run for the entire reforecast period is presented. The first two weeks of the forecast are shown in brackets. Winter reforecasts correspond to NDJFMA, while Summer corresponds to MJJASO, as indicated in Table 4.1. Results significant over the 99% confidence interval are depicted in **bold**.

Resolution	All Dates	Winter	Summer
Tco639	**-4.34%** (**-4.22%**)	**-5.9%** (**-6.64%**)	**-2.45%** (-1.33%)
Tco319	**-3.88%** (**-2.96%**)	**-5.32%** (**-4.90%**)	**-2.60%** (-0.18%)
Tco199	**-3.35%** (**-3.55%**)	-3.30% (**-5.27%**)	**-3.41%** (-1.51%)

These results show that, in the first half of the forecast, the IFS is in good agreement with ERA5. However, in the latter half of the forecast, both the control and NO_GS_SLHF runs significantly overestimate blocking frequency when using the PV index from Schwierz et al. (2004) seen in 4.1. Conversely, when using the geopotential height reversal index to detect atmospheric blocks, as seen in Fig. 4.2, the IFS experiments and ERA5 are in greater agreement for the entire run. For all indices, the simulated blocks appear to be located closer to Europe, with less blocking

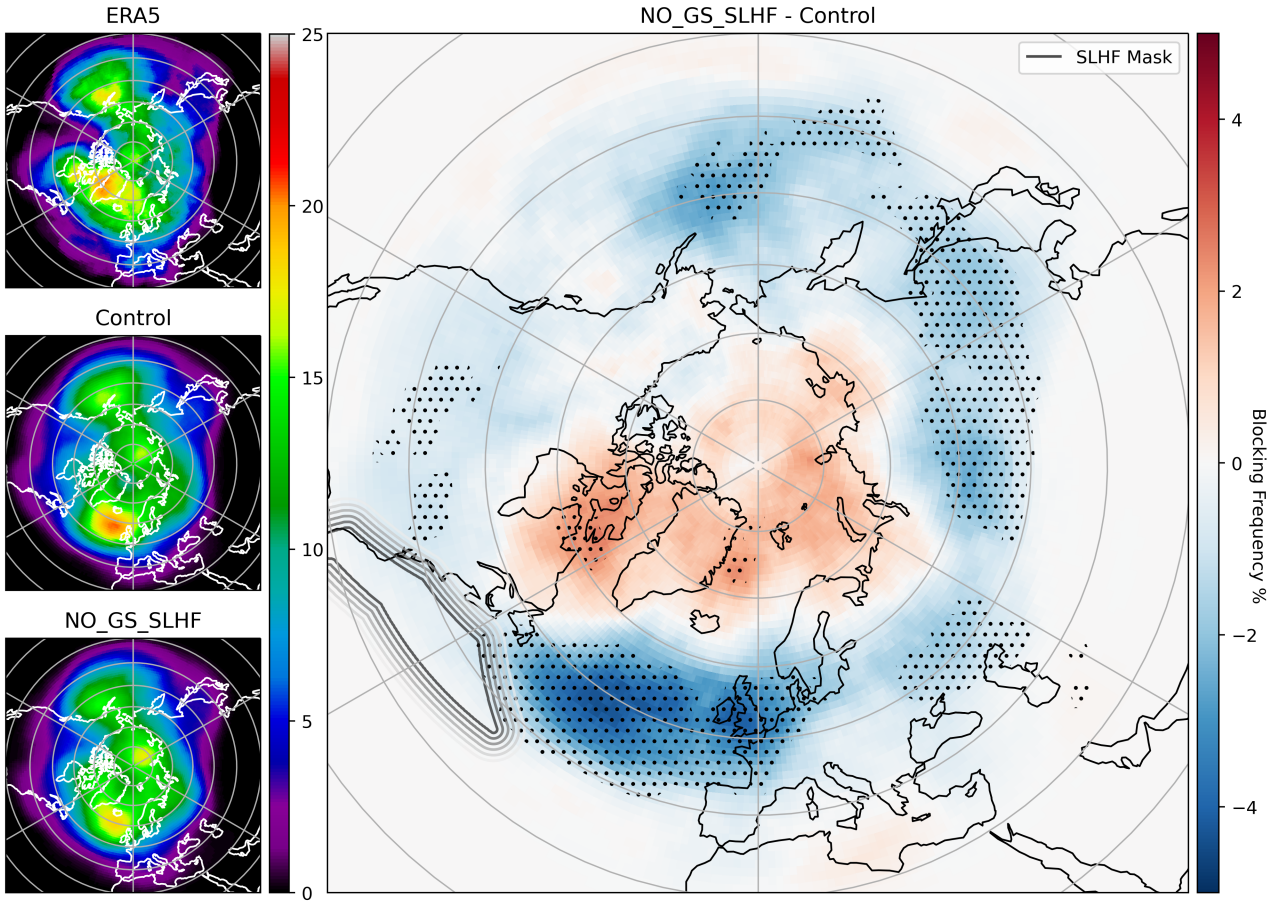


Figure 4.3: As in Fig. 4.1 but now calculated using the **geopotential height anomaly index**.

observed over Greenland compared to reanalysis. In the North Pacific, the spatial distribution of blocking frequency in the IFS runs appears to be in good agreement with ERA5.

Turning to the seasonal strength of this signal, the same analysis was conducted for dates within the extended winter (NDJFMA) and extended summer (MJJASO) periods, comprising of 9 and 6 initial dates respectively, as indicated in Table 4.1. The results of this seasonal analysis are presented in Fig. 4.5. The summer composite reveals a significant decrease in blocking over the North Atlantic storm track, Western Europe, Northern Japan, and the North Pacific. Additionally, during winter, a more prominent area of reduced blocking spans from the Western North Atlantic to East Asia, accompanied by a signal in the North Pacific. Expanding this perspective to encompass the overall change in blocking frequency across the NH, once more, the dominance of the signal in extended winter becomes evident, as displayed in Table 4.2. This finding remains robust to changes to initial date sample size.

Examining the changes in the atmospheric block's characteristics reveals the impact of air-

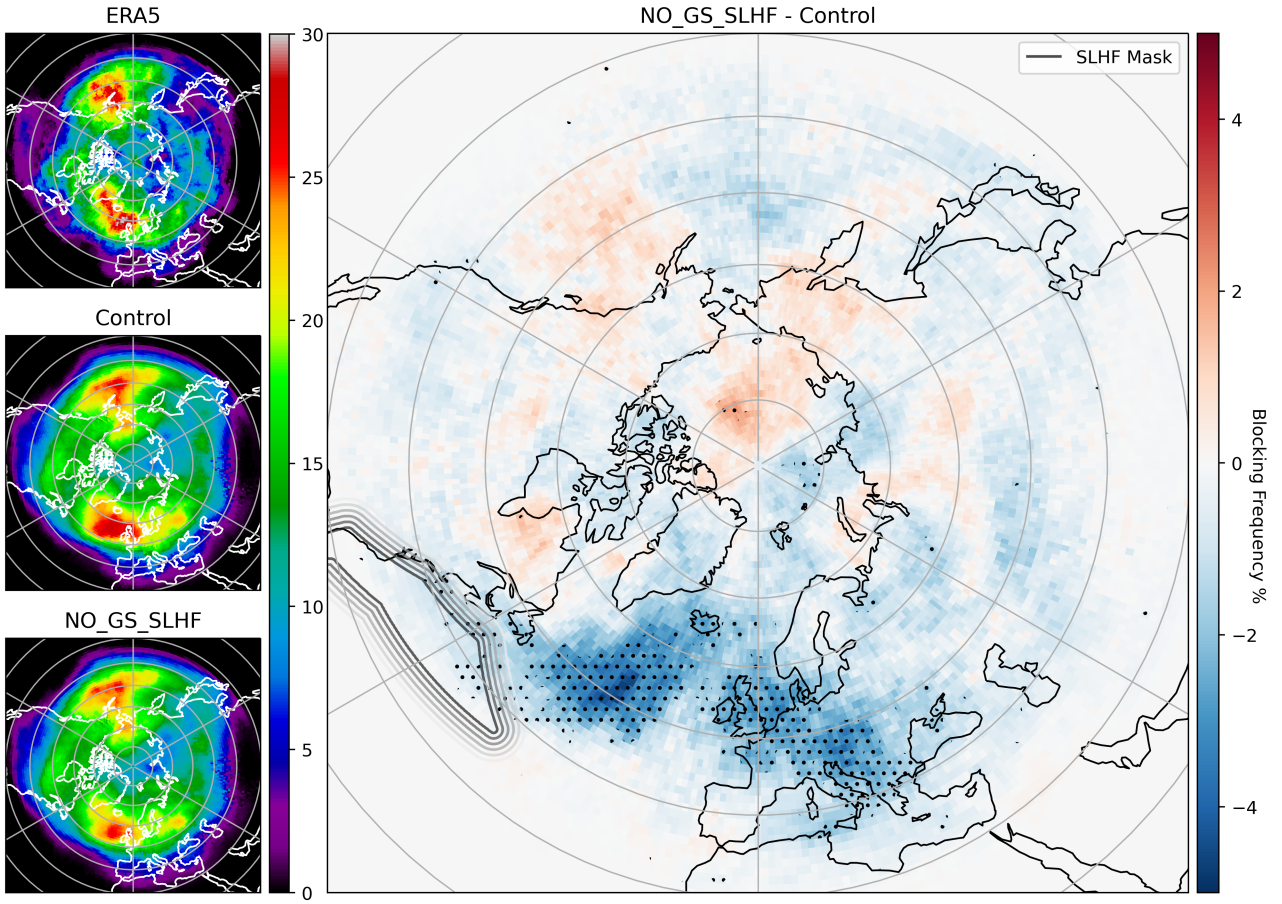


Figure 4.4: Mean blocking frequency for ERA5 (top left), the control run (middle left), the NO_GS_SLHF run (bottom left), and the difference between the NO_GS_SLHF and control runs (right) for the first two weeks of the reforecast. The grey contours indicate the SLHF mask applied, with the darkest (lightest) contour indicating complete suppression (permission). Stippling indicates areas that exceed the 95% confidence interval.

sea interactions on individual blocks. Figure 4.6 shows the probability distributions of these characteristics. The solid line, representing the mean value, illustrates that in the NO_GS_SLHF run, the blocks have shorter life cycles (-6.4%), a more compact spatial signature (-10.1%), and exhibit weaker intensity (-0.35%), indicating a weaker negative PV anomaly inside the blocks. Interestingly, the NO_GS_SLHF run detects more individual blocks compared to the control run (+16.5%). However, due to their decreased duration and size, this discrepancy is not substantial enough to result in an overall increase in blocking frequency, as indicated in Table 4.2 and seen in Fig. 4.1 and 4.5. The dotted lines in Fig. 4.6 illustrate the upper and lower quartiles of the distribution. This demonstrates that in the NO_GS_SLHF run, there is a narrower range of block durations and sizes, indicating reduced variability. Conversely, the NO_GS_SLHF run exhibits wider variability in the intensities of blocks.

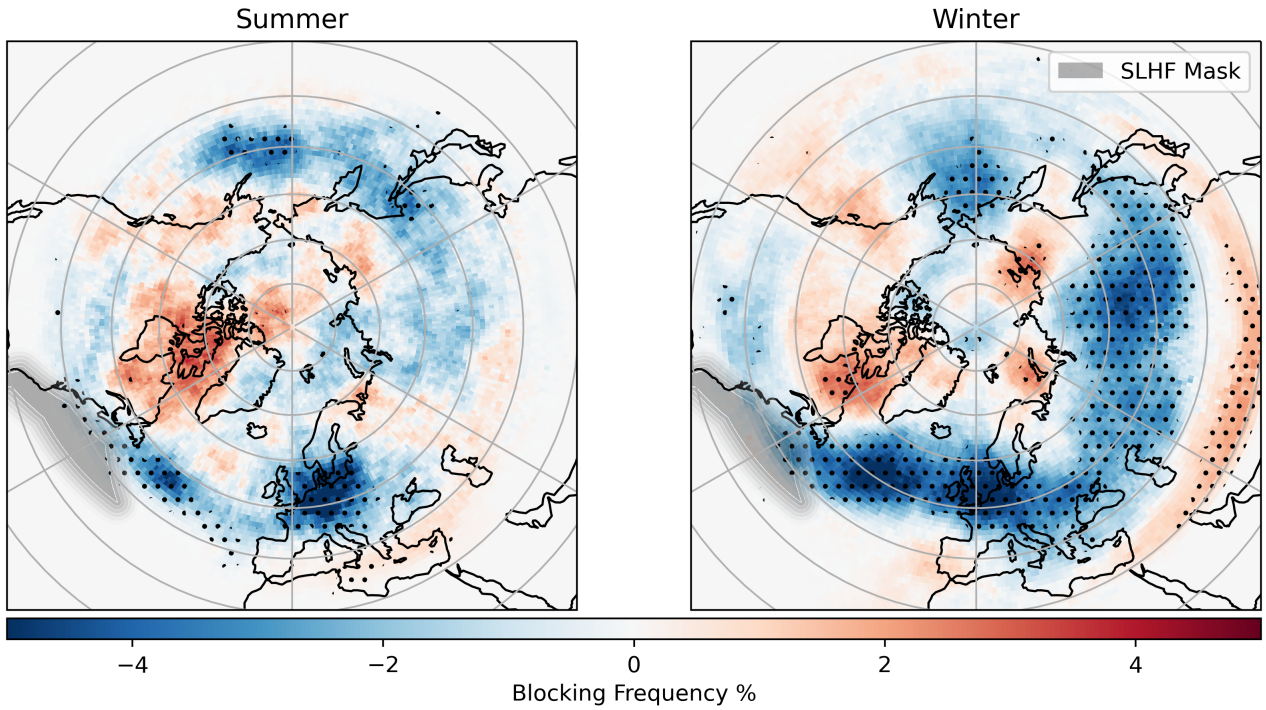


Figure 4.5: The difference in mean blocking frequency between the NO_GS_SLHF and control runs for the extended summer (left) and extended winter (right). The grey contours indicate the SLHF mask applied, with the darkest (lightest) contour indicating complete suppression (permission). Stippling indicates areas that exceed the 95% confidence interval.

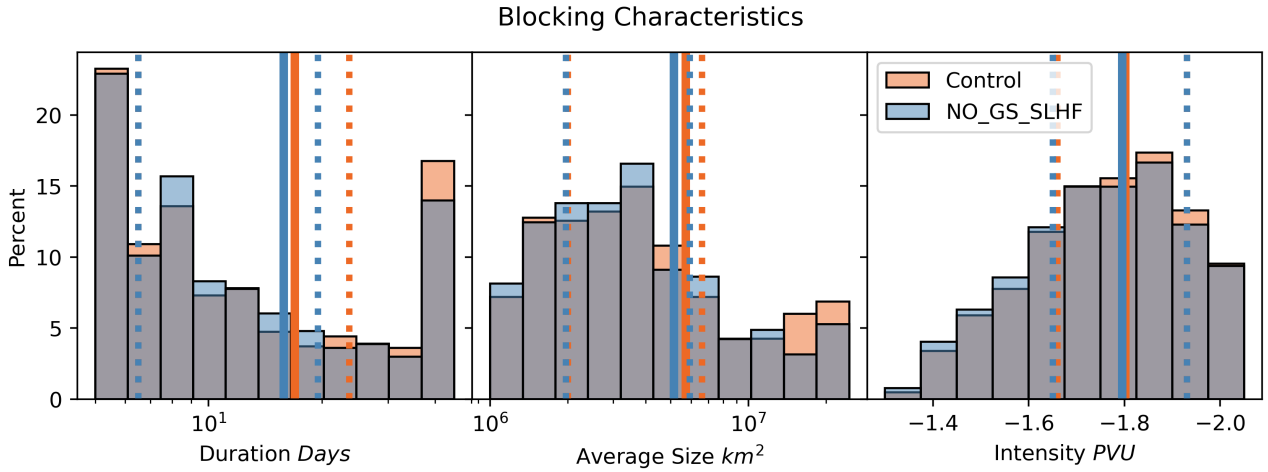


Figure 4.6: The distributions of the block characteristics for the control (light red) and NO_GS_SLHF (light blue) runs. From left to right the block's duration, average size, and intensity (total PV per area) are shown. Solid lines represent the mean values, while dotted lines represent the upper and lower quartiles.

4.3.2 Changes in the Jet Stream and Rossby Wave Characteristics

Examining the overall impact of suppressed GS SLHF on the jet stream across the NH, Figure 4.7a displays the difference in zonal wind at 250hPa between the NO_GS_SLHF and control

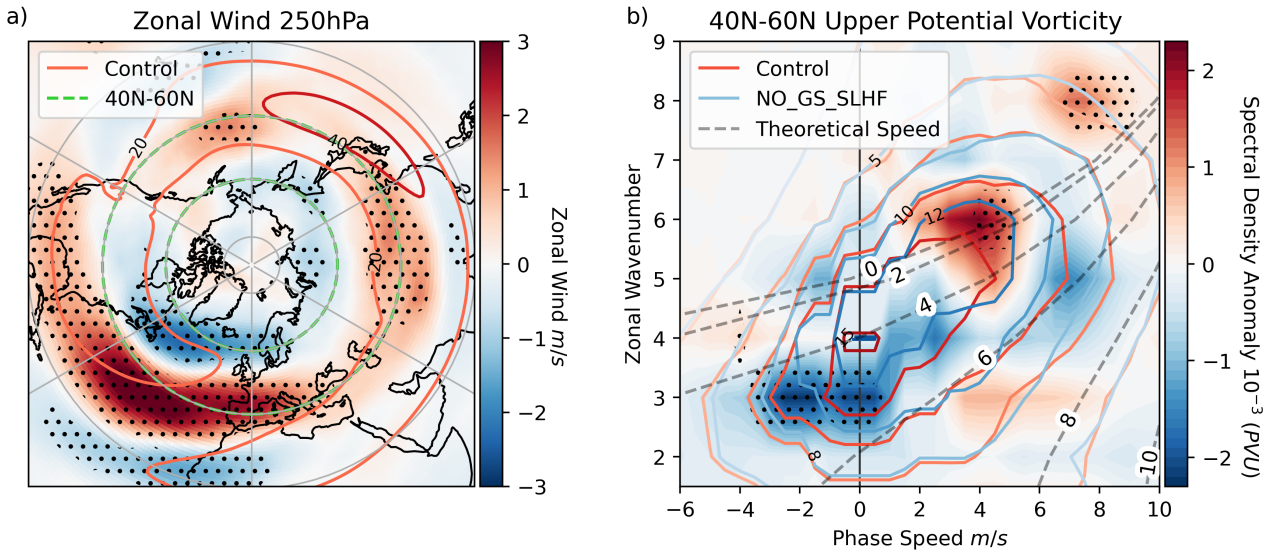


Figure 4.7: The zonal wind at 250hPa (a) and the power spectrum of the vertically averaged anomalous PV field from 500hPa to 150hPa within the latitudinal range of 40°N to 60°N (b) are presented. In both figures, the shading illustrates the difference between the NO_GS_SLHF and control runs, with the blue and red contours representing their respective reforecast means. The region between 40°N and 60°N is indicated by green dashed lines. The theoretical phase speed for different meridional wavenumbers at 40°N, applying a background flow of 16.4 m/s as observed, is depicted with grey dashed lines. Areas that exceed the 95% confidence interval are highlighted with stippling.

runs. The red contours represent the average zonal wind for the control run. In the North Atlantic, a shift towards the equator is observed in the polar jet, while a poleward shift is noted in the subtropical jet, suggesting at a merged jet. Downstream over central Asia and the North Pacific, indications of a poleward shift in the jet are observed. Moreover, a general increase in jet speed over the North Pacific correlates with the decrease in atmospheric blocking seen in Figs. 4.1 and 4.5. This finding agrees with Riboldi et al. (2020), who observed decreased blocking with increased zonal wind. Although there is a small but significant 0.9% increase in zonal wind across the entire NH in the NO_GS_SLHF run, there is no dipole signal when averaging above and below the jet stream maximum, suggesting no overall meridional shift in the jet stream. This result is further supported by meridional cross-sectional composites (Fig. 4.8).

Fig. 4.7b shows the power spectrum of the anomalous PV field from 500hPa to 150hPa, between latitudes 40°N and 60°N. It compares the spectral density of the NO_GS_SLHF (blue) and control runs (red), with shading indicating differences. Both runs exhibit slower eastward propagation with decreasing zonal wave number. The NO_GS_SLHF runs show more energy

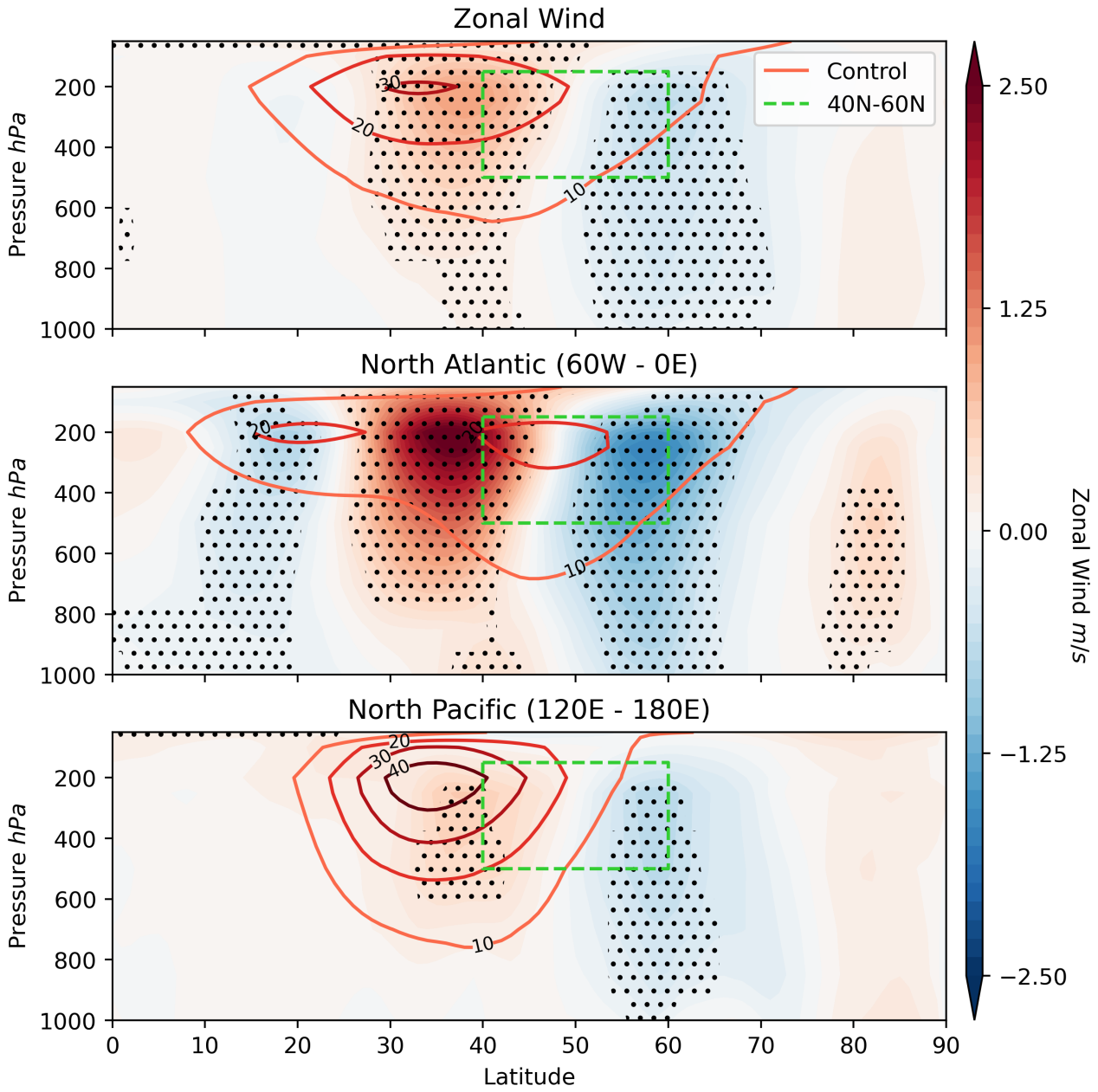


Figure 4.8: Meridional cross-section of the mean zonal wind for the entire Northern Hemisphere (top), the North Atlantic 60°W - 0°E (middle), and the North Pacific 120°E - 180°E (bottom). The control run is shown with the red contours, while the shading depicts the difference between the NO_GS_SLHF and the control runs. The dashed green box depicts the region where the spectral analysis is computed as in Fig. 4.7.

with higher wavenumbers, promoting faster eastward propagation. Conversely, the control run favours westward and stationary zonal waves with lower wavenumbers. With a negligible change in zonal wind speed (0.03m/s) between 40N-60N, the signal isn't due to changes in the jet speed but suppressed Rossby wave forcing. This aligns with smaller blocking sizes in the NO_GS_SLHF run, implying larger zonal wave numbers. This is consistent with the findings of

Riboldi et al. (2020), who associated low phase speed with atmospheric blocking.

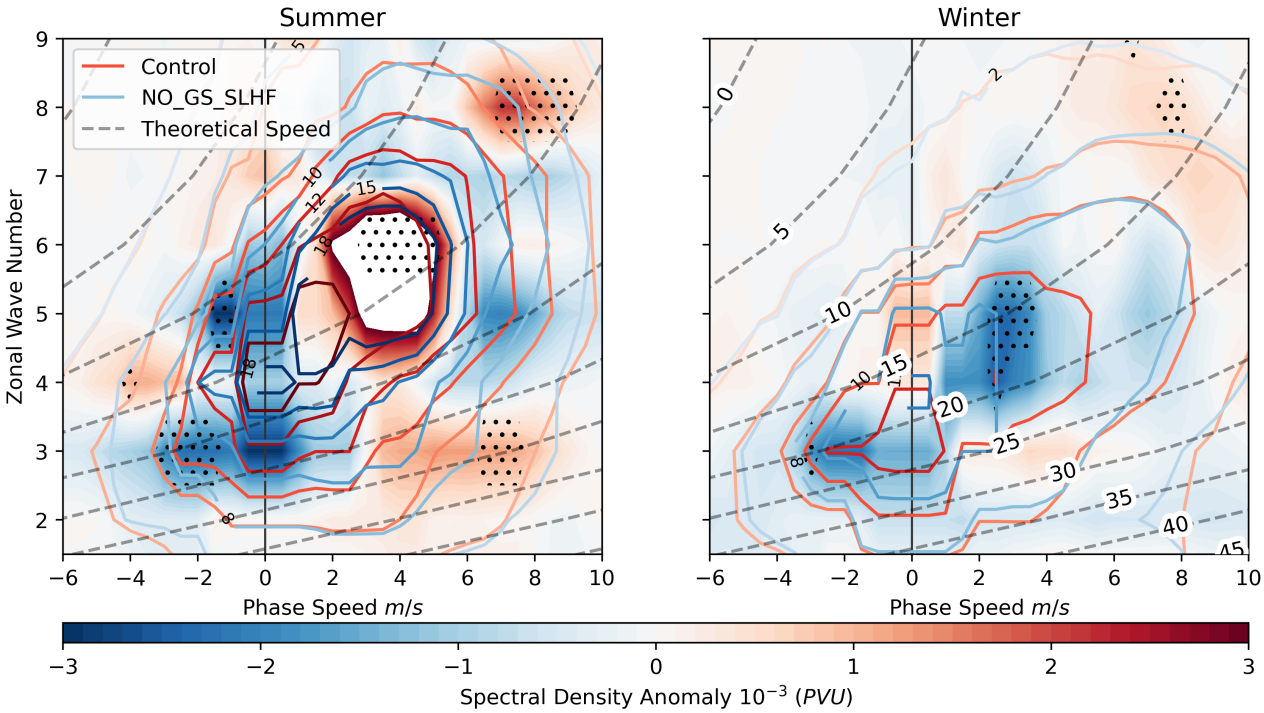


Figure 4.9: The power spectrum of the vertically averaged anomalous PV field from 500hPa to 150hPa within the latitudinal range of 40°N to 60°N for extended summer (left) and extended winter (right). The shading illustrates the difference between the NO_GS_SLHF and control runs, with the blue and red contours representing their respective reforecast means. The theoretical phase speed for different background flows at 40°N, applying a meridional wavenumber of 4, is depicted with grey dashed lines. Areas that exceed the 95% confidence interval are highlighted with stippling.

Examining the seasonal change in this signal (Fig. 4.9), the power spectrum shifts, with the most pronounced stationary wave changing from zonal wavenumber 4 in summer to 3 in winter, consistent with the increased zonal wind observed during winter. Furthermore, the difference between the NO_GS_SLHF and control runs shifts from the dipole signature seen in Fig. 4.7b in summer to an overall reduction of wavenumbers 3-5 in winter. This again underscores the comparatively strong signal exerted by air-sea interactions in winter compared to summer.

4.3.3 The Interrupted Oceanic Pathway

So far, we have seen that the effect of reduced moisture flux from the GS corroborates the observations and theory laid out in Chapter 3 and seen in Mathews & Czaja (2024), primarily that air-sea interactions act to maintain and sustain atmospheric blocks. We will now further test and scrutinize this theory by looking at the fields responsible for this diabatic modification

of air and the resulting transport from the atmospheric boundary layer to the upper troposphere where the block is formed.

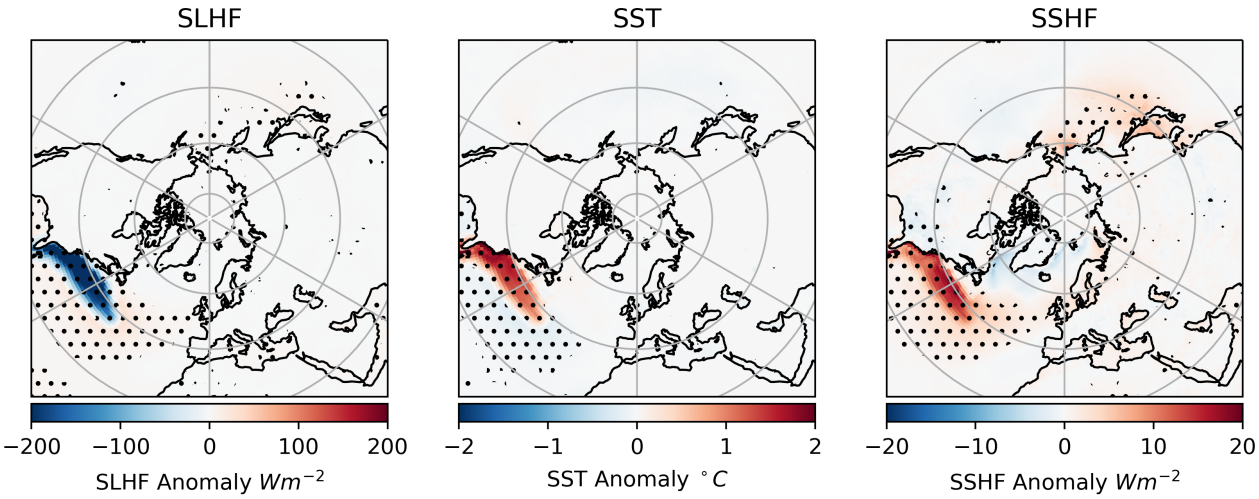


Figure 4.10: The difference between the NO_GS_SLHF and control runs for the SLHF (left), SST (middle) and SSHF (right). Stippling indicates areas that exceed the 95% confidence interval.

Fig. 4.10 shows the change in the oceanic fields when GS moisture flux is suppressed. The left panel shows a reduction of SLHF over the GS region that corresponds to the mask applied to this field as seen also in Fig. 4.1. Outside of this mask, there is an increase in SLHF from the ocean to the atmosphere. This is presumably due to the comparatively dry air in the NO_GS_SLHF run that has more capacity for moisture uptake outside of this region since it did not accumulate any moisture over the GS region. Notably, there is also a small but significant increase in SLHF over the Kuroshio extension. This suggests the possibility of "two-basin particles," as previously observed by Yamamoto et al. (2021). Here, however, these particles would originate in the North Atlantic and travel eastward to the North Pacific, as opposed to traveling eastward from the North Pacific to the North Atlantic. As before, these air parcels are presumably less moist due to the suppression in the NO_GS_SLHF run, allowing them to uptake more moisture over the Kuroshio.

The effect that this suppression has on SSTs and SSHF can be seen in the middle and right panels of Fig. 4.10 respectively. Notably, SLHF is an order of magnitude greater than SSHF and makes up the majority of the turbulent heat flux. With this suppressed, there is now less energy being removed from the ocean and hence the SSTs increase where this mask is applied. Now with increased SSTs, there is a stronger temperature difference over the GS mask and hence

the SSHF increases. Outside of this mask, the influence is less clear. With the increased SLHF, there is now more heat being removed from the ocean outside of this region and hence the SSTs are reduced; however, we still see an increase in the SSHF even with reduced SSTs. Possibly this air is still at a colder temperature in the NO_GS_SLHF run since there is reduced moisture and hence reduced latent heating, which would allow for stronger temperature differences between the SSTs and the boundary layer. Similarly, this could explain the positive SSHF signal seen over the Kuroshio assuming the interaction here is from "two-basin particles".

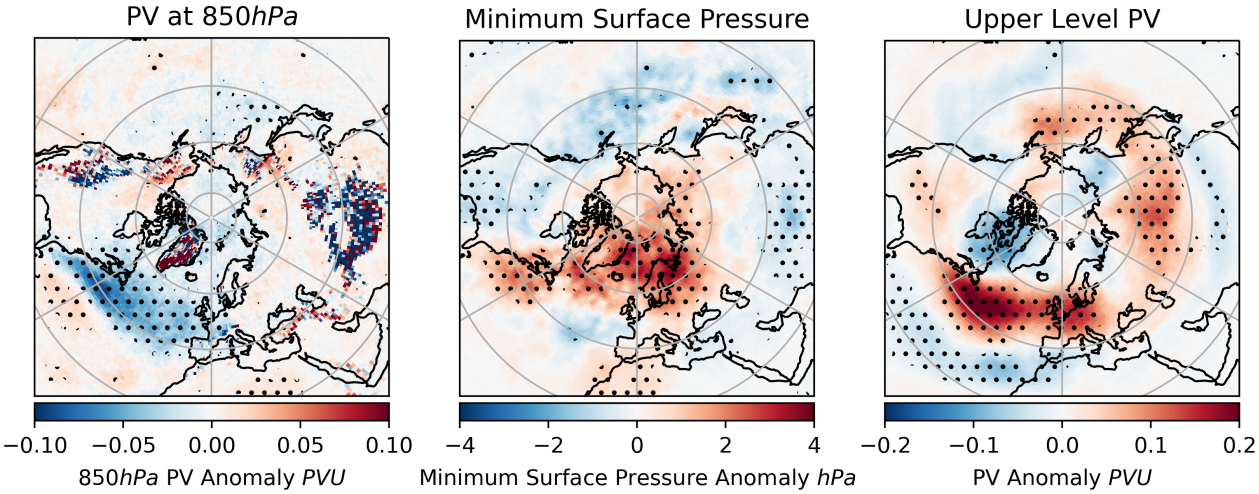


Figure 4.11: The difference between the NO_GS_SLHF and control runs for the PV at 850 hPa (left), minimum surface pressure throughout the forecast (middle), and PV anomaly between 150hPa and 500 hPa (right). Stippling indicates areas that exceed the 95% confidence interval.

The effect of these perturbed ocean fields on the atmosphere can be seen in Fig. 4.11. The left panel shows the PV at 850 hPa difference between the NO_GS_SLHF and control runs. This shows a dipole signal over the North Atlantic storm track with more negative PV anomalies on the northern side and positive anomalies on the southern side. Additionally, there is a small negative PV anomaly over the Kuroshio. These negative anomaly signals are likely a result of the increased SSHF in these areas that act to reduce the static stability of the boundary layer air. The middle panel shows the change in minimum surface pressure over the entire forecast, showing an overall increase in the minimum surface pressure over the North Atlantic storm track and into the Barents Sea suggestive of less deep cyclones due to the reduced moisture. There is a decrease of minimum surface pressure outside of the North Atlantic - European sector, although far less spatially compact and with a weaker magnitude. Finally, the right panel shows the difference in the PV between 150 hPa and 500 hPa between the NO_GS_SLHF and control runs. This shows a similar but opposite signal to the reduced blocking frequency

signal seen in Fig. 4.1. As blocking is measured here as a negative PV anomaly (Schwierz et al. 2004), these positive PV anomalies seen in the right panel are expected to coincide with a reduced blocking frequency. As in Fig. 4.1, this signal is strongest over the North Atlantic and Europe but extended to the North Pacific and even North America.

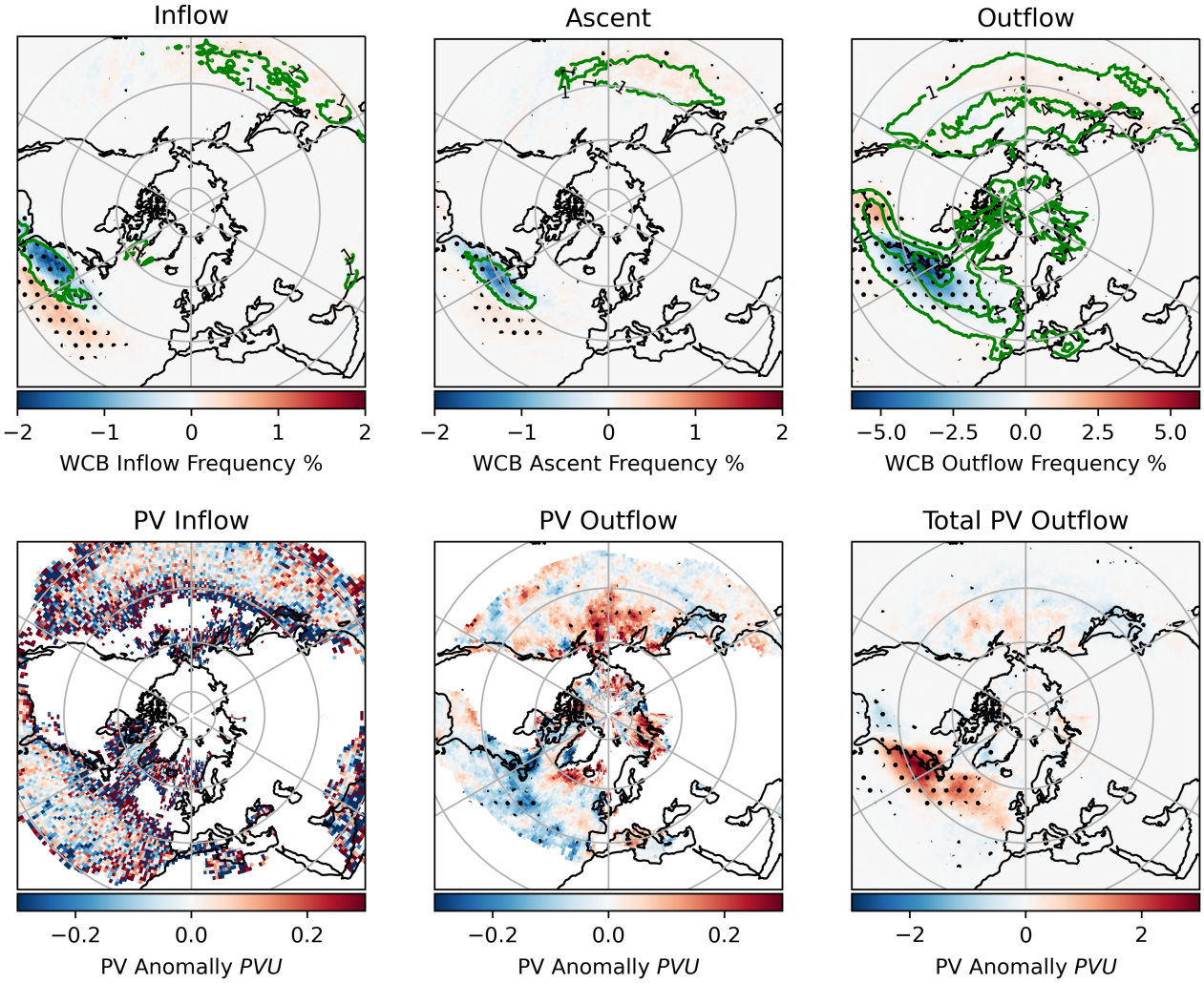


Figure 4.12: The difference between the NO_GS_SLHF and control runs for the WCB inflow (top left), ascent (top middle), outflow (top right), anomalous PV inflow (bottom left), anomalous PV outflow (bottom middle), and total anomalous PV outflow (bottom right). Green contours indicate the control values with contour intervals being 1%, 4%, and 9% respectively. Stippling indicates areas that exceed the 95% confidence interval.

Examining the transport from the atmospheric boundary layer to the upper troposphere, the difference in the WCB inflow, ascent, and outflow are shown in the top left, middle, and right panels of Figure 4.12 respectively. For all of these panels, there is a reduction in WCB activity over the North Atlantic where the most prominent activity is present in the control run, as shown by the green contours. The strength of this signal is almost as strong as the control

signal itself, indicating that the transport of boundary layer air over the North Atlantic to the upper troposphere is greatly reduced. Notably, there is a southward shift in the inflow and ascent regions due to the suppressed moisture flux over the GS, as well as an eastward shift to the Gulf of Mexico for the WCB outflow. In the North Pacific, there is a very weak but consistently positive anomaly of WCB activity, presumably due to the drier "two-basin particles'" ability to uptake moisture.

In order to infer the quality (quantity) of anomalous PV being transported via WCB, the anomalous PV fields are masked using the identified WCBs at both the inflow and outflow heights, and the average (sum) is taken. The bottom panels in Fig. 4.12 show the average anomalous PV in the WCB inflow (left) and outflow (middle) and the total anomalous PV in the WCB outflow for the entire forecast (right). While there is no discernible signal in the quality of the PV in the WCB inflow, there is a small but significant reduction (increase) of the average PV in the WCB outflow over the North Atlantic (North Pacific). While the PV at 850 hPa is anomalously lower at the inflow region (approximately 800 hPa) as seen in Fig. 4.11, this is not reflected in the PV inflow of the WCB. However, this signal is reflected when looking at the total PV inflow (not shown), although this is primarily reflecting the change in the WCB inflow signal seen in the top left panel of Fig. 4.12. Hence it is unclear whether changing the quality of the PV inflow would change the quality of the PV outflow as suggested by Methven (2015) and suspected from the comparable signals in PV at 850 hPa seen here in Fig. 4.11 (left panel) and the PV outflow seen in Fig. 4.12 (bottom middle panel). Finally, despite the fact that the PV in the outflow is more negative (bottom middle), the decrease in WCB outflow activity is more significant (top right). Consequently, there is an overall reduction in the net transport of anomalous PV to the upper troposphere, resulting in a decrease in blocking. Having fully examined this mechanism, we now compare the difference between model resolutions.

4.3.4 Dependence on Model Resolution

Firstly, Table 4.2 demonstrates a significant decrease in blocking frequency across all resolutions and initial dates for the entire NH when comparing the NO_GS_SLHF and control runs. The strength of this signal diminishes with decreased resolution, although this trend is primarily seen in winter, while the opposite trend is observed in summer. However, this pattern is less consistent within the first two weeks of the forecast, although Tco639 consistently exhibits the

most substantial change.

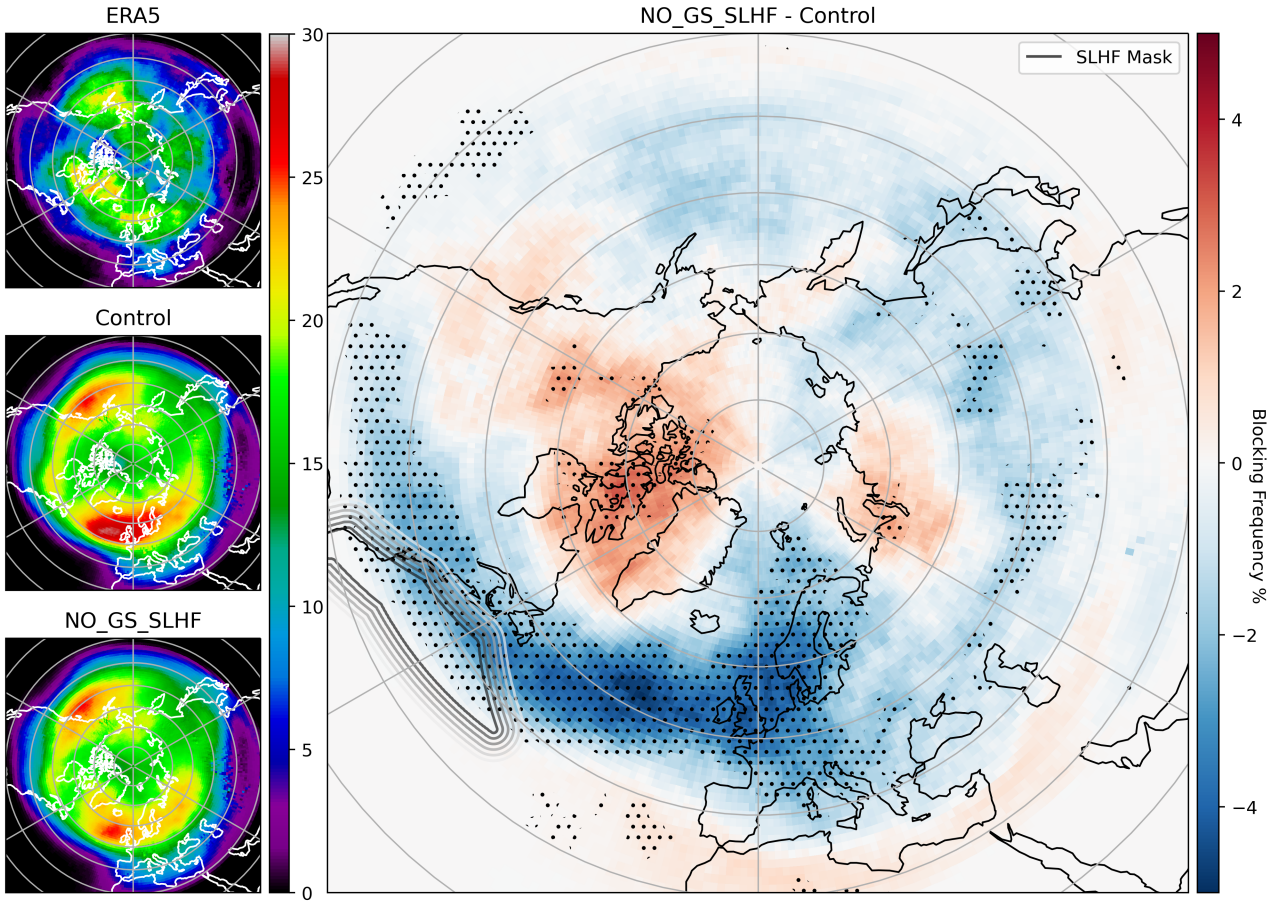


Figure 4.13: As in Fig. 4.1 but now at resolution **Tco319**.

Analysing the change in blocking frequency for lower resolutions (Fig. 4.13 and Fig. 4.14), we observe a smaller spatial signature in both lower resolution runs, with no propagation to the North Pacific. While the Tco199 run shows the largest spatial signature among the lower resolution runs, it has a considerably weaker magnitude. All resolutions show increased blocking over Northeastern Canada, shifting westward with lower resolution.

Fig. 4.15 depicts the percentage change in atmospheric blocking characteristics across resolutions, with saturated colour bars indicating significant results. This figure confirms that when GS SLHF is suppressed, blocks exhibit shorter duration, smaller size, and weaker intensity, though more individual blocks are detected. Notably, this signal is significant for all characteristics only at the highest resolution, Tco639.

Testing sensitivity to suppressed moisture fluxes between Tco639 and the two lower resolutions reveals no significant results, except for the block's average size, which is significant for both

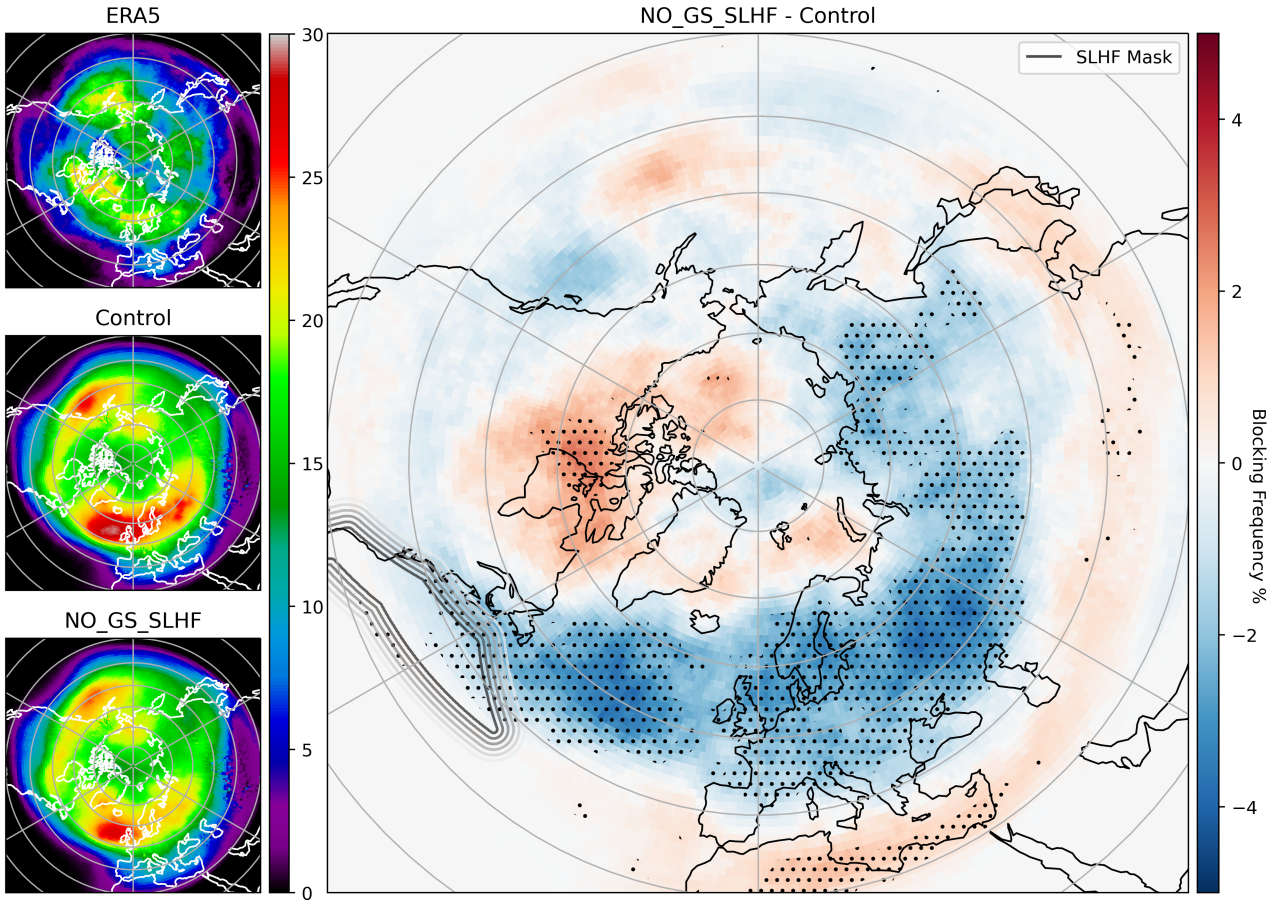


Figure 4.14: As in Fig. 4.1 but now at resolution **Tco199**.

resolutions. Tco199 exhibits a larger difference between the two runs compared to Tco319 in all characteristics, consistent with Table 4.2.

To assess the robustness of this result, different overlap and PV anomaly thresholds were tested. For Tco639, blocking intensity and average size were significant for all overlap values below 0.7 and 0.6 at PV thresholds of -1.2PVU and -1.3PVU, respectively. However, blocking duration and the number of blocks detected showed strongest significance between 0.4 to 0.5 overlap for both PV anomaly thresholds. This sensitivity likely arises from merging and splitting events, altering the block's life-cycle and the number of individual blocks detected (Hauser et al. 2023). The change in sign was consistent across all threshold values. While air-sea interactions are suspected to help maintain blocks, their effect on blocking duration is less robust than on blocking size and intensity. Testing lower resolutions across threshold values shows a noisier signal, with occasional significant signals for block intensity and average size, particularly in Tco199. Neither lower resolution run exhibits significant signals for duration or the number of individual blocks detected.

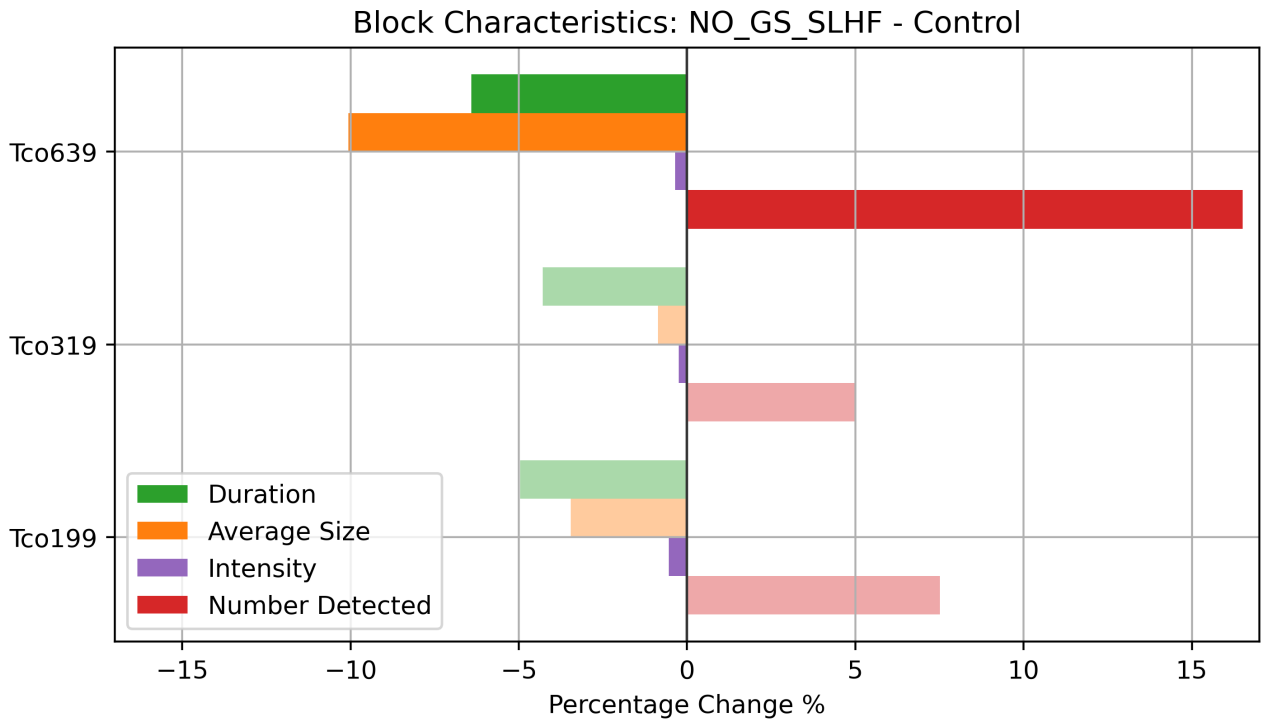


Figure 4.15: The percentage change in the block's characteristics for the NO_GS_SLHF run with respect to the control run verses resolution. The block's duration, average size, intensity, and the number of individual blocks detected per forecast are shown in green, orange, purple, and red, respectively. Fully saturated colours indicate changes over the 95% confidence level.

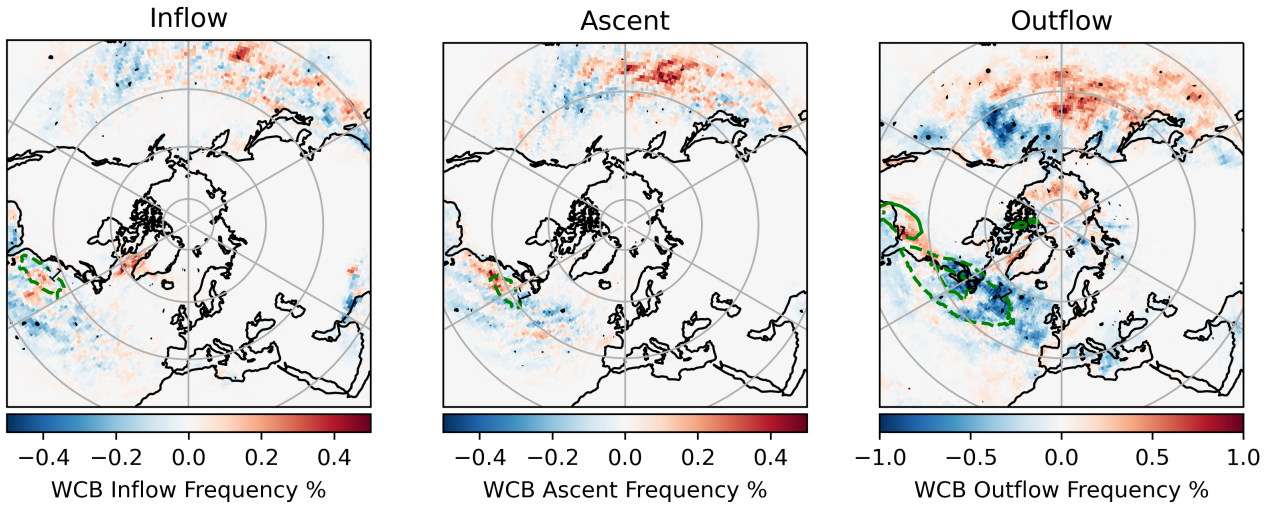


Figure 4.16: The difference between the WCB inflow (left), ascent (middle), and outflow (right) sensitivity of Tco639 and Tco199. Green contours show the difference between the NO_GS_SLHF and control runs for resolution Tco639 as shown in shading in Fig. 4.12, with dashed lines showing negative values.

Finally, Fig. 4.16 shows the difference between resolution Tco639 and Tco199's WCB sensitivity to suppressed GS moisture flux. For the WCB inflow (left) and ascent (middle), there is effectively no significant signal; however, for the WCB outflow (right), there is some, although

patchy, significant signal seen. This shows that the decrease in WCB outflow due to GS moisture flux suppression is strongest at Tco639, where there is already a reduction of WCB activity over the North Atlantic at this resolution, as indicated by the dashed green contour. Additionally, there is increased sensitivity outflow activity in the North Pacific at Tco639 compared to Tco199, which again correlates with the increased WCB out activity over the North Pacific as a result of suppressed GS moisture flux. While this signal is very weak, it suggests that with more reforecasts and ensemble members, perhaps a clearer, stronger signal would emerge showing that WCB's sensitivity to moisture fluxes is dependent on resolution.

4.4 Conclusions

In this study, the impact of suppressing Gulf Stream SLHF on atmospheric blocking was analysed using a coupled ensemble reforecast on the ECMWF IFS. When this air-sea interaction was suppressed:

1. Atmospheric blocking frequency reduced over the majority of the Northern Hemisphere by up to 30%.

2. The duration, average size, and intensity of atmospheric blocks decreased by approximately 6.4%, 10.1%, and 0.35%, respectively. Additionally, a 16.5% increase in the number of individual blocks detected per forecast was observed.

3. Faster eastward-propagating Rossby waves with larger zonal wave numbers were evident.

4. WCB activity dropped significantly, transporting less anomalously low PV air to the block.

5. Resolutions lower than Tco639 ($\sim$18km) exhibited a weaker, non-significant change in block duration, average size, and the number of individual blocks detected. However, a reduction in blocking frequency and intensity was seen across all resolutions.

We have investigated the effects of air-sea interactions, specifically the influence of the Gulf Stream's GS, on atmospheric blocking. This experiment highlights the significant role that air-sea interactions play in modulating the strength of atmospheric blocks and their potential

impacts, both locally and remotely. The underlying mechanisms of this process are beginning to be understood. A theory proposed by Mathews & Czaja (2024) suggests that air-sea interactions may diabatically influence boundary layer air, which is subsequently transported to the block via warm conveyor belts, altering the quality and quantity of its negative PV anomalies. While some of these hypotheses have been tested and confirmed, ultimately, a Lagrangian analysis is needed to fully confirm these results, particularly the change in the PV from inflow to outflow, accounting for all the effects of latitudinal change, outflow pressure, inflow moisture, etc. (Heitmann 2023, Fig. 5.9).

Chapter 5

A Heuristic Model for the Oceanic Pathway to Atmospheric Blocking

5.1 Introduction and Motivation

Having linked the Gulf Stream (GS) to atmospheric blocking in the North Atlantic (NA) and theorising the ocean's potential pathway to atmospheric blocks in Chapter 3 (Mathews & Czaja 2024), and then testing and confirming these hypotheses on the ECMWF's state-of-the-art high-resolution integrated forecasting system in Chapter 4 (Mathews et al. 2024), there is now scope to explore this mechanism from a dynamical systems perspective. Given the inherent complexity and uncertainty of both real-world data and high-resolution model output, this approach will allow for the distillation of the oceanic pathway to atmospheric blocking into its essential parts, removing any interfering mechanisms that may act to enhance or dampen the effects of this pathway, giving a qualitative and causal relationships between these domains.

Since the work of Lorenz (1963), simple heuristic models have been an important tool for theoretical understanding, used to investigate weather phenomena such as the North Atlantic Oscillation (NAO) (Molteni & Kucharski 2019), storm track activity (Ambaum & Novak 2014, Novak et al. 2017), and the life cycle of atmospheric blocks (Nakamura & Huang 2018). These approaches, although extremely idealised, allow for the examination of a single physical process by removing any additional physics present in the real world, while also demanding very little computational power. Additionally, the possibility of modifying parameters in these simple systems, which could relate to a change in scale, seasonality, or the relative importance of feedback processes, and exploring their bifurcations, allows for a qualitative argument to be

made while also retaining a clear line of causality. For example, Lorenz (1984) showed that with increasing asymmetric thermal forcing, his three-variable global circulation model (GCM) bifurcates from a single steady fixed point to a stable limit cycle, i.e., a supercritical Hopf bifurcation (Strogatz 2018). The three resulting fixed points from this bifurcation correspond to a zonal, transient, and blocked regime. Further increasing the asymmetric forcing leads to chaotic behaviour, with an increasing Lyapunov exponent indicating less predictability (Wang et al. 2014). This has implications for both the irregularity of the atmosphere and the high-resolution GCMs designed to forecast it, and could even be compared to the asymmetric heating of the atmosphere by the GS and other western boundary currents (WBCs).

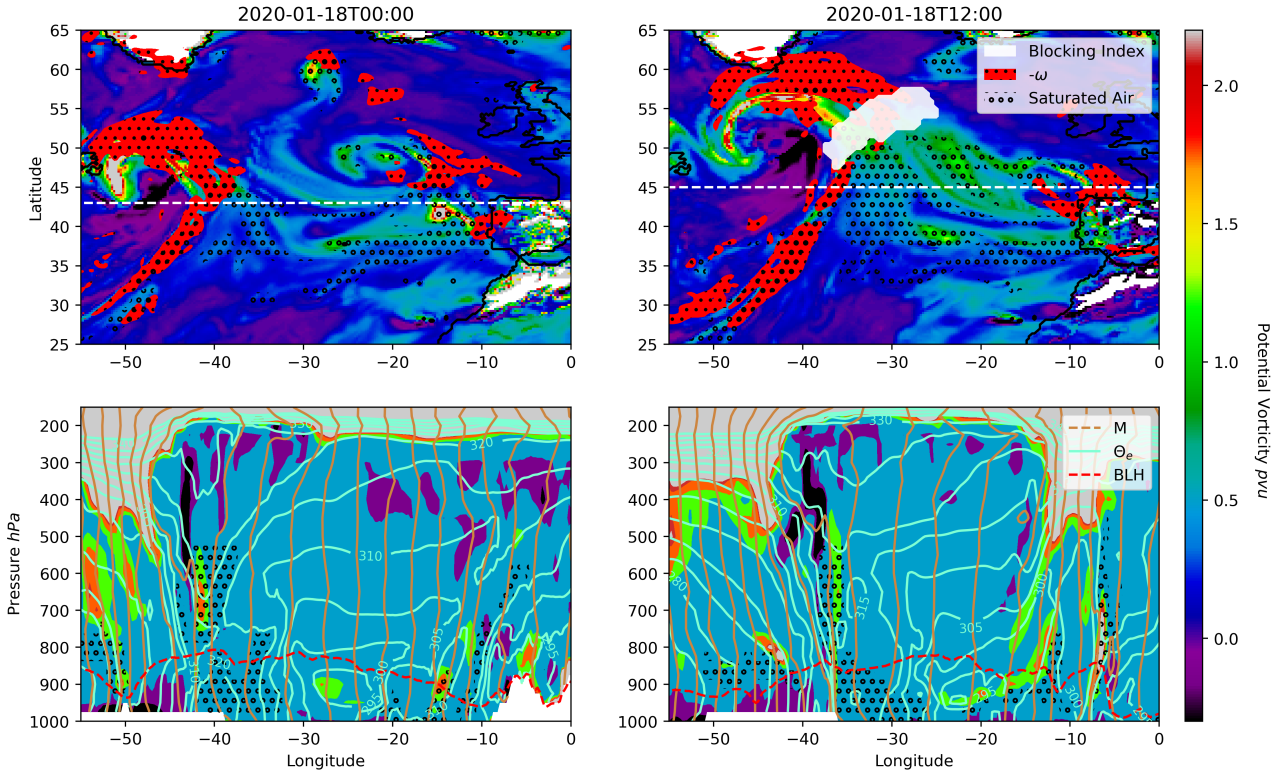


Figure 5.1: The average PV between 900-975 hPa (top) and a PV zonal section (bottom) (in PVU, 1 PVU = 10^{-6} Km^2 s^{-1} kg^{-1}) for a blocking event starting on January 18th, 2020. The white dashed line in the top panels indicates the position of the section used in the bottom panels. The red stippled contour shows upward velocities at 500 hPa where $\omega < -1$ Pa s^{-1}, while the hollow stippling shows air that has a relative humidity above 90% at 975 hPa. The brown, light blue, and red lines in the bottom panels show surfaces of constant momentum, equivalent potential temperature, and the height of the atmospheric boundary layer, respectively.

In order to motivate a simple model describing the oceanic pathway to atmospheric blocking, we shall reexamine the case study seen earlier in Fig. 3.1. Here, Fig. 5.1 shows the same induction of a blocking event starting on the 18th of January 2020, although now air that is approximately saturated (relative humidity is greater than 90%) is indicated by hollow stippling.

The top panels show moist air pooling behind a decaying cyclone and moving towards the warm sector of an incoming cyclone, as primarily documented in the moist handover mechanism from Papritz et al. (2021). This saturated air leaves the atmospheric boundary layer, ascending along the WCB of the cyclone as indicated by the red stippled contour in the top panels indicating upward transport at 500 hPa, and is deposited in the upper troposphere, generating the negative PV anomaly that forms the atmospheric block. The transport of this anomalously low PV air from the GS region to the block via the moist handover mechanism has been observed by Wenta et al. (2024), while the PV modification of the boundary layer air and moisture supply due to air-sea heat fluxes was observed in Chapter 3 by Mathews & Czaja (2024).

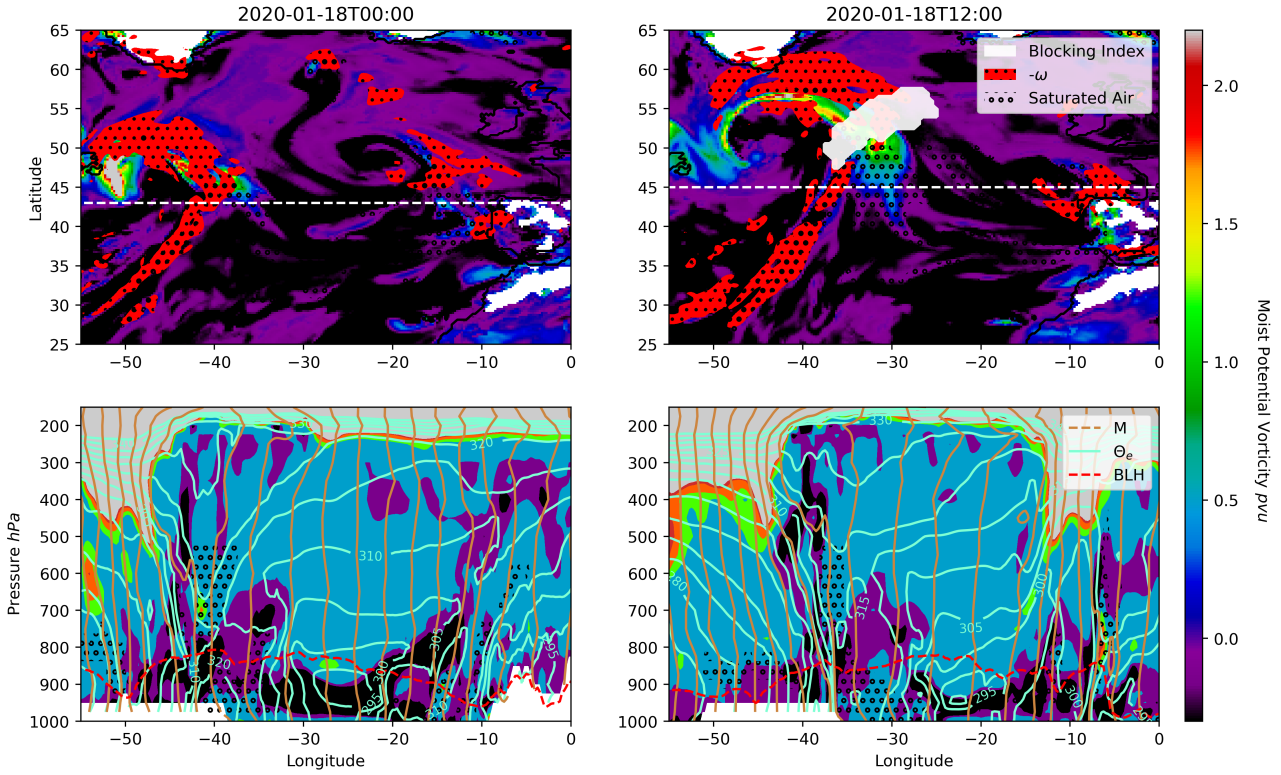


Figure 5.2: As in Fig. 5.1 but for moist PV.

While it is understood how the ocean can modify the boundary layer air through heat fluxes, initiated by cold air outbreaks (CAOs) and sustained by surplus oceanic heat content, how the ocean affects air transport from the boundary layer to the upper troposphere has yet to be thoroughly investigated. Although Sheldon et al. (2017) showed that the rate and quantity of air transported along the WCB depends on both the absolute and the gradient of the sea surface temperatures (SSTs), it is still unclear what explicitly determines the strength of transport from the boundary layer to the upper troposphere. For this, we turn to the work of Bennetts & Hoskins (1979), who theorised that an air parcel is conditionally symmetrically unstable if its

wet bulb (or moist) PV is negative. Additionally, Emanuel (1983) showed that when the slope of surfaces of constant absolute momentum is less than that of surfaces of constant equivalent potential temperature, the air parcel will undergo slantwise convection, with the strength of that instability being primarily dependent on the vertical shear of the meridional wind. For fully saturated air, conditions for slantwise instability and conditional symmetric instability can be seen in the bottom panels of Fig. 5.2 at approximately -40E by the brown and light blue contours and by the black and purple shading, respectively.

In this study, we derive and explore a simple three-box model that describes the oceanic pathway to atmospheric blocking and ask the questions: to what degree can the ocean predict atmospheric blocks, and how does this depend on certain feedback processes? This chapter is laid out as follows: Section 5.2 describes the three-box blocking model. Section 5.3 describes the diagnostic methods used to analyse the model. The results are shown in Section 5.4, with the fixed ocean model and the fully coupled model being examined in Sections 5.4.1 and 5.4.2, respectively. Finally, the model is discussed in Section 5.5, and the conclusions are given in Section 5.6.

5.2 The Model

The model used in this study is a three-box model, as shown in Fig. 5.3, where the ocean (bottom box) is coupled to a fully saturated atmospheric boundary layer (middle box) via heat fluxes, as illustrated by the orange arrow F, and the boundary layer is connected to the upper troposphere (top box) via convection, as illustrated by the green arrow σ. Air is also allowed to flow through the boundary layer box at a background speed u, as illustrated by the blue arrow. To derive the equations of motion for this model, the principles of mass conservation, energy conservation, and (moist) PV conservation are applied. The use of Cauchy's mean value theorem, seen in Equation A.5, allows for the elimination of either the boundary layer moist PV or the equivalent potential temperature equation of motion due to the approximation $\frac{\partial \theta_{BL}}{\partial z} \approx -\frac{\theta_{BL}}{h_{BL}}$, where θ_{BL} is the average boundary layer equivalent potential temperature. As the relative humidity exceeds 90% for the WCB inflow in the boundary layer, as seen in Fig. 5.1 and 5.2, this air mass is close to saturation. Consequently, the angle between moist and dry isentropes is negligible, making the diabatic generation and conservation of moist PV approximately equivalent to "dry" PV (Bennetts & Hoskins 1979, Equation 20, the first term

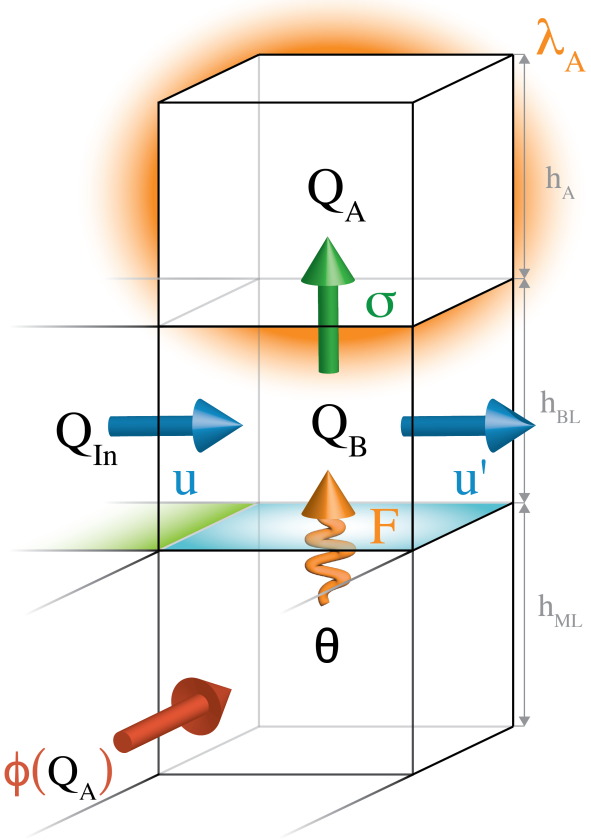


Figure 5.3: Schematic of the three-box blocking model. The bottom box represents the average ocean temperature θ in the oceanic mixed layer, the middle box is the average boundary layer moist PV Q_B, and the top box is the average upper troposphere PV Q_A. The height of each box is denoted by h. The ocean is connected to the atmospheric boundary layer via heat fluxes F, indicated by the orange arrow. The atmospheric boundary layer is then connected to the upper box via convection σ, represented by the green arrow. The upper-level PV anomaly decays according to λ_A, depicted by the orange hue. Air is allowed to flow through the boundary layer u, indicated by the blue arrow, with the inflow of new PV into the boundary layer box is denoted by Q_{In}, while the inflow of heat into the oceanic mixed layer is represented by ϕ.

on the right-hand side (rhs)). Additionally, assuming moist-adiabatic transport to the upper troposphere, as discussed in Section 3.3.3, the inflow of moist PV in the WCB is approximately equal to the outflow. This outflow is no longer saturated as any moisture contained in the air parcel has been used to cross dry isentropes, and hence, the moist PV is approximately equivalent to the "dry" PV in the upper troposphere. In short, we are assuming the inflow of PV is approximately equal to the outflow, as also theorised by Methven (2015). The non-dimensionalised equations of motion for this model are derived in Appendix B and are given by:

$$\dot{\theta} = -c\kappa(\theta + Q_B) + \gamma Q_A, \tag{5.1}$$

$$\dot{Q}_B = -\kappa(\theta + Q_B) + Q_{In} - Q_B, \tag{5.2}$$

$$\dot{Q}_A = \lambda_A(1 - Q_A) + \sigma(Q_B)Q_B. \tag{5.3}$$

Here, the independent variable t represents time, the non-dimensional variables $\theta(t)$, $Q_B(t)$, and $Q_A(t)$ are the average ocean temperature, atmospheric boundary layer moist PV, and upper troposphere PV within their respective boxes, and $\sigma(Q_B)$ is the convection parameterisation. The first terms on the rhs relate to the diabatic sources and sinks of both heat and PV, notably the bulk formula from Bjerknes (1964) for Equations 5.1 and 5.2, and some relaxation to climatology for Equation 5.3. The second terms on the rhs relate to the advection of the substance in and out of the domain, with the red, blue, and green arrows in Fig. 5.3 depicting Ekman transport, through advection and convection respectively for Equations 5.1, 5.2, and 5.3. For simplicity, $Q_{In} = 0$. The control parameters are κ, which is the strength of the air-sea coupling, c, the ratio of the heat capacities of the atmospheric boundary layer to the oceanic mixed layer, γ, the wind stress feedback for Ekman transport from the large-scale flow to the oceanic transport, and λ_A, the decay timescales of the large-scale atmospheric flow.

The convection scheme is based on Bennetts & Hoskins (1979) and is parameterised by:

$$\sigma(Q_B) = \begin{cases} \sigma_0\sqrt{-Q_B}, & \text{if } Q_B \leq 0 \\ 0, & \text{otherwise} \end{cases} \tag{5.4}$$

where σ_0 is the convective timescale. This parameterisation is depicted by the green line in Fig. 5.4. It arises from gravitational instability when a parcel of air is perturbed from its background state. The rate of instability depends on the buoyancy frequency:

$$N = \sqrt{\frac{g}{\theta_0}\frac{\partial\theta_{BL}}{\partial z}}, \tag{5.5}$$

where g is the acceleration due to gravity, and θ_0 is some reference temperature. Assuming that the horizontal temperature gradients are small compared to the vertical gradients—which is a reasonable approximation given the large domain over the Gulf Stream extension—then $Q_B \propto N^2$. As described by Bennetts & Hoskins (1979), when this air becomes destabilised, the solutions to the equation of motion of this perturbed air parcel result in exponential growth. However, when the buoyancy frequency is real, the air parcel oscillates around it's original position. Hence, convection occurs only when $\frac{\partial \theta_{BL}}{\partial z} < 0$, which, in a vertically stratified fluid, is equivalent to $Q_B < 0$. This criterion for convection is evident from the upward motion at 500 hPa, illustrated by the red stippled contour in the upper panels of Fig. 5.2, and the negative moist PV shown by the purple and black shading in the bottom panels at 500 hPa.

The non-dimensional time unit is $t_0 = \frac{L}{U}$, which is of the order $O(10^5\text{s})$, i.e., approximately a day. Hence, the control parameter $\lambda_A = 0.2$, indicating that the large-scale flow has timescales of five days. Convection is $\sigma_0 = t_0 \frac{\rho_{BL} h_{BL} V_B}{\rho_A h_A V_A} \sqrt{\frac{g}{h_{BL}}} \approx O(10^2)$ and will be set to 535 unless otherwise specified. Additionally, control parameters are set to $\kappa = 11$, $c = 0.006$ and $\gamma = 0.2$, which approximately resemble the real-world coupling for the boxes in Fig. 5.3.

5.3 Method

The model is integrated forward using the Runge-Kutta formula of order 5 (Dormand & Prince 1980) with a time step of $dt = 0.00001$. Although coarser time steps can be used to integrate the system, the convection scheme seen in Equation 5.4 is not smooth, requiring a high temporal resolution to accurately capture the position of the trajectory.

The largest Lyapunov exponent is computed following Kuptsov & Parlitz (2012). When a trajectory along an attractor is perturbed by some infinitesimal amount $\delta \boldsymbol{x}$, the rate of growth of that perturbation from its original trajectory is given by:

$$\dot{\delta \boldsymbol{x}} = \boldsymbol{J} \delta \boldsymbol{x} \tag{5.6}$$

where $\boldsymbol{J}$ is the Jacobian matrix. By propagating a set of random orthonormal vectors according to Equation 5.6 along the attractor, and regularly re-orthonormalising these vectors (referred to as Gram-Schmidt orthonormalisation), the averaged effect across the whole attractor results in

the Lyapunov vectors. These vectors determine the direction of growth (decay) and magnitude of that growth (decay), given that the vectors are larger (less) than unity.

The bifurcation diagrams are calculated by first integrating the model for an appropriate amount of time so that the trajectory is appropriately close to the attractor. Then the trajectory is integrated along the attractor, and the local extrema are found and saved. The bifurcation parameter is then adjusted, and the process is repeated.

The instantaneous dimension and persistence are calculated following Faranda et al. (2017). The probability that, given some state $\boldsymbol{\zeta}$ along the attractor, the trajectory returns to that state is given by a generalized Pareto distribution. The instantaneous dimension is extracted through the shape parameter of the distribution, which is equal to the inverse of the dimension for state $\boldsymbol{\zeta}$. This process is repeated for all states along the attractor to find its instantaneous dimension for the entire attractor. The instantaneous persistence is determined by introducing the extrema index in the generalized Pareto distribution. This index ranges between 0 and 1, corresponding to complete stability or transitivity, respectively. The instantaneous persistence is the inverse of this extrema index.

5.4 Results

5.4.1 Fixed Ocean Model

For the results in this section, the ocean is assumed to be at a fixed temperature, akin to an infinite heat reservoir. Consequently, the model simplifies to a two-box model with a prescribed ocean, meaning that Equation 5.1 is ignored. Hence the equations of motion for the fixed ocean model are:

$$\dot{Q}_B = -\kappa(\theta_o + Q_B) - Q_B \tag{5.7}$$

$$\dot{Q}_A = -\lambda_A(Q_A - 1) + \sigma(Q_B)Q_B \tag{5.8}$$

where θ_o is the set temperature of the ocean. The first term on the rhs of both equations describe the diabatic effects on the PV, followed by the effects of advection with the second

term. The behaviour of the boundary layer's equation of motion, Equation 5.7, will be examined first. Due to the approximation using Cauchy's mean value theorem mentioned in Section 5.2 and shown in Equation A.5, $Q_B \propto -\theta_{BL}$. Since $\kappa > 0$, PV is therefore destroyed when the ocean is warmer than the atmospheric boundary layer, or equivalently, when $\theta_o > -Q_B$. PV is then generated in the opposite case. This is in agreement with the observations of Vannière et al. (2016) showing the generation of negative PV through the destabilisation of the boundary layer in the cold sector of a cyclone. Therefore, the boundary layer PV decays exponentially to minimise the difference between the boundary layer temperature and the oceanic temperature, while also being balanced by the advection of any anomalous PV out of the boundary layer. Whether this stability is dominated by heat flux or advection depends on whether $\kappa \gg 1$ or $\kappa \ll 1$, respectively.

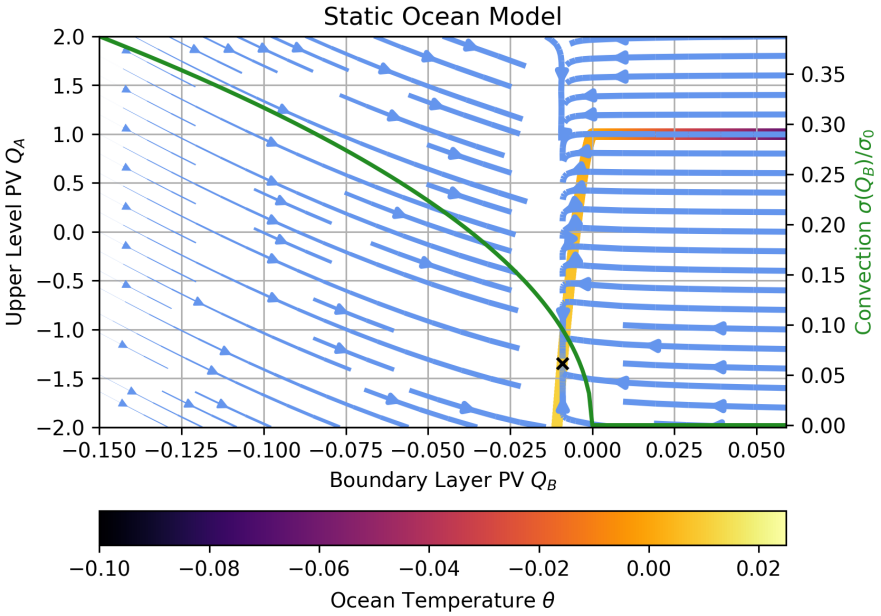


Figure 5.4: A stream plot showing the trajectory of the equations of motion given a fixed ocean temperature of $\theta_o = 0.01$, $\sigma_0 = 535$, $\kappa = 11$, and $\lambda_A = 0.2$. The black cross denotes the fixed point of the system, with the colour gradient line depicting the variations of the fixed point with ocean temperatures. The green line shows the convection parameterisation.

The equation of motion for the upper troposphere, Equation 5.8, shows that the diabatic effects on the upper troposphere act only to return the upper tropospheric PV to some background value. This process could be interpreted as long wave radiative cooling (Harvey et al. 2020), or alternatively the advection of anomalous air out of the upper-level box while climatological air is advected in, or some other process. The tendency towards climatology is offset by the injection of boundary layer PV. This only occurs when the boundary layer PV is negative,

triggering convection as described by Equation 5.4 and shown with the green line in Fig. 5.4.

The combination of these motions can be seen in the stream plot shown in Fig. 5.4, with $\theta_o = 0.01$, $\sigma_0 = 535$, $\kappa = 11$, and $\lambda_A = 0.2$. The blue lines show the direction of motion throughout phase space, with the thinness of the lines indicating the speed, and the fixed point for this model configuration shown by the black cross. This figure shows that while the boundary layer PV is strictly positive, the upper-level PV moves towards its climatological value of 1. However, once the boundary layer PV is negative, the upper-level PV is now affected by convection and balances the inflow of negative PV with its tendency towards climatology. Meanwhile, the boundary layer air always attempts to minimise the difference between its temperature and the temperature of the ocean, while also being simultaneously pulled towards climatology.

Considering the steady-state solutions of the equations of motion, Equations 5.7 and 5.8, it can be easily shown that the fixed points for this system are $Q_B^* = -\frac{\kappa}{1+\kappa}\theta_o$ and $Q_A^* = 1+\frac{\sigma_0 Q_B^*}{\lambda_A}\sigma(Q_B^*)$, as shown by the thick coloured line in Fig. 5.4. From this plot, it is obvious that while $\theta_o < 0$, the upper troposphere always tends towards its climatology. However, once the ocean is anomalously hot, negative PV is generated in the boundary layer, and there exists a balance between the convective influences and relaxation to climatology. With strong enough positive oceanic temperature anomalies, negative PV is maintained in the upper troposphere, which, as measured by Schwierz et al. (2004), is defined as an atmospheric block. The eigenvalues for this system are $\lambda = -\kappa - 1, -\lambda_A$ for all oceanic temperatures, and hence this model is globally stable. Given that this model only has two dimensions, growth, decay, or oscillations are the only types of motion possible, and hence progressing to the fully coupled model will allow for more interesting behaviour.

5.4.2 Coupled Model

Including a fully dynamic ocean, as detailed in Equations 5.1 - 5.3, transforms the system from one with only a stable fixed point to an oscillating system. Fig. 5.5 shows the time series of the system for $\sigma_0 = 535$, $\kappa = 11$, $c = 0.006$, $\gamma = 0.2$, and $\lambda_A = 0.2$, with the upper-level and boundary layer PV shown in green and purple, respectively, while the oceanic mixed layer temperature is shown in orange. Notably, this figure shows a local maximum in ocean heat content occurring just before a local minimum of boundary layer PV, followed by a minimum in

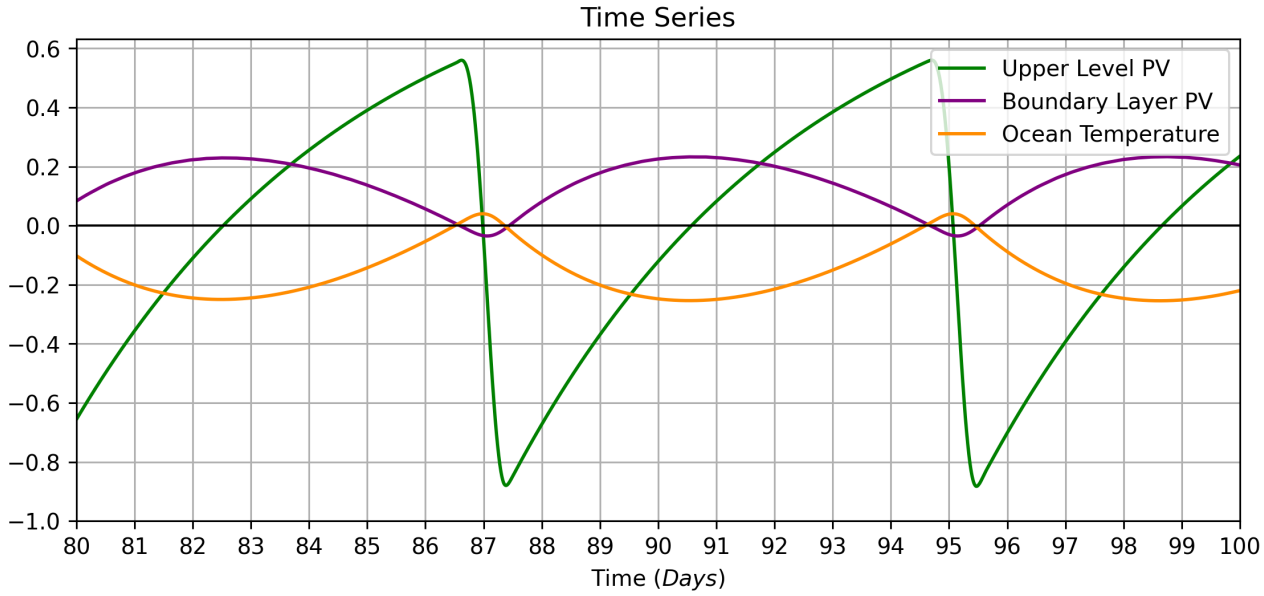


Figure 5.5: Variations of the upper-level PV Q_A, the boundary layer PV Q_B, and the ocean temperature θ over a 20-day period are denoted in green, purple, and orange, respectively, with parameters $\sigma_0 = 535$, $\kappa = 11$, $c = 0.006$, $\gamma = 0.2$, and $\lambda_A = 0.2$.

upper-level PV roughly half a day later, indicating an atmospheric block. This is then followed by a minimum ocean temperature while the block decays and the upper level PV approaches climatology. This sequence is one that has been observed in Chapter 3, notably in Fig. 3.7.

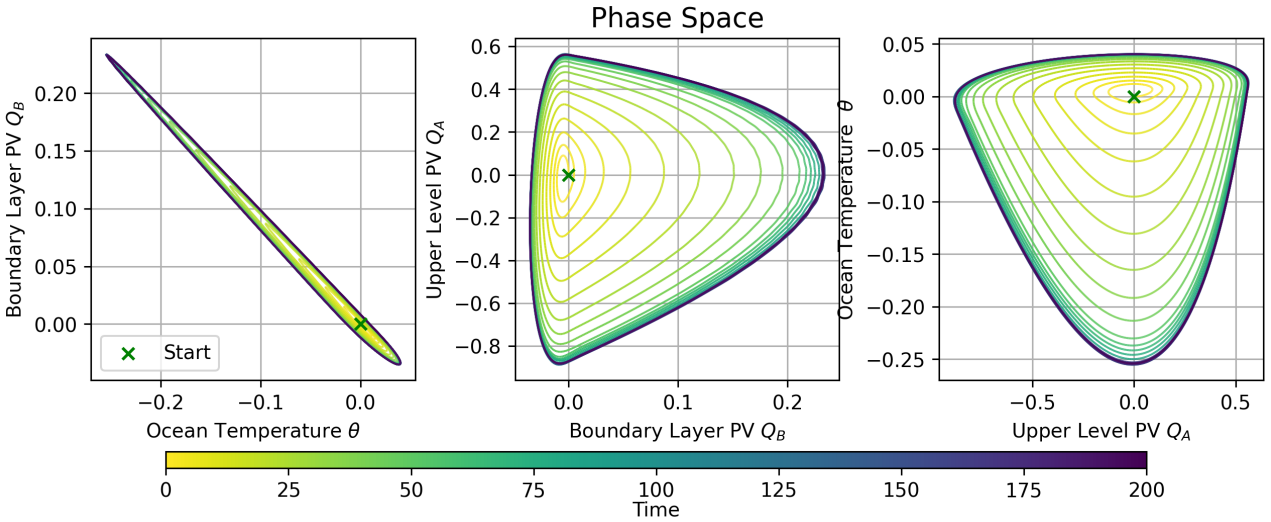


Figure 5.6: Phase plot of the trajectory with parameters $\sigma_0 = 535$, $\kappa = 11$, $c = 0.006$, $\gamma = 0.2$, and $\lambda_A = 0.2$. The colours along the trajectory denote the time since its initialisation, as denoted by the green cross.

Fig. 5.6 shows the trajectory in phase space, starting from the origin and spiraling outward clockwise (counter clockwise) towards an attractor in the left (middle and right) panels. While

there is no clear relationship seen between the upper-level PV and the variables in the lower domain other than the direction of orbit, there is a strong linear relationship seen between the ocean temperature and the boundary layer PV, with more negative PV coinciding with warmer oceans and vice versa. This correlation was again seen during the observational analysis in Section 3.3.1. From these two results, it is clear that this model approximately mimics the mechanism it aims to represent.

The period of oscillation between a zonal and blocked state is approximately 10 days, which again is reminiscent of the regime timescales in the atmosphere. Looking at the magnitude of these oscillations, the normalisation factor is $Q_0 = 2$ PVU, and therefore the PV magnitudes are reminiscent of the real world. However, for the ocean temperature, the normalisation factor is $O(10^2\text{K})$, and hence the change in ocean temperature is $O(10^1\text{K})$, which is somewhat large. Reducing the convection parameter σ_0 will reduce the amplitude of this oscillation to one that is more appropriate for this interaction, although it loses some interesting behaviour which will be discussed in Section 5.4.2.

Fig. 5.7 shows consecutive extrema plotted against each other, with the bottom axis showing the leading extrema and the vertical axis showing the succeeding one. From left to right, bottom to top shows the maximum ocean temperature and the minimum boundary layer and upper-level PV. Focusing on the left orange column, it is clear that there is a strong negative linear relationship between maximum ocean temperature and the succeeding minimum PV in both the boundary layer and upper levels (left middle and top panels respectively), although this is notably stronger for the boundary layer PV. Additionally, there is a positive linear relationship between the boundary layer PV and the succeeding upper-level PV minimums (top middle panel). The relationship between the remaining extremes is far weaker, indicating that the direction of causality is primarily from the lower domain to the upper domain. The Lorenz maps (the diagonal panels) show a somewhat noisy relationship compared to the clear relationship seen in most continuous models (Lorenz 1963). This is presumably due to the non-smooth nature of the convection parameterisation used in Equation 5.4.

Finally, we examine the local dimension and persistence of the attractor, as shown by the three-dimensional phase portrait in Fig. 5.8 (left and right panels respectively). Starting with the local dimension, it is seen that the region with the overall lowest dimension is when convection is triggered, i.e., from the maximum upper-level PV to the maximum ocean heat content followed

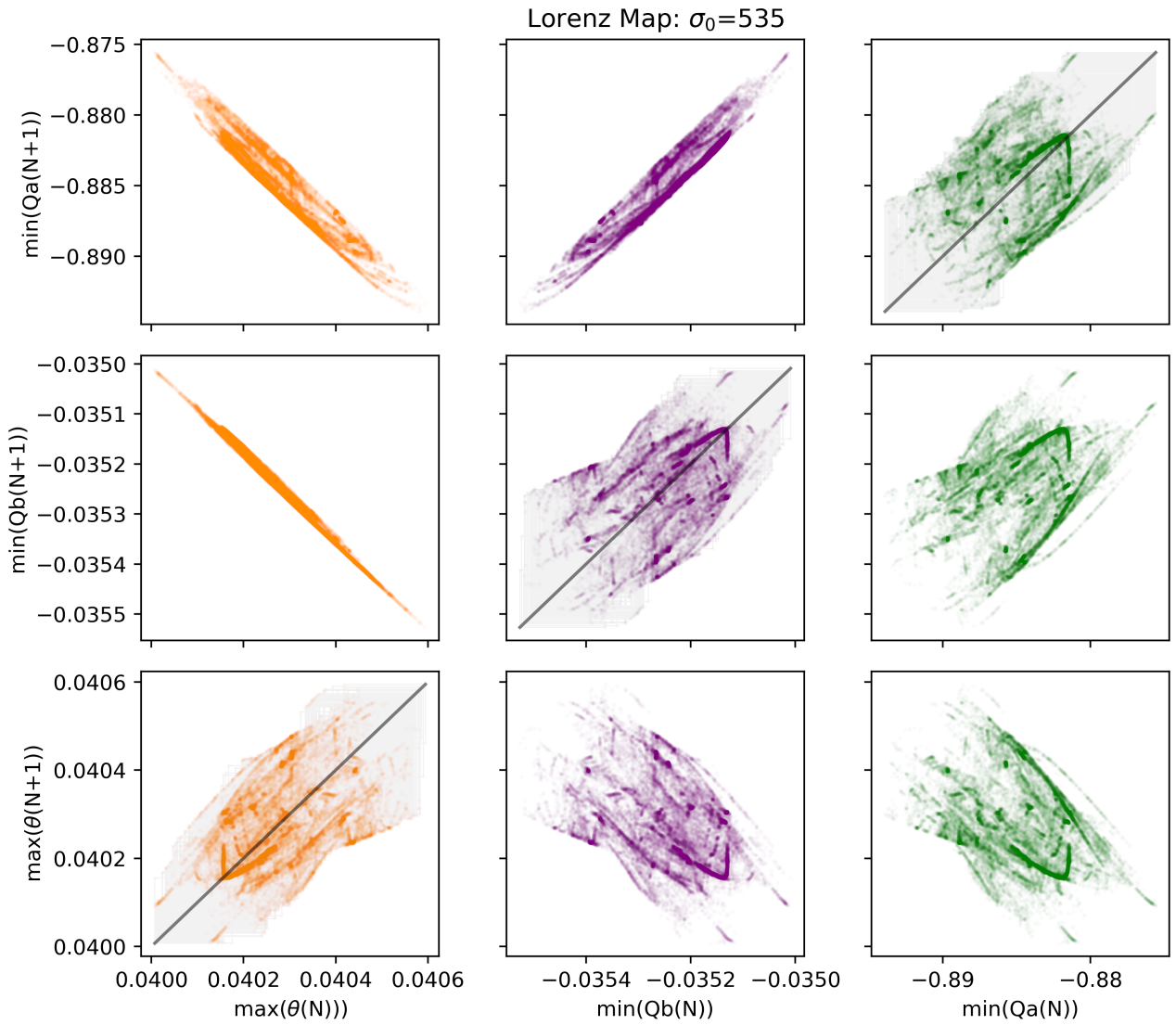
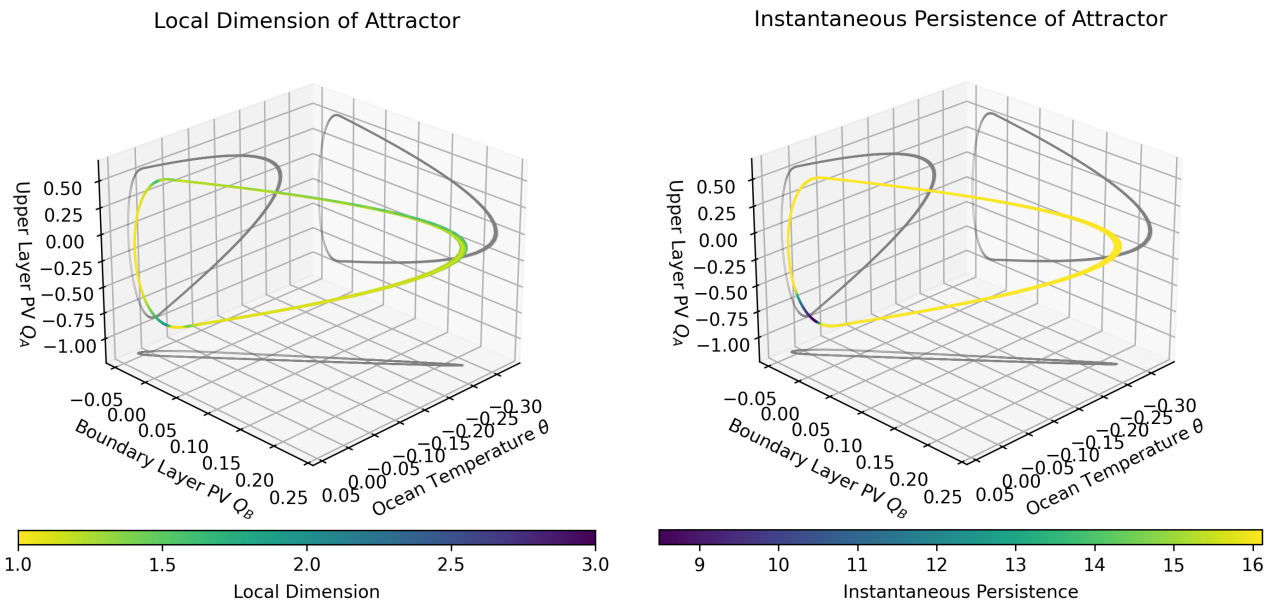


Figure 5.7: Lorenz map showing consecutive extrema for all variables. When θ, Q_B, or Q_A leads, the plot is in orange, purple, or green, respectively. Parameters are set to $\sigma_0 = 535$, $\kappa = 11$, $c = 0.006$, $\gamma = 0.2$, and $\lambda_A = 0.2$

by the minimum upper-level PV. While the local dimension is relatively high just before the minimum upper-level PV suggestive of reduced predictability beyond this region, this coincides with a region of low persistence, and hence transient behaviour. Therefore, this convective stage does not exists in a region where nearby trajectories diverge for long and hence there is still some predictability after this region, as seen by the Lorenz maps in Fig. 5.7. At the peak of the block, there is both a low dimension and high persistence, a feature also seen in both the negative phase of the NAO (Faranda et al. 2017) and heatwaves associated with blocking patterns (Holmberg et al. 2023).

After the peak of the block, the trajectory moved through a region of high persistence and



(a) Instantaneous dimension

(b) Instantaneous persistence

Figure 5.8: Phase plot of the three-box model with the instantaneous dimension (left) and persistence (right) shown in colour. Parameters were set to $\sigma_0 = 535$, $\kappa = 11$, $c = 0.006$, $\gamma = 0.2$, and $\lambda_A = 0.2$.

moderately high local dimension, meaning that it spends a significant amount of time in a region where nearby trajectories diverge, and hence there is less predictability from the block to the lower domain as seen in Fig. 5.7. In the region of the attractor where the ocean temperature is at minimum, it is seen that the edges of this attractor have the highest dimension, suggesting that more anomalous values lead to less predictability. We now continue to explore the predictability of this model, but seeing how that varies with the control parameters.

Bifurcation and Predictability

In order to find the fixed points of the system, one must find a solution to the equation:

$$i\sigma_0 \left(\frac{\gamma Q_A}{c(\kappa + 2)} \right)^{3/2} = \lambda_A (Q_A - 1). \tag{5.9}$$

Solutions to this equation have only one real fixed point. Fig. 5.9 shows this fixed point with changes in convection strength. When convection is off, the upper-level PV decays to background values, $Q_A^* = 1$. However, once it is increased, the stable fixed point moves towards zero. Further increasing this parameter results in a Hopf bifurcation, with the stable spiral in phase space (not shown) now transforming into a stable limit cycle, seen in Fig. 5.6, with an

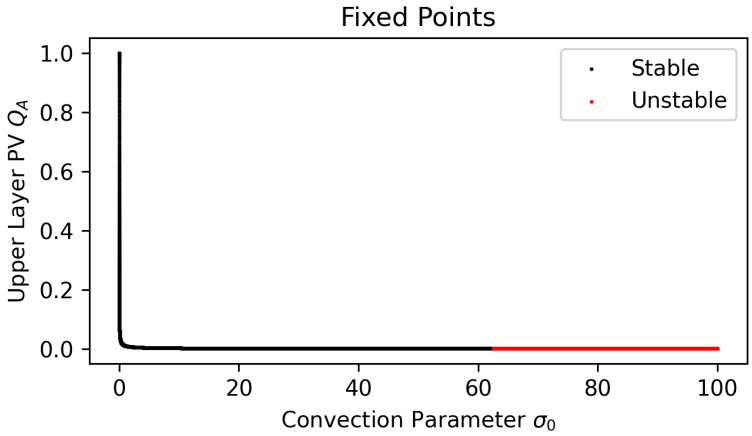


Figure 5.9: Fixed points of the three-box model with variations in the convection strength σ_0. Black and red points show stable and unstable fixed points respectively. Parameters are set to $\sigma_0 = 535$, $\kappa = 11$, $c = 0.006$, $\gamma = 0.2$, and $\lambda_A = 0.2$.

unstable fixed point located at $Q_A^* \approx 0$. This occurs at $\sigma_{Hopf} \approx 62.5$ for these particular chosen parameter values.

The modification of the remaining parameters provides qualitative insight into their role in this model. Fig. 5.10 shows the change in both the average difference in successive extrema and the period of oscillation with a changing parameter. Focusing first on the change in control parameter $c = \frac{\rho_{BL} c_p h_{BL}}{\rho_o c_o h_{ML}}$, shown in the first panel of Fig. 5.10, this represents the ratio of the heat capacity of the atmospheric boundary layer versus that of the oceanic mixed layer. This parameter nicely encapsulates seasonality as the ocean's mixed layer is deepest during winter and shallowest during summer (Kraus & Turner 1967), and hence higher (lower) values of c represent summer (winter) air-sea interactions. When this parameter is increased, both the period of oscillation and the successive difference in extrema decrease. This suggests that the ocean has more thermal inertia in the winter, giving it more influence to steer the atmosphere than in summer (Bjerknes 1964). Additionally, if there were no difference between the heat capacities, i.e. $c/c_0 = O(10^3)$, then for this model configuration, the system would no longer oscillate.

The strength of the air-sea coupling is controlled by the parameter κ, as seen in the second panel. This parameter was theorised to be a negative feedback for this mechanism in Chapter 3, and from inspection of equations 5.1 and 5.2, it is clear that the difference between the ocean and atmospheric boundary layer temperatures decays exponentially ignoring all other influences, as also seen in the fixed ocean model in Fig. 5.4. The inclusion of a dynamic ocean

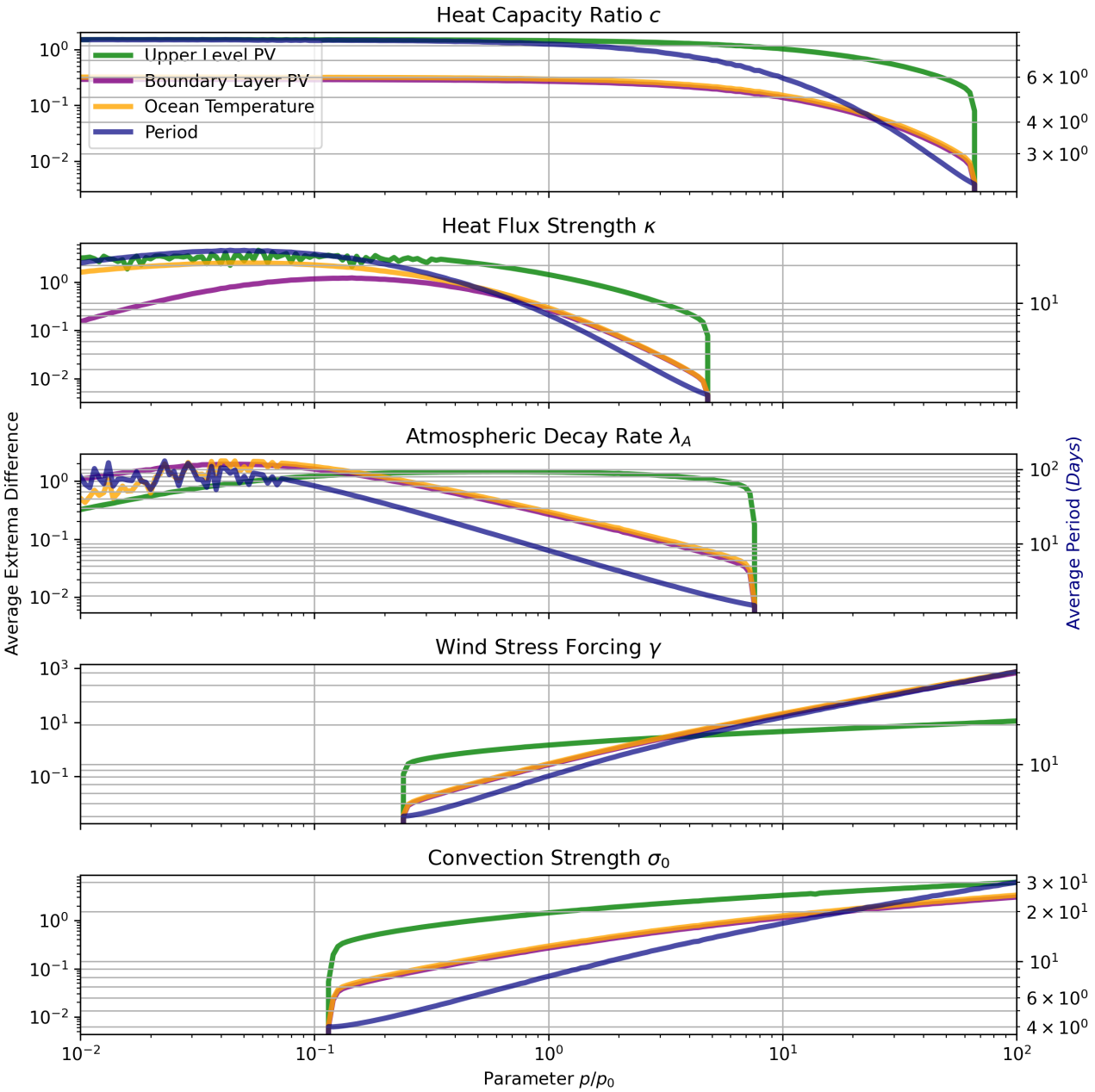


Figure 5.10: Plot showing the average period of oscillation, shown in navy, and the average difference between successive maxima and minima with changes in control parameters. The upper-level PV, boundary layer PV, and ocean temperature are shown in green, purple, and orange, respectively. Parameters are set to $\sigma_{00} = 535$, $\kappa = 11$, $c_0 = 0.006$, $\gamma_0 = 0.6$, and $\lambda_{A0} = 0.2$ when they are not undergoing modification.

does not change this relationship, as increasing the strength of this parameter decreases the size between successive extrema and the period of oscillation. Similarly, the same is true for the rate of decay of the atmosphere λ_A, as shown in the third panel of Fig. 5.10.

Both the wind stress forcing γ and the convective strength σ_0 parameters, shown in the fourth and fifth panels respectively, act in similar ways. Both the period of oscillation and the difference

between succeeding extremes increase as these parameters are increased. Hence, these two parameters can be thought of as driving the three box model. Importantly, both are needed in order for oscillations to occur, as with small enough values, the system will collapse to a stable fixed point even if the other parameter remains untouched.

For all parameters, there is a value p_{Hopf} where a Hopf bifurcation occurs. Beyond this point, the average period grows logarithmically until saturation, at which time this parameter no longer dominates the timescales of the system. Calculating the slope before saturation occurs gives a relationship for the power law between the period of oscillation and the parameter of interest. This relationship is approximately:

$$T \propto \frac{\sqrt[3]{\sigma_0}}{\lambda\kappa}\sqrt{\frac{\gamma}{c}}, \tag{5.10}$$

where T is the average period of oscillation. Notably, there are some similarities between this model and that of a damped harmonic oscillator. Here, c takes the role of the inverse of mass, while γ is the inverse of the spring constant. Therefore, a larger oceanic mixed layer heat capacity (or a smaller atmospheric boundary layer heat capacity) is equivalent to a larger mass on a spring, indicating more thermal inertia. Additionally, less Ekman transport forcing is equivalent to a stronger spring constant. The heat flux strength κ and the atmospheric decay rate λ_A act as the damping ratio in this harmonic oscillator, a result also observed in the fixed ocean model in Section 5.4.1.

Now exploring the position of the local extrema, Fig. 5.11 shows the bifurcation diagram of the upper-level PV with changes in the convection parameter σ_0. As in the fixed point analysis, there is a stable fixed point seen for weak convection parameterisation, which then bifurcates at $\sigma_0 = \sigma_{Hopf}$ into a stable limit cycle. Furthermore, this system sees a number of period doublings (not shown) before a chaotic regime is achieved at $\sigma_c \approx 117$, as indicated by the Lyapunov exponent shown by the red line. After this point, a window of predictability is seen, and more numerous periodic orbits are observed, as shown in the zoomed section of Fig. 5.11.

As the convection parameter is increased further, the distance between the extrema is also increased, although this primarily affects the minimum upper-level PV. Hence, in this model, as convection is increased, blocks become stronger and last for longer. Additionally, there is also a general increase in the Lyapunov exponent as convection is strengthened, meaning that the

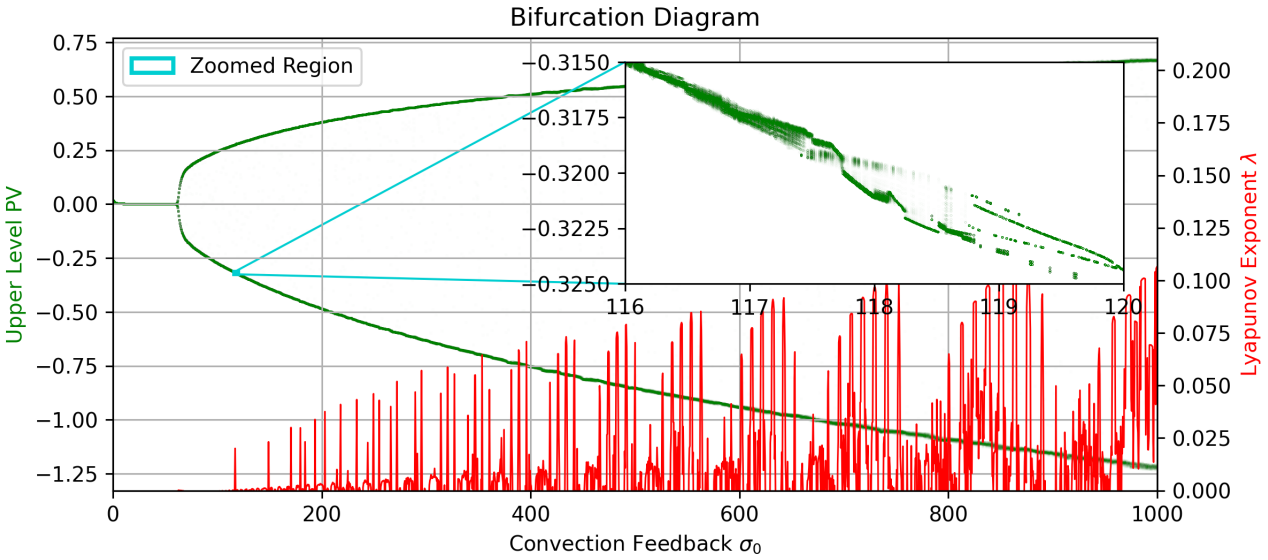


Figure 5.11: Bifurcation diagram of the three-box model with variations in the convection strength σ_0, including a zoomed-in region indicated by the light blue box. The largest Lyapunov exponent is plotted in red. Parameters are set to $\kappa = 11$, $c = 0.006$, $\gamma = 0.2$, and $\lambda_A = 0.2$

system becomes more unpredictable. Assuming there is a 1% error in the measurement of the initial condition, and the Lyapunov exponent $O(0.1)$, then the time horizon where prediction is possible from the system is $O(50$ days).

5.5 Discussion

5.5.1 The Fixed Ocean Model

Although this model is very simple at its core, it demonstrates some of the concepts discussed in Section 3.4. Notably, the strength of the oceanic preconditioning affects both the negative PV anomalies generated in the boundary layer and the strength of negative PV anomalies in the upper troposphere that create the atmospheric block. The block can remain present in the upper troposphere indefinitely, provided that the surplus heat content is strong enough and remains unchanged. When there is no surplus heat in the ocean, negative PV anomalies cannot be generated in the boundary layer, nor can they be transported to the upper troposphere, thus cutting off the block from the oceanic pathway.

While heat content anomalies in the GS extension, and other WCBs, tend to lose their heat to the atmosphere via heat flux, these anomalies are primarily generated by oceanic transport (Kelly 2004). Given the strength and persistence of this heat transport, these anomalies might

persist far longer than expected if only accounting for air-sea heat fluxes. This offers a plausible explanation for the significant increase in blocking frequency seen after a period of increased heat transport in Fig. 3.6. Notably, unlike the implication in the coupled model, this heat transport can arise from forcing other than atmospheric surface winds driving ocean currents. Hirschi et al. (2019) found that the GS exhibits its own chaotic variability, partly due to the deposition of vortices in the Gulf of Mexico, allowing more mass transport due to a continuity argument.

5.5.2 The Fully Coupled Ocean

When deriving the three-box coupled model, many choices and simplifications can be made, allowing for the retention of certain physics while excluding others. The goal of this model was to mimic the real-world oceanic pathway to atmospheric blocking, with transport observed primarily by Yamamoto et al. (2021) and Wenta et al. (2024), and oceanic influence observed and tested in Chapter 3 and 4, and to test the dependence on physical processes. Therefore, this model had to include convection from the boundary layer to the upper troposphere and heat flux from the ocean to the atmospheric boundary layer. After this point, additional modifications can be included to examine their role in driving or damping this simple model. First, the convection parameterisation will be discussed.

Convection

The first and most important of these choices was the convection parameterisation. This parametrisation retained all of the non-linearity in the final model while also determining the mass flux from lower to upper levels. Initially, the linear approximation $\sigma(Q_B) = \sigma_0 - \beta Q_B$ was chosen based on a simple Taylor expansion, resulting in a complex chaotic attractor. However, this choice led to nonphysical processes. Specifically, once $Q_B > \sigma_0/\beta$, air flowed from the upper levels to the boundary layer, initiating a positive feedback loop and resulting in a strong negative PV anomaly in the upper levels, which did not mimic the oceanic pathway. Consequently, the decision was made to ensure that the convection scheme maintained $\sigma \geq 0$.

Sheldon et al. (2017) demonstrated that both the absolute SSTs and SST gradients affect the amount of mass transported from the boundary layer along the WCB of a cyclone and into

the upper troposphere. The former relates primarily to gravitational instability, as detailed by Bennetts & Hoskins (1979), which is the parameterisation used in the model seen in Equation 5.4, while the latter implies slantwise instability. It is therefore reasonable to ask, how would the model behave if a slantwise convection scheme was use instead?

Emanuel (1983) explains that the strength of slantwise instability primarily depends on the shear of the meridional wind as follows:

$$\sigma = \sqrt{f v_z}, \tag{5.11}$$

where f is the Coriolis parameter, and v_z is the vertical shear of the meridional wind. We can further expand the vertical shear in terms of the thermal wind, resulting in:

$$\sigma(\theta_B) \approx \sqrt{\frac{g}{\theta_0}\frac{\theta_B - \theta_{In}}{L}}, \tag{5.12}$$

where L is the typical length scale considered, and θ_{In} is the equivalent potential temperature incoming into the atmospheric boundary layer above the ocean. Using this parameterisation, convection is triggered when $\theta_B > \theta_{In}$.

In both the slantwise and gravitational instability cases, heating from the ocean acts to destabilise and increase the temperature of the atmospheric boundary layer, thereby triggering convection in both parameterisations once a positive anomalous temperature, θ^*, is reached. Thus, these convection schemes are effectively equivalent when θ_{In} is constant. However, if the incoming air temperature into the boundary layer is a dependent variable, the model's behaviour will change, as in the case when a CAO feedback is included. When a block is present over the North Atlantic, cold air is advected over the Gulf Stream (Kolstad et al. 2009). This can be parameterised in the box model as:

$$\theta^*_{In}(Q_A) = \alpha Q_A, \tag{5.13}$$

where α is the CAO feedback parameter. In a slantwise scheme, this CAO feedback increases the horizontal temperature gradient, leading to stronger convection, depositing more negative PV anomalies from the boundary layer into the block, resulting in a positive feedback. However,

in the case of gravitational instability, this CAO feedback does not directly modify convection, but does so indirectly. To see this indirect effect, the role of advection must be examined.

As inferred from Cauchy's mean value theorem seen in Equation A.5, $Q_B \propto -\theta_{BL}$. Using the same relation for air that enters the atmospheric boundary layer over the ocean, together with the CAO feedback parameterisation seen in Equation 5.13, it is clear that when a block exists over the NA, the cold air that is advected over the ocean also has a positive PV anomaly. Using the gravitational instability parameterisation, once a block is established, although it does not affect convection, it quickly fills the boundary layer with positive PV and stops convection from occurring, resulting in a negative feedback. Hence, the choice of convection parameterisation determines a portion of the feedbacks in the system, which ultimately shape the nature and predictability of the dynamical system of interest.

This difference in feedbacks as a result of the chosen convection parameterisation is further distinguished when examining advection in the slantwise scheme. In Emanuel (1983)'s first description of slantwise convection, seen in Equation 15, the temperature profile does not depend on height and, therefore:

$$Q_B = -\frac{v_z}{\rho_{BL}} \frac{\partial \theta_{BL}}{\partial x}, \tag{5.14}$$

where v_z is the vertical shear of the meridional wind. Using the thermal wind relation, we can see that $Q_B \propto -\frac{\partial \theta_{BL}}{\partial x}^2$, and hence is always negative. Again, using this relation for the incoming air, there is always negative PV entering the atmospheric boundary layer, although this is strengthened when the land-sea contrast is more pronounced. Therefore, when a block is present, not only is there a direct effect of increased convection due to the CAO feedback, but the magnitude of the negative PV advected over the ocean is stronger, resupplying the negative PV anomaly, further enhancing the positive feedback.

Heat Flux

While the convection parameterisation introduces the primary non-linearity in this model, there is also potential for another non-linearity through the bulk formula from Bjerknes (1964) as seen in (Gill 1982, Equation 2.4.5):

$$F = \frac{\rho_{BL} c_p c_H u(\theta - \theta_{BL})}{h_{BL}}, \tag{5.15}$$

where c_H is the Stanton number. In particular, this wind speed depends on the large scale flow, with wind speed over the GS extension negatively correlated with the NAO (Zubiate et al. 2017, Fig. 5a). Therefore, wind speed could be parameterised by the upper-level PV, with negative values relating to the negative NAO phase and vice versa. Importantly, wind speed is strictly positive, so this parameterisation must reflect that. With this in mind, when a block is formed, the wind speed decreases over the GS extension, decreasing the magnitude of the heat flux between the ocean to the atmosphere for a given temperature difference. Assuming there is a positive temperature anomaly in the oceanic mixed layer such that the atmospheric boundary layer is heated by the ocean, this results in less PV being destroyed in the boundary layer, thereby reducing the supply of negative PV air mass for the block. Hence, the inclusion of this non-linearity acts as a negative feedback. However, upon implementing this non-linearity through a number of parameterisations (not shown), there is little effect on the model quality other than to dampen the system. While wind speed does affect heat flux, the primary driver in both magnitude and direction is the difference in oceanic and atmospheric temperatures (Cayan 1992, Kelly 2004). Hence, this non-linearity has been ignored for simplicity.

Additional Coupling

When designing a simple heuristic model, one must decide on the domain and the limitations on movement through it. For example, the boundary layer box allows air to flow through, resulting in the exponential decay of any anomalous PV in this box. However, preventing through flow and only allowing air mass to move in and out of this box when convection is triggered does not change the quality of the model, but reduces the decay rate of the lower box. The same relation is true for Ekman transport in the oceanic mixed layer.

One final choice of non-linearity comes in the form of advection, which is implicit in the material derivative. As discussed above, the wind speed, and hence advection in and out of the boundary layer box, depends on whether the synoptic structure is zonal or blocked in nature. Hence, the advection of air in and out of the boundary layer depends on the PV in the upper level. When the flow is blocked, this results in less incoming PV, and the air mass in the boundary layer has more exposure to the diabatic effects of air-sea interactions. Assuming positive heat flux

from the ocean to the atmosphere, this means more negative PV is generated in the boundary layer, which in turn maintains the block, resulting in a positive feedback effect. The inclusion of this non-linearity also tends to dampen the effects of the CAO feedback as less "fresh" air is advected into the boundary layer box. Although interesting in design, the inclusion of this non-linearity did not change the quality of the model (not shown), and hence it was omitted for simplicity.

As seen in Fig. 3.6, a strong modulator of atmospheric blocking is heat transport through the Florida Straits. While other inclusions of non-linearity through advection did not significantly modify the model, the nonlinearities present in Ekman transport did. The reason being that without some thermal forcing on the ocean, the ocean only acted to reduce its temperature difference with the atmosphere, and hence no anomalies hot enough to create the oceanic pathway were possible. Modifications to this term and how it is parameterised will change the behaviour of the model (not shown), and more work is needed to thoroughly include the effects of ocean-atmosphere coupling (Czaja & Marshall 2001) and the GS's intrinsic chaotic variability (Hirschi et al. 2019) in the ocean's heat transport.

5.5.3 Implications for Observations and Modelling

With both the fixed and fully coupled oceans, this simple model shows increased blocking with higher ocean temperatures. This was previously observed in Chapter 3 Fig. 3.7 on sub-seasonal timescales, and on decadal timescales by Häkkinen et al. (2011). Not only does this model provide an explanation for this teleconnection, but it also theorises a relationship between the maximum ocean temperature and the succeeding block, both for decadal timescales in the fixed ocean model and sub-seasonal timescales in the fully coupled model.

A surprising result from this model is that the timescale of this interaction depends on several key parameters, notably the heat capacity ratio, the strength of convection, and the wind stress forcing. This presents a theoretical model for coupling timescales that can be verified using spectral analysis on observational data, as previously done by Barsugli & Battisti (1998) and Czaja & Marshall (2001). For example, the seasonal cycle of the mixed layer depth has been well observed by de Boyer Montégut et al. (2004), varying by an order of magnitude from summer to winter. Examining the change in resonant frequencies that are concurrent in both the ocean mixed layer and the upper troposphere across different seasons could verify

this relationship while also helping to define the remaining parameters seen in Equation 5.10. Extending this idea to GCMs, spectral analysis could be used to test the quality of both the resolved convection and the wind-driven ocean currents by the large-scale flow. Given that blocking is largely underrepresented in climate models (Woollings et al. 2018), this approach could be useful in identifying which processes in the model are underrepresented, as in the case of the driving parameters σ_0 and γ, or overestimated, as in the case of the damping parameters λ_A and κ.

This model has shown that there is significant sensitivity to the chosen parameters. When the convection strength is increased, the model exhibits a Hopf bifurcation, followed by a series of period doublings until a chaotic regime is reached, as seen in Fig. 5.11. Beyond this point, there are numerous windows of periodicity and chaotic regimes with increasing Lyapunov exponents. Therefore, depending on the strength of the parametrisation, the model could either be in a predictable periodic regime or a chaotic one with a drastically different time horizon. Due to the fractal nature of this model, it is impossible that any chosen parameter values will actually represent the Earth's system, let alone the inherent difficulties regarding sensitivity to initial conditions. This highlights the importance of stochastically perturbed physical tendency (SPPT) schemes (Subramanian & Palmer 2017) in ensemble forecasting, particularly in fully coupled ocean-atmosphere models.

The sensitivity of this model's behaviour isn't confined to the convection scheme; it extends to all processes within the model, as illustrated in Fig. 5.10. Adjusting any of the parameters can lead to shifts between chaotic and periodic regimes. Notably, the inclusion and intensity of wind stress forcing significantly impact the model's performance. This suggests that for accurate sub-seasonal forecasting, it is crucial for a GCM to effectively couple large-scale atmospheric flow with the resulting oceanic transport. As demonstrated in Fig. 4.15 and in the work of Famooss Paolini et al. (2022), higher-resolution models exhibit a stronger response to oceanic perturbations. This could be due to better-resolved upward motion (as shown in Fig. 9 of Sheldon et al. (2017)), improved propagation of large-scale atmospheric flow to oceanic transport, or some other coupling process.

5.6 Conclusion

In this study, a heuristic three-box model was derived to illustrate the oceanic pathway to atmospheric blocking. This model demonstrates:

1. A resemblance to the real-world oceanic pathway to atmospheric blocking, as observed by Mathews & Czaja (2024).
2. The strength of an atmospheric block depends on the magnitude of the prescribed positive temperature anomaly in the ocean, with no oceanic pathway when negative temperature anomalies are present in the ocean.
3. The signal of causality for a block propagates from the oceanic mixed layer to the atmospheric boundary layer, and finally to the upper troposphere, with the strength of the ocean temperature maximum being negatively correlated with the strength of the successive PV minima.
4. Modifications to all parameters in the box model resulted in a Hopf bifurcation, followed by period doubling and a series of chaotic regimes with increasing unpredictability.
5. The choice of convection parameterisation determines the nature of the CAO feedback, being either negative or positive for gravitational or slantwise instability, respectively.

After finding observational evidence for the oceanic pathway to atmospheric blocking (Mathews & Czaja 2024) and testing that causal relationship on the ECMWF's IFS (Mathews et al. 2024), we have now explored this pathway theoretically through the use of a simple three-dimensional heuristic model. While this model does not aim to accurately forecast atmospheric blocking, it allows for a theoretical exploration of this pathway and provides an improved understanding of the relevant processes involved and parametric dependence. Further additions and modifications to this model may provide a more accurate depiction of the real world, offering greater insight into the strength and importance of the feedbacks present in this mechanism and inspiring future observational research and high-resolution experimentation on GCMs.

Chapter 6

Conclusion

6.1 Summary of Thesis Achievements

This thesis sought to establish a link between Gulf Stream dynamics and atmospheric blocking, aiming to understand how this western boundary current influences the frequency, severity, and persistence of these blocking events. Not only has this link been identified, but the causal relationship between the Gulf Stream (GS) and atmospheric blocking has also been tested and confirmed using both a heuristic model and a high-resolution coupled experiment.

In Chapter 3, using ERA5, RAPID, and ARGO data, it was found that the frequency of atmospheric blocking nearly doubled during December, January, February (DJF) following anomalous heat transport through the Florida Straits five months prior. This anomalous heat transport triggers a chain of events starting with an increase in heat content in the oceanic mixed layer, followed by increased heat flux from the ocean to the atmosphere, generating more negative PV in the atmospheric boundary layer. It was theorised that this diabatically modified boundary layer air is transported to the upper troposphere via the moist handover mechanism first observed by Papritz et al. (2021) and shown to contribute to a block's negative PV anomaly by Wenta et al. (2024). Whether the quality of the PV in the Warm Conveyor Belt (WCB) outflow, the frequency of WCB activity, and the intensity of WCB convection are modified by this surplus heat transport into the North Atlantic remains to be observed in future observational and reanalysis studies.

This observational link was then tested in Chapter 4 through a sensitivity experiment using the ECMWF IFS, where Surface Latent Heat Flux (SLHF) was suppressed over the GS region.

This resulted in a reduction of atmospheric blocking frequency by up to 30%, most prominently over the North Atlantic storm track and Europe, but also throughout the Northern Hemisphere. This signal was strongest in the winter months, although a significant reduction in atmospheric blocking frequency was also observed in summer. In addition to a reduction in blocking frequency, the resulting blocks were smaller in size, less intense (measured as PV anomaly per area), and had shorter lifespans, although more individual blocking anticyclones were formed. Rossby waves with higher zonal wave numbers were observed when GS SLHF was suppressed, exhibiting less stationarity than in the control experiment. Although no statistically significant differences were observed between resolutions, the strongest and only statistically significant signal above the 95^{th} percentile for all blocking characteristics was observed in the highest resolution experiment at approximately 18km.

When GS moisture flux was suppressed, less heat was removed from the ocean, resulting in the increase of SSTs along the GS extension. This resulted in an increase in surface sensible heat flux from the ocean to the atmosphere, reducing static stability and generating more negative PV in the atmospheric boundary layer. However, without sufficient moisture in the North Atlantic storm track, this airmass could not produce the latent heating necessary to ascend, as evidenced by reduced WCB activity. The PV quality in the WCB outflow was more negative without GS SLHF, although fewer negative PV anomalies were transported overall, leading to more blocking in the control experiment. While it was seen that more negative PV anomalies were generated in the boundary layer in the NO_GS_SLHF experiment compared to the control, this signal was not evident in the WCB inflow. Ultimately, a Lagrangian approach is needed to properly understand how the transport of boundary layer air is altered without moisture transfer from the GS region.

In the final study in Chapter 5, a heuristic three-box model was derived, coupling an oceanic mixed layer to an atmospheric boundary layer through air-sea heat fluxes, and the latter to the upper troposphere through convection. This simple model showed similarities to real-world mechanisms, mimicking the observations seen in Chapter 3, such as positive (negative) heat anomalies in the ocean before (after) a block. This model demonstrated that the magnitude of the ocean's heat content maximum was negatively correlated with the minimum PV in both the boundary layer and the upper troposphere, while the upper troposphere extrema exhibited a weak connection with the subsequent lower domain extrema, suggesting an upward causal

relationship. Modifications to all control parameters resulted in a Hopf bifurcation, with the period of oscillations resembling simple harmonic motion. Notably, increasing the strength of convection generally coincided with stronger blocking anomalies, while an increasing positive Lyapunov exponent indicated chaotic behaviour and decreased predictability.

The combined work produced in Chapters 3 - 5 provides theoretical, observational, and modeling evidence of the link between the Gulf Stream and atmospheric blocking. While more work is needed to assess the robustness of these results across models, understand the importance of resolution, and account for these results in the context of a warmer climate, especially with an anomalously warm Gulf Stream (Saba et al. 2016), this step in providing coupling evidence between the Gulf Stream and the midlatitude jet stream on subseasonal timescales has improved our understanding of how western boundary currents can contribute to the dynamics associated with extreme weather.

6.2 Applications

As discussed in Section 3.4.3, the most obvious and useful application of these results is to use heat transport from the Florida Straits as a seasonal and subseasonal index for predictability. Although the atmosphere is responsible for most air-sea heat flux driven by atmospheric temperatures at the ocean surface (Frankignoul & Hasselmann 1977), it seems that on seasonal and subseasonal timescales, the amount of heat in the ocean indeed modulates the strength of this interaction. The removal of this surplus heat from the ocean produces moisture in the atmosphere that can be used for later ascent across dry isentropes and also diabatically modify this airmass, changing the quality of its PV. This suggests, as also discussed by Kelly et al. (2010), using heat content in the oceanic mixed layer rather than SSTs as a better predictor for subseasonal forecasts. A simple example of this was seen in the heuristic blocking model used in Chapter 5, where the model's behavior was modulated by the ratio of atmospheric boundary layer and oceanic mixed layer heat capacities, c, emphasizing the importance of thermal inertia rather than just the temperature anomaly.

As seen in the work of Sheldon et al. (2017), the transport from the atmospheric boundary layer to the upper troposphere depends on the resolution of the model used. Additionally, Famooss Paolini et al. (2022) observed different responses to GS front shifts in models with

resolutions of 100km and above compared to those with finer resolution. Although the resolutions used in Chapter 4 were finer than 100km, differences in the frequency of WCBs were observed between resolutions. Therefore, this work emphasizes the importance of resolution in GCMs to accurately resolve upward transport from the atmospheric boundary layer to the upper troposphere.

Moreover, as shown by Barsugli & Battisti (1998), coupling between the atmosphere and the ocean enhances the variance in both domains while also reducing energy transfer between them. This effect was seen in the heuristic model in Chapter 5, where the fixed ocean model exhibited only one stable fixed point and large blocking anomalies for comparatively small ocean temperature anomalies, compared to the fully coupled model that exhibited chaotic behavior and weaker anomalies. With the next generation of reanalysis, such as ERA6, expected to be fully coupled, this will likely improve the quality of the results observed in Chapter 3 and further highlight the importance of coupling between domains in numerical weather prediction.

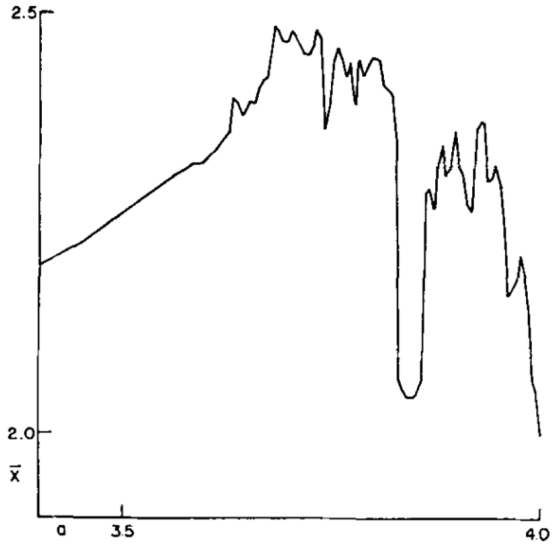


Figure 6.1: The mean of variable X with small changes in parameter a for a logistic map, taken from Lorenz (1964) Fig. 3.

One final note on modeling is the importance of stochastically perturbed physical tendency schemes (Subramanian & Palmer 2017). As seen in the simple heuristic model in Chapter 5, small modifications to the control parameters resulted in bifurcations from periodic regimes into chaotic behavior with varying predictability. Due to the inherent uncertainty in measuring these control parameters, correct parameterisation of these processes is impossible. In simple models like the one used here, infinitesimal perturbations can lead to entirely different behaviors

due to the fractal nature of the system. As shown by Lorenz (1964), this has implications for deducing the climate given the governing equations, as illustrated in Fig. 6.1. Hence, sampling a range of control parameters for ensemble integration will at least allow for probing somewhat likely physical process configurations, giving insight into possible climate outcomes.

6.3 Future Work

While this work highlighted the importance of oceanic preconditioning in maintaining and modulating air-sea interactions, it focused solely on forcing in the direction perpendicular to the air-sea interface. Quantifying the role of frontal interactions between the GS and cyclones, as seen in Minobe et al. (2008), O'Reilly et al. (2016), and Sheldon et al. (2017), was not explored. SST fronts help generate the baroclinicity needed to anchor storm tracks and may also modify horizontal heating gradients in the atmosphere. Due to the direction of the horizontal vorticity vector in cyclones resulting from the thermal wind, this frontal interaction will generate negative PV only in the Northern Hemisphere, as illustrated in Fig. 6.2. Hence it is likely that the understanding in Chapter 3 was an underestimation of the true influence of the GS on the midlatitude jet stream. It is then suggested that one could extend the approach used here to focus on the contribution of frontal interactions and how they affect mass transport from the boundary layer to the upper troposphere and the quality of air transported. Moreover, this could be extended to consider the coupled effects on the ocean, such as the role of heat transport through the Florida Straits in modifying the GS SST gradients and wind stress from the resulting cyclones then feeding back on the Florida Straits heat transport through Ekman transport as suggested by Hoskins & Valdes (1990).

Undoubtedly, the weakest point in this analysis is the assumption of net conservation of PV along the WCB of a cyclone, as theorised by Methven (2015). In reality, this is only approximately observed, and the effect of latent heating along the WCB can generate PV dipoles due to horizontal heating gradients, as seen in Fig. 6.2 from Oertel et al. (2020). To quantify the relationship between WCB PV inflow and outflow, a Lagrangian-based analysis is required, accounting for differences in inflow and outflow pressure, latitudes, relative humidity, relative vorticity, etc. This will not only enable an accurate interpretation of the mechanisms at play but also quantify the role of the magnitude of the boundary layer PV in modifying the strength of the instabilities, as parameterised in the heuristic blocking model, if at all.

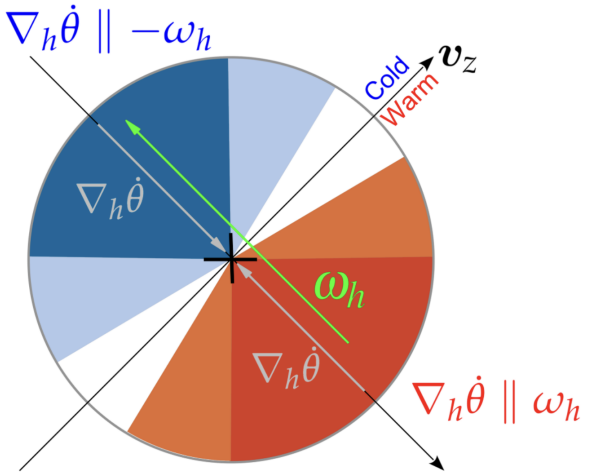


Figure 6.2: Fig. 1 from Oertel et al. (2020), showing the diabatic effect of PV through the interaction of horizontal vorticity and the horizontal gradient of heating across the cold front of the cyclone. Here ω_h is the horizontal vorticity vector.

Finally, both the SLHF sensitivity experiment seen in Chapter 4 and the fixed ocean model seen in Chapter 5 Section 5.4.1 raise questions regarding incomplete processes in GCMs. As we have seen in these experiments, with oceanic responses to atmospheric forcing suppressed, both the accuracy and variability of these models are greatly reduced. This raises the question: which coupling processes in the Earth system are not accurately represented in models, and how does the neglect of these processes generate biases in them? For example, will higher resolution maps of the ocean floor suspected to be produced by Seabed in 2030 correct biases in ocean circulation? To what extent will increased confidence in cloud feedbacks constrain future projections of global temperatures? How exactly does the biosphere feedback on the atmosphere, hydrosphere and cryosphere? While reductions in model complexity are necessary steps to generate usable forecasting systems, certain simplifications may be more detrimental than others. Understanding these complex coupled relationships across the climate system will not only improve predictions but also bolster society's confidence in these predictions in the years to come.

Appendix A

Diabatic PV Generation

The diabatic change in moist potential vorticity is given by:

$$\frac{DQ_e}{Dt} = \frac{f + \zeta_z}{\rho}\frac{\partial \dot{\theta}_e}{\partial z} + \frac{\vec{\zeta_H}.\vec{\nabla}_H \dot{\theta}_e}{\rho}, \tag{A.1}$$

where Q_e is moist potential vorticity, $\vec{\zeta}$ is the absolute vorticity, θ_e is the equivalent potential temperature, ρ is the density and z and H indicate the vertical and horizontal components. For air-sea interactions, the first term accounts for the flux from the ocean to the atmosphere while the second term describes the interaction of frontal structures (large horizontal temperature gradients). Average values of ζ_z in the cold sector of cyclones are $O(10^{-5}\mathrm{s}^{-1})$ and therefore, this term will be ignored due to its small effect relative to the Coriolis parameter. For the purpose of this paper, only the first term on the right hand side of equation A.1 will be investigated, i.e.:

$$\frac{DQ_e}{Dt} \approx \frac{f}{\rho}\frac{\partial \dot{\theta}_e}{\partial z}. \tag{A.2}$$

The above equation is written in a Lagrangian framework, and therefore the time scales, Dt, considered is the time that an atmospheric particle travels over the WBC, Δt_A. This also implies that the volume being considered is that which is affected by the oceanic heat flux, i.e. the atmospheric boundary layer of height h_{BL}, with moist PV Q_e. In order to link this equation with the observables above, the atmospheric heating in the boundary layer must be introduced. This is given by:

$$\begin{aligned} F_s &= \int_0^{h_{BL}} C_A \rho_{BL} \dot{\theta}_e(z) dz, \\ &= h_{BL} C_A \rho_{BL} \overline{\dot{\theta}_e}, \end{aligned} \tag{A.3}$$

where F_s is the turbulent and radiative heat flux from the ocean to the atmosphere, ρ_{BL} is the density of the boundary layer (assumed constant), C_A is the specific heat capacity of air and the bar indicates the average throughout the boundary layer. Making use of Cauchy's mean value theorem between the ocean surface and the top of the atmospheric boundary layer gives the following relation:

$$\overline{\dot{\theta}_e} = \left. \frac{\dot{\theta}_e}{\frac{\partial \dot{\theta}_e}{\partial z}} \right|_{z=c} \overline{\frac{\partial \dot{\theta}_e}{\partial z}}, \tag{A.4}$$

where c is some height between the sea surface and the top of the atmospheric boundary layer. Applying an orders of magnitude argument to the term evaluated at $z = c$ in A.4 results in:

$$\overline{\dot{\theta}_e} \approx -h_{BL} \overline{\frac{\partial \dot{\theta}_e}{\partial z}}. \tag{A.5}$$

The minus sign is included as the average heating throughout the boundary layer is assumed to be positive and decay with height. Now inserting this relation into equation A.3 results in:

$$\overline{\frac{\partial \dot{\theta}_e}{\partial z}} = -\frac{F_s}{C_A \rho_{BL} h_{BL}^2}. \tag{A.6}$$

The surface heat flux F_s is sustained by an anomalous ocean heat transport convergence:

$$F_s = \Delta HT. \tag{A.7}$$

The latter is what is building up the change in ocean heat content over a timescale Δt_O:

$$\Delta HT = \frac{\Delta HC}{\Delta t_O}. \tag{A.8}$$

Approximating the material derivative in equation A.2 by overall change, i.e.:

$$\begin{aligned} \frac{DQ_e}{Dt} &\approx \frac{\Delta Q_e}{\Delta t_A} \\ &\approx \frac{f}{\rho_{BL}} \overline{\frac{\partial \dot{\theta}_e}{\partial z}}, \end{aligned} \tag{A.9}$$

and combining equations A.6, A.7 and A.8 results in:

$$\Delta Q_e = -f \left(\frac{\Delta t_A}{\Delta t_O} \right) \frac{\Delta HC}{C_A (\rho_{BL} h_{BL})^2}. \tag{A.10}$$

We see from this equation that a positive heat content build up relates to the generation of negative moist PV anomalies in the boundary layer. Making use of the hydrostatic balance ($g\rho_{BL}h_{BL} = \Delta P_{BL}$) and relating the change in heat content of the ocean to the change in potential temperature ($\Delta HC = C_O \rho_O h_{ML} \Delta\theta_O$) results in:

$$\Delta Q_e = -\frac{fg\Delta\theta_O}{\Delta P_{BL}} \left(\frac{\Delta t_A}{\Delta t_O} \right) \left(\frac{C_O \rho_O h_{ML}}{C_A \rho_{BL} h_{BL}} \right), \tag{A.11}$$

where h_{ML} is the mixed layer thickness of the ocean and ΔP_{BL} is the pressure difference from the bottom to the top of the boundary layer. Notably, the generation of negative moist PV has dependence on latitude through the Coriolis parameter, and on the height of the atmospheric boundary layer, with higher latitudes and shallower atmospheric boundary layers generating more negative moist PV for the same change in heat content, ΔHC. Moreover, a deeper oceanic mixed layer has larger thermal inertia and therefore generates more negative moist PV in the boundary layer. The ratio of the atmospheric to the oceanic timescales also determines the strength of this interaction, with faster airflow at low level reducing the efficiency of the negative moist PV generation. Additionally, a slow build up of oceanic heat content anomaly also reduces the efficiency of negative moist PV generation.

Considering the moist-adiabatic transport of this lower-level air mass to the upper levels of the atmospheric block, we assume that the boundary layer moist PV is approximately equal to the upper-level PV due to the absence of moisture sources and that mass is conserved along the ascent. Finally, armed with the knowledge of how much boundary layer air mass is transported to the upper troposphere and considering the negative moist PV anomalies generated by the diabatic processes in the boundary layer, we can now estimate the ratio, denoted as r, of the

mass integrated PV in the block ($\rho_{Block}V_{Block}Q_{Block}$) to that in the boundary layer, namely:

$$\begin{aligned} r &= \frac{\rho_{BL}V_{BL}\Delta Q_e}{\rho_{Block}V_{Block}Q_{Block}} \\ &= \frac{\Delta P_{BL}A_{BL}\Delta Q_e}{\Delta P_{Block}A_{Block}Q_{Block}}. \end{aligned} \tag{A.12}$$

Appendix B

Non-Dimensionlizing the Box Model

The full dimensional equations of motion are:

$$\dot{Q}_A = \frac{\rho_B}{\rho_A}\frac{h_{BL}}{h_A}\sigma(Q_B)Q_B - \lambda_A(Q_A - 1), \tag{B.1}$$

$$\dot{Q}_B = -\frac{f c_H u(\theta + \rho_B h_{BL} Q_B/f)}{\rho_B h_{BL}^2} + \frac{u}{L}(Q_{Land} - Q_B), \tag{B.2}$$

$$\dot{\theta} = -\frac{\rho c_p c_H u(\theta + \rho_B h_{BL} Q_B/f)}{\rho_o c_o h_{ML}} + \phi(Q_A), \tag{B.3}$$

where Q is the PV, θ is the temperature, σ is the convection parameterisation, and ϕ is the temperature transport into the ocean mixed layer parameterisation. u is the average wind speed, ρ is the density, h is the height of the box, L is the typical horizontal length scale, c_p and c_o are the heat capacities of the atmosphere and ocean respectively, f is the Coriolis parameter, c_H is the Stanton number, and λ_A is the control parameter governing the decay times in the upper troposphere. Subscripts A, B, BL, ML, and $LAND$ denote the upper atmosphere, lower atmosphere, boundary layer, mixed layer, and land, respectively.

To non-dimensionalise these equations, the time scale $\tau = L/u$, approximately one day, was chosen, where L is the typical horizontal length scale. Additionally, the PV scale used is

$Q_0 = \frac{f\theta_0}{\rho h_{BL}}$, where θ_0 is the temperature scale. Applying the non-dimensional transformation $x \to x_0\tilde{x}$, where x is the variable of interest and $\tilde{x}$ is its non-dimensional equivalent, results in the following equations:

$$\dot{\tilde{Q}}_A = r\tilde{\sigma}(\tilde{Q}_B)\tilde{Q}_B - \tilde{\lambda}_A(\tilde{Q}_A - 1), \tag{B.4}$$

$$\dot{\tilde{Q}}_B = -\kappa(\tilde{\theta} + \tilde{Q}_B) + \tilde{Q}_{Land} - \tilde{Q}_B, \tag{B.5}$$

$$\dot{\tilde{\theta}} = -c\kappa(\tilde{\theta} + \tilde{Q}_B) + \tilde{\phi}(\tilde{Q}_A), \tag{B.6}$$

where $r = \frac{\rho_B}{\rho_A}\frac{h_{BL}}{h_A}$ is the ratio of mass between the lower and upper boxes, $\tilde{\lambda}_A = \frac{L\lambda_A}{u}$ is the non-dimensional decay rate of the upper box, $\kappa = \frac{c_H L}{h_{BL}}$ represents the strength of the air-sea heat flux, and $c = \frac{\rho c_p h_{BL}}{\rho_o c_o h_{ML}}$ is the ratio of the heat capacities of the atmosphere to the ocean. Notably, the functions $\sigma(Q_B)$ and $\phi(Q_A)$ are in units per second and Kelvin per second, respectively, making their non-dimensional transformation straightforward.

For clarity, the tilde notation has been removed in the main text.

Bibliography

Ambaum, M. H. & Novak, L. (2014), 'A nonlinear oscillator describing storm track variability', *Quarterly Journal of the Royal Meteorological Society* **140**(685), 2680–2684.

Argo, G. (2023), 'Argo float data and metadata from global data assembly centre (argo gdac)', *Seanoe* .

Attinger, R., Spreitzer, E., Boettcher, M., Forbes, R., Wernli, H. & Joos, H. (2019), 'Quantifying the role of individual diabatic processes for the formation of pv anomalies in a north pacific cyclone', *Quarterly Journal of the Royal Meteorological Society* **145**(723), 2454–2476.

Austin, J. (1980), 'The blocking of middle latitude westerly winds by planetary waves', *Quarterly Journal of the Royal Meteorological Society* **106**(448), 327–350.

Bane Jr, J. M. & Osgood, K. E. (1989), 'Wintertime air-sea interaction processes across the gulf stream', *Journal of Geophysical Research: Oceans* **94**(C8), 10755–10772.

Barnes, E. A., Slingo, J. & Woollings, T. (2012), 'A methodology for the comparison of blocking climatologies across indices, models and climate scenarios', *Climate dynamics* **38**, 2467–2481.

Barsugli, J. J. & Battisti, D. S. (1998), 'The basic effects of atmosphere–ocean thermal coupling on midlatitude variability', *Journal of the Atmospheric Sciences* **55**(4), 477–493.

Bennetts, D. A. & Hoskins, B. (1979), 'Conditional symmetric instability-a possible explanation for frontal rainbands', *Quarterly Journal of the Royal Meteorological Society* **105**(446), 945–962.

Bishop, S. P., Small, R. J., Bryan, F. O. & Tomas, R. A. (2017), 'Scale dependence of midlatitude air–sea interaction', *Journal of Climate* **30**(20), 8207–8221.

Bjerknes, J. (1964), Atlantic air-sea interaction, *in* 'Advances in geophysics', Vol. 10, Elsevier, pp. 1–82.

Bolton, D. (1980), 'The computation of equivalent potential temperature', *Monthly weather review* **108**(7), 1046–1053.

Bouillon, S., Maqueda, M. A. M., Legat, V. & Fichefet, T. (2009), 'An elastic–viscous–plastic sea ice model formulated on arakawa b and c grids', *Ocean Modelling* **27**(3-4), 174–184.

Cayan, D. R. (1992), 'Latent and sensible heat flux anomalies over the northern oceans: The connection to monthly atmospheric circulation', *Journal of climate* **5**(4), 354–369.

Cellitti, M. P., Walsh, J. E., Rauber, R. M. & Portis, D. H. (2006), 'Extreme cold air outbreaks over the united states, the polar vortex, and the large-scale circulation', *Journal of Geophysical Research: Atmospheres* **111**(D2).

Charney, J. G. & DeVore, J. G. (1979), 'Multiple flow equilibria in the atmosphere and blocking', *Journal of the atmospheric sciences* **36**(7), 1205–1216.

Charney, J. G. & Eliassen, A. (1949), 'A numerical method for predicting the perturbations of the middle latitude westerlies', *Tellus* **1**(2), 38–54.
URL: *https://onlinelibrary.wiley.com/doi/abs/10.1111/j.2153-3490.1949.tb01258.x*

Cobb, A. & Czaja, A. (2019), 'Mesoscale signature of the north atlantic oscillation and its interaction with the ocean', *Geophysical Research Letters* **46**(10), 5575–5581.

Coumou, D., Petoukhov, V., Rahmstorf, S., Petri, S. & Schellnhuber, H. J. (2014), 'Quasi-resonant circulation regimes and hemispheric synchronization of extreme weather in boreal summer', *Proceedings of the National Academy of Sciences* **111**(34), 12331–12336.

Croci-Maspoli, M., Schwierz, C. & Davies, H. (2007), 'A multifaceted climatology of atmospheric blocking and its recent linear trend', *Journal of Climate* **20**(4), 633–649.

Czaja, A. & Hausmann, U. (2009), 'Observations of entry and exit of potential vorticity at the sea surface', *Journal of Physical Oceanography* **39**, 2280–2294.

Czaja, A. & Marshall, J. (2001), 'Observations of atmosphere-ocean coupling in the north atlantic', *Quarterly Journal of the Royal Meteorological Society* **127**(576), 1893–1916.

Davini, P., Cagnazzo, C., Gualdi, S. & Navarra, A. (2012), 'Bidimensional diagnostics, variability, and trends of northern hemisphere blocking', *Journal of Climate* **25**(19), 6496–6509.

Davini, P., Weisheimer, A., Balmaseda, M., Johnson, S. J., Molteni, F., Roberts, C. D., Senan, R. & Stockdale, T. N. (2021), 'The representation of winter northern hemisphere atmospheric blocking in ecmwf seasonal prediction systems', *Quarterly Journal of the Royal Meteorological Society* **147**(735), 1344–1363.

Davis, C. A. (1992), 'Piecewise potential vorticity inversion', *Journal of the atmospheric sciences* **49**(16), 1397–1411.

de Boyer Montégut, C., Madec, G., Fischer, A. S., Lazar, A. & Iudicone, D. (2004), 'Mixed layer depth over the global ocean: An examination of profile data and a profile-based climatology', *Journal of Geophysical Research: Oceans* **109**(C12).

de Rosnay, P., Browne, P., de Boisséson, E., Fairbairn, D., Hirahara, Y., Ochi, K., Schepers, D., Weston, P., Zuo, H., Alonso-Balmaseda, M. et al. (2022), 'Coupled data assimilation at ecmwf: Current status, challenges and future developments', *Quarterly Journal of the Royal Meteorological Society* **148**(747), 2672–2702.

Dormand, J. R. & Prince, P. J. (1980), 'A family of embedded runge-kutta formulae', *Journal of computational and applied mathematics* **6**(1), 19–26.

Dorrington, J., Strommen, K., Fabiano, F. & Molteni, F. (2022), 'Cmip6 models trend toward less persistent european blocking regimes in a warming climate', *Geophysical Research Letters* **49**(24), e2022GL100811.

ECMWF (2021), *IFS Documentation CY47R3 - Part IV Physical processes*, number 4, ECMWF.
URL: *https://www.ecmwf.int/node/20198*

ECMWF (2023), 'Available at:', `https://www.ecmwf.int/en/publications/ifs-documentation`.

Ekman, V. W. (1905), 'On the influence of the earth's rotation on ocean-currents.'.

Emanuel, K. A. (1983), 'The lagrangian parcel dynamics of moist symmetric instability', *Journal of Atmospheric Sciences* **40**(10), 2368–2376.

Famooss Paolini, L., Athanasiadis, P. J., Ruggieri, P. & Bellucci, A. (2022), 'The atmospheric response to meridional shifts of the gulf stream sst front and its dependence on model resolution', *Journal of Climate* **35**(18), 6007–6030.

Faranda, D., Messori, G. & Yiou, P. (2017), 'Dynamical proxies of north atlantic predictability and extremes', *Scientific reports* **7**(1), 41278.

Fichefet, T. & Maqueda, M. M. (1997), 'Sensitivity of a global sea ice model to the treatment of ice thermodynamics and dynamics', *Journal of Geophysical Research: Oceans* **102**(C6), 12609–12646.

Frankignoul, C. (1985), 'Sea surface temperature anomalies, planetary waves, and air-sea feedback in the middle latitudes', *Reviews of geophysics* **23**(4), 357–390.

Frankignoul, C. & Hasselmann, K. (1977), 'Stochastic climate models, part ii application to sea-surface temperature anomalies and thermocline variability', *Tellus* **29**(4), 289–305.

Gill, A. E. (1982), *Atmosphere-ocean dynamics*, Vol. 30, Academic press.

Gill, A., Green, J. & Simmons, A. (1974), Energy partition in the large-scale ocean circulation and the production of mid-ocean eddies, *in* 'Deep sea research and oceanographic abstracts', Vol. 21, Elsevier, pp. 499–528.

Grams, C. M., Beerli, R., Pfenninger, S., Staffell, I. & Wernli, H. (2017), 'Balancing europe's wind-power output through spatial deployment informed by weather regimes', *Nature climate change* **7**(8), 557–562.

Grams, C. M., Magnusson, L. & Madonna, E. (2018), 'An atmospheric dynamics perspective on the amplification and propagation of forecast error in numerical weather prediction models: A case study', *Quarterly Journal of the Royal Meteorological Society* **144**(717), 2577–2591.

Hadley, G. (1735), 'Vi. concerning the cause of the general trade-winds', *Philosophical Transactions of the Royal Society of London* **39**(437), 58–62.
URL: *https://royalsocietypublishing.org/doi/abs/10.1098/rstl.1735.0014*

Häkkinen, S., Rhines, P. B. & Worthen, D. L. (2011), 'Atmospheric blocking and atlantic multidecadal ocean variability', *Science* **334**(6056), 655–659.

Harvey, B., Methven, J., Sanchez, C. & Schäfler, A. (2020), 'Diabatic generation of negative potential vorticity and its impact on the north atlantic jet stream', *Quarterly Journal of the Royal Meteorological Society* **146**(728), 1477–1497.

Hauser, S., Teubler, F., Riemer, M., Knippertz, P. & Grams, C. M. (2023), 'Towards a holistic understanding of blocked regime dynamics through a combination of complementary diagnostic perspectives', *Weather and Climate Dynamics* **4**(2), 399–425.

Haynes, P. H. & McIntyre, M. (1990), 'On the conservation and impermeability theorems for potential vorticity', *Journal of Atmospheric Sciences* **47**(16), 2021–2031.

Heitmann, K. (2023), Characteristics and Impacts of Warm Conveyor Belts in Present-Day and Future Climate, PhD thesis, ETH Zurich.

Held, I. M. (1983), 'Stationary and quasi-stationary eddies in the extratropical troposphere: Theory', *Large-scale dynamical processes in the atmosphere* **127**, 168.

Hersbach, H., Bell, B., Berrisford, P., Hirahara, S., Horányi, A., Muñoz-Sabater, J., Nicolas, J., Peubey, C., Radu, R., Schepers, D. et al. (2020), 'The era5 global reanalysis', *Quarterly Journal of the Royal Meteorological Society* **146**(730), 1999–2049.

Hewitt, H. T., Bell, M. J., Chassignet, E. P., Czaja, A., Ferreira, D., Griffies, S. M., Hyder, P., McClean, J. L., New, A. L. & Roberts, M. J. (2017), 'Will high-resolution global ocean models benefit coupled predictions on short-range to climate timescales?', *Ocean Modelling* **120**, 120–136.

Hirschi, J. J.-M., Frajka-Williams, E., Blaker, A. T., Sinha, B., Coward, A., Hyder, P., Biastoch, A., Böning, C., Barnier, B., Penduff, T. et al. (2019), 'Loop current variability as trigger of coherent gulf stream transport anomalies', *Journal of Physical Oceanography* **49**(8), 2115–2132.

Holmberg, E., Messori, G., Caballero, R. & Faranda, D. (2023), 'The link between european warm-temperature extremes and atmospheric persistence', *Earth System Dynamics* **14**(4), 737–765.

Hoskins, B. (1974), 'The role of potential vorticity in symmetric stability and instability', *Quarterly Journal of the Royal Meteorological Society* **100**(425), 480–482.

Hoskins, B. (1997), 'A potential vorticity view of synoptic development', *Meteorological Applications* **4**(4), 325–334.

Hoskins, B. J. & Karoly, D. J. (1981), 'The steady linear response of a spherical atmosphere to thermal and orographic forcing', *Journal of the atmospheric sciences* **38**(6), 1179–1196.

Hoskins, B. J., McIntyre, M. E. & Robertson, A. W. (1985), 'On the use and significance of isentropic potential vorticity maps', *Quarterly Journal of the Royal Meteorological Society* **111**(470), 877–946.

Hoskins, B. J. & Valdes, P. J. (1990), 'On the existence of storm-tracks', *Journal of Atmospheric Sciences* **47**(15), 1854–1864.

Huang, B., Thorne, P. W., Banzon, V. F., Boyer, T., Chepurin, G., Lawrimore, J. H., Menne, M. J., Smith, T. M., Vose, R. S., Zhang, H.-M. et al. (2017), 'Noaa extended reconstructed sea surface temperature (ersst), version 5', *NOAA National Centers for Environmental Information* **30**(8179-8205), 25.

Hurrell, J. W., Kushnir, Y., Ottersen, G. & Visbeck, M. (2003), 'An overview of the north atlantic oscillation', *Geophysical Monograph-American Geophysical Union* **134**, 1–36.

Jiménez-Esteve, B., Kornhuber, K. & Domeisen, D. (2022), 'Heat extremes driven by amplification of phase-locked circumglobal waves forced by topography in an idealized atmospheric model', *Geophysical Research Letters* **49**(21), e2021GL096337.

Kautz, L., Martius, O., Pfahl, S., Pinto, J., Ramos, A., Sousa, P. & Woollings, T. (2022), 'Atmospheric blocking and weather extremes over the euro-atlantic sector–a review, weather clim. dynam., 3, 305–336'.

Kelly, K. A. (2004), 'The relationship between oceanic heat transport and surface fluxes in the western north pacific: 1970–2000', *Journal of climate* **17**(3), 573–588.

Kelly, K. A., Small, R. J., Samelson, R., Qiu, B., Joyce, T. M., Kwon, Y.-O. & Cronin, M. F. (2010), 'Western boundary currents and frontal air–sea interaction: Gulf stream and kuroshio extension', *Journal of Climate* **23**(21), 5644–5667.

Kolstad, E. W., Bracegirdle, T. J. & Seierstad, I. A. (2009), 'Marine cold-air outbreaks in the north atlantic: Temporal distribution and associations with large-scale atmospheric circulation', *Climate dynamics* **33**, 187–197.

Kolstad, E. W. & O'Reilly, C. H. (2024), 'Causal oceanic feedbacks onto the winter nao', *Climate Dynamics* pp. 1–14.

Kraus, E. & Turner, J. (1967), 'A one-dimensional model of the seasonal thermocline ii. the general theory and its consequences', *Tellus* **19**(1), 98–106.

Kuo, H.-l. (1951), 'Vorticity transfer as related to the development of the general circulation', *Journal of Atmospheric Sciences* **8**(5), 307–315.

Kuptsov, P. V. & Parlitz, U. (2012), 'Theory and computation of covariant lyapunov vectors', *Journal of nonlinear science* **22**, 727–762.

Lorenz, E. N. (1963), 'Deterministic nonperiodic flow', *Journal of atmospheric sciences* **20**(2), 130–141.

Lorenz, E. N. (1964), 'The problem of deducing the climate from the governing equations', *Tellus* **16**(1), 1–11.

Lorenz, E. N. (1984), 'Irregularity: A fundamental property of the atmosphere', *Tellus A* **36**(2), 98–110.

Madec, G., Bourdallé-Badie, R., Bouttier, P.-A., Bricaud, C., Bruciaferri, D., Calvert, D., Chanut, J., Clementi, E., Coward, A., Delrosso, D. et al. (2017), 'Nemo ocean engine'.

Madonna, E., Li, C., Grams, C. M. & Woollings, T. (2017), 'The link between eddy-driven jet variability and weather regimes in the north atlantic-european sector', *Quarterly Journal of the Royal Meteorological Society* **143**(708), 2960–2972.

Madonna, E., Wernli, H., Joos, H. & Martius, O. (2014), 'Warm conveyor belts in the era-interim dataset (1979–2010). part i: Climatology and potential vorticity evolution', *Journal of climate* **27**(1), 3–26.

Marshall, J., Jamous, D. & Nilsson, J. (2001), 'Entry, flux, and exit of potential vorticity in ocean circulation', *Journal of physical oceanography* **31**(3), 777–789.

Marshall, J., Johnson, H. & Goodman, J. (2001), 'A study of the interaction of the north atlantic oscillation with ocean circulation', *Journal of Climate* **14**(7), 1399–1421.

Marshall, J. & Molteni, F. (1993), 'Toward a dynamical understanding of planetary-scale flow regimes', *Journal of the atmospheric sciences* **50**(12), 1792–1818.

Martínez-Alvarado, O., Joos, H., Chagnon, J., Boettcher, M., Gray, S., Plant, R., Methven, J. & Wernli, H. (2014), 'The dichotomous structure of the warm conveyor belt', *Quarterly Journal of the Royal Meteorological Society* **140**(683), 1809–1824.

Mathews, J. & Czaja, A. (2024), 'Oceanic maintenance of atmospheric blocking in wintertime in the north atlantic', *Climate Dynamics* pp. 1–14.

Mathews, J. P., Czaja, A., Vitart, F. & Roberts, C. (2024), 'Gulf stream moisture fluxes impact atmospheric blocks throughout the northern hemisphere', *Geophysical Research Letters* **51**(13), e2024GL108826. e2024GL108826 2024GL108826.
URL: *https://agupubs.onlinelibrary.wiley.com/doi/abs/10.1029/2024GL108826*

McCarthy, G. D., Smeed, D. A., Johns, W. E., Frajka-Williams, E., Moat, B. I., Rayner, D., Baringer, M. O., Meinen, C. S., Collins, J. & Bryden, H. L. (2015), 'Measuring the atlantic meridional overturning circulation at 26 n', *Progress in Oceanography* **130**, 91–111.

Methven, J. (2015), 'Potential vorticity in warm conveyor belt outflow', *Quarterly Journal of the Royal Meteorological Society* **141**(689), 1065–1071.

Minobe, S., Kuwano-Yoshida, A., Komori, N., Xie, S.-P. & Small, R. (2008), 'Influence of the gulf stream on the troposphere', *Nature* **452**, 206–9.

Molteni, F. & Kucharski, F. (2019), 'A heuristic dynamical model of the north atlantic oscillation with a lorenz-type chaotic attractor', *Climate Dynamics* **52**(9), 6173–6193.

Nakamura, N. & Huang, C. S. (2018), 'Atmospheric blocking as a traffic jam in the jet stream', *Science* **361**(6397), 42–47.

Novak, L., Ambaum, M. & Tailleux, R. (2017), 'Marginal stability and predator–prey behaviour within storm tracks', *Quarterly Journal of the Royal Meteorological Society* **143**(704), 1421–1433.

Oertel, A., Boettcher, M., Joos, H., Sprenger, M. & Wernli, H. (2020), 'Potential vorticity structure of embedded convection in a warm conveyor belt and its relevance for large-scale dynamics', *Weather and Climate Dynamics* **1**(1), 127–153.

O'Reilly, C. H. & Czaja, A. (2015), 'The response of the pacific storm track and atmospheric circulation to kuroshio extension variability', *Quarterly Journal of the Royal Meteorological Society* **141**(686), 52–66.

O'Reilly, C. H., Minobe, S. & Kuwano-Yoshida, A. (2016), 'The influence of the gulf stream on wintertime european blocking', *Climate Dynamics* **47**(5), 1545–1567.

Palmer, T. N. (1993), 'Extended-range atmospheric prediction and the lorenz model', *Bulletin of the American Meteorological Society* **74**(1), 49–66.

Papritz, L., Aemisegger, F. & Wernli, H. (2021), 'Sources and transport pathways of precipitating waters in cold-season deep north atlantic cyclones', *Journal of the Atmospheric Sciences* **78**(10), 3349–3368.

Parfitt, R., Czaja, A. & Kwon, Y.-O. (2017), 'The impact of sst resolution change in the era-interim reanalysis on wintertime gulf stream frontal air-sea interaction', *Geophysical Research Letters* **44**(7), 3246–3254.

Pauluis, O., Czaja, A. & Korty, R. (2010), 'The global atmospheric circulation in moist isentropic coordinates', *Journal of climate* **23**(11), 3077–3093.

Pelly, J. L. & Hoskins, B. J. (2003), 'A new perspective on blocking', *Journal of the atmospheric sciences* **60**(5), 743–755.

Petoukhov, V., Rahmstorf, S., Petri, S. & Schellnhuber, H. J. (2013), 'Quasiresonant amplification of planetary waves and recent northern hemisphere weather extremes', *Proceedings of the National Academy of Sciences* **110**(14), 5336–5341.

Pfahl, S., Schwierz, C., Croci-Maspoli, M., Grams, C. M. & Wernli, H. (2015), 'Importance of latent heat release in ascending air streams for atmospheric blocking', *Nature Geoscience* **8**(8), 610–614.

Pfahl, S. & Wernli, H. (2012), 'Quantifying the relevance of atmospheric blocking for co-located temperature extremes in the northern hemisphere on (sub-) daily time scales', *Geophysical Research Letters* **39**(12).

Primeau, F. (2005), 'Characterizing transport between the surface mixed layer and the ocean interior with a forward and adjoint global ocean transport model', *Journal of Physical Oceanography* **35**(4), 545–564.

Quinting, J. F. & Grams, C. M. (2022), 'Eulerian identification of ascending airstreams (elias 2.0) in numerical weather prediction and climate models–part 1: Development of deep learning model', *Geoscientific Model Development* **15**(2), 715–730.

Randel, W. J. & Held, I. m. (1991), 'Phase speed spectra of transient eddy fluxes and critical layer absorption', *Journal of the atmospheric sciences* **48**(5), 688–697.

Rex, D. F. (1950), 'Blocking action in the middle troposphere and its effect upon regional climate', *Tellus* **2**(4), 275–301.

Riboldi, J., Lott, F., d'Andrea, F. & Rivière, G. (2020), 'On the linkage between rossby wave phase speed, atmospheric blocking, and arctic amplification', *Geophysical Research Letters* **47**(19), e2020GL087796.

Rodwell, M. & Folland, C. (2002), 'Atlantic air–sea interaction and seasonal predictability', *Quarterly Journal of the Royal Meteorological Society: A journal of the atmospheric sciences, applied meteorology and physical oceanography* **128**(583), 1413–1443.

Rodwell, M. J., Rowell, D. P. & Folland, C. K. (1999), 'Oceanic forcing of the wintertime north atlantic oscillation and european climate', *Nature* **398**(6725), 320–323.

Rossby, C.-G. (1939), 'Relation between variations in the intensity of the zonal circulation of the atmosphere and the displacements of the semi-permanent centers of action', *J. mar. Res.* **2**, 38–55.

Rossler, E. (1976), 'An equation for continuous chaos'.

Saba, V. S., Griffies, S. M., Anderson, W. G., Winton, M., Alexander, M. A., Delworth, T. L., Hare, J. A., Harrison, M. J., Rosati, A., Vecchi, G. A. et al. (2016), 'Enhanced warming of the n orthwest a tlantic o cean under climate change', *Journal of Geophysical Research: Oceans* **121**(1), 118–132.

Scaife, A. A., Woollings, T., Knight, J., Martin, G. & Hinton, T. (2010), 'Atmospheric blocking and mean biases in climate models', *Journal of Climate* **23**(23), 6143–6152.

Schwierz, C., Croci-Maspoli, M. & Davies, H. (2004), 'Perspicacious indicators of atmospheric blocking', *Geophysical research letters* **31**(6).

Sheldon, L., Czaja, A., Vannière, B., Morcrette, C., Sohet, B., Casado, M. & Smith, D. (2017), 'A 'warm path'for gulf stream–troposphere interactions', *Tellus A: Dynamic Meteorology and Oceanography* **69**(1), 1299397.

Shutts, G. (1983), 'The propagation of eddies in diffluent jetstreams: Eddy vorticity forcing of 'blocking'flow fields', *Quarterly Journal of the Royal Meteorological Society* **109**(462), 737–761.

Steinfeld, D. (2020), 'Contrack - contour tracking', `https://github.com/steidani/ConTrack`.

Steinfeld, D., Boettcher, M., Forbes, R. & Pfahl, S. (2020), 'The sensitivity of atmospheric blocking to upstream latent heating–numerical experiments', *Weather and Climate Dynamics* **1**(2), 405–426.

Steinfeld, D. & Pfahl, S. (2019), 'The role of latent heating in atmospheric blocking dynamics: a global climatology', *Climate Dynamics* **53**(9), 6159–6180.

Steinfeld, D., Sprenger, M., Beyerle, U. & Pfahl, S. (2022), 'Response of moist and dry processes in atmospheric blocking to climate change', *Environmental Research Letters* **17**(8), 084020.

Sterl, A. & Caires, S. (2005), 'Climatology, variability and extrema of ocean waves: The web-based knmi/era-40 wave atlas', *International journal of climatology* **25**(7), 963–978.

Stoelinga, M. T. (1996), 'A potential vorticity-based study of the role of diabatic heating and friction in a numerically simulated baroclinic cyclone', *Monthly weather review* **124**(5), 849–874.

Stommel, H. (1948), 'The westward intensification of wind-driven ocean currents', *Eos, Transactions American Geophysical Union* **29**(2), 202–206.

Strogatz, S. H. (2018), *Nonlinear dynamics and chaos: with applications to physics, biology, chemistry, and engineering*, CRC press.

Subramanian, A. C. & Palmer, T. N. (2017), 'Ensemble superparameterization versus stochastic parameterization: A comparison of model uncertainty representation in tropical weather prediction', *Journal of Advances in Modeling Earth Systems* **9**(2), 1231–1250.

Tibaldi, S. & Molteni, F. (1990), 'On the operational predictability of blocking', *Tellus A* **42**(3), 343–365.

Vannière, B., Czaja, A., Dacre, H., Woollings, T. & Parfitt, R. (2016), 'A potential vorticity signature for the cold sector of winter extratropical cyclones', *Quarterly Journal of the Royal Meteorological Society* **142**(694), 432–442.

Visbeck, M., Chassignet, E., Curry, R., Delworth, T., Dickson, R., Krahmann, G., Hurrell, J., Kushnir, Y. & Ottersen, G. (2003), 'The north atlantic oscillation: climatic significance and environmental impact', *Geophys. Monogr* **134**.

Wang, H., Yu, Y. & Wen, G. (2014), 'Dynamical analysis of the lorenz-84 atmospheric circulation model', *Journal of Applied Mathematics* **2014**(1), 296279.

Welander, P. (1968), 'Wind-driven circulation in one-and two-layer oceans of variable depth', *Tellus* **20**(1), 1–16.

Wenta, M., Grams, C. M., Papritz, L. & Federer, M. (2024), 'Linking gulf stream air–sea interactions to the exceptional blocking episode in february 2019: a lagrangian perspective', *Weather and Climate Dynamics* **5**(1), 181–209.

Wilks, D. (2016), '"the stippling shows statistically significant grid points": How research results are routinely overstated and overinterpreted, and what to do about it', *Bulletin of the American Meteorological Society* **97**(12), 2263–2273.

Wilks, D. S. (1997), 'Resampling hypothesis tests for autocorrelated fields', *Journal of Climate* **10**(1), 65–82.

Woollings, T., Barriopedro, D., Methven, J., Son, S.-W., Martius, O., Harvey, B., Sillmann, J., Lupo, A. R. & Seneviratne, S. (2018), 'Blocking and its response to climate change', *Current climate change reports* **4**(3), 287–300.

Yamamoto, A., Nonaka, M., Martineau, P., Yamazaki, A., Kwon, Y.-O., Nakamura, H. & Taguchi, B. (2021), 'Oceanic moisture sources contributing to wintertime euro-atlantic blocking', *Weather and Climate Dynamics* **2**(3), 819–840.

Yamamoto, A., Palter, J. B., Lozier, M. S., Bourqui, M. S. & Leadbetter, S. J. (2015), 'Ocean versus atmosphere control on western european wintertime temperature variability', *Climate dynamics* **45**, 3593–3607.

Yamazaki, A. & Itoh, H. (2013), 'Vortex–vortex interactions for the maintenance of blocking. part i: The selective absorption mechanism and a case study', *Journal of the Atmospheric Sciences* **70**(3), 725–742.

Young, L.-S. (1982), 'Dimension, entropy and lyapunov exponents', *Ergodic theory and dynamical systems* **2**(1), 109–124.

Zubiate, L., McDermott, F., Sweeney, C. & O'Malley, M. (2017), 'Spatial variability in winter nao–wind speed relationships in western europe linked to concomitant states of the east atlantic and scandinavian patterns', *Quarterly Journal of the Royal Meteorological Society* **143**(702), 552–562.

Zuo, H., Balmaseda, M. A., Tietsche, S., Mogensen, K. & Mayer, M. (2019), 'The ecmwf operational ensemble reanalysis–analysis system for ocean and sea ice: a description of the system and assessment', *Ocean science* **15**(3), 779–808.